

ORDINARY
GRANT
IN-46-CR
53052
P-50

SEMI-ANNUAL STATUS REPORT #10
TO THE NATIONAL AERONAUTICS AND SPACE ADMINISTRATION

CRUSTAL DYNAMICS PROJECT

NASA GRANT NAG 5-814
"The Interpretation of Crustal Dynamics Data in Terms of Plate
Motions and Regional Deformation Near Plate Boundaries"

for the period
22 March 1991 - 21 September 1991

Principal Investigator:

Prof. Sean C. Solomon
Department of Earth, Atmospheric,
and Planetary Sciences
Massachusetts Institute
of Technology
Cambridge, MA 02139

(NASA-CR-185844) THE INTERPRETATION OF
CRUSTAL DYNAMICS DATA IN TERMS OF PLATE
MOTIONS AND REGIONAL DEFORMATION NEAR PLATE
BOUNDARIES Semiannual Status Report No. 10,
22 Mar. - 21 Sep. 1991 (MIT) 50 p CSCL 08G G3/46

N92-13508

Unclass
0053052

TABLE OF CONTENTS

	Page
SUMMARY	3
APPENDIX 1: GPS measurements of deformation associated with the 1987 Superstition Hills earthquake, Imperial Valley, California: Evidence for conjugate faulting	4
APPENDIX 2: A comparison of STRC90 and STRC91 campaign results: Strain in the Coachella Valley, southeastern California	6
APPENDIX 3: Lateral variations in upper mantle temperature and composition inferred from shear-wave travel time and attenuation, geoid, and bathymetry	8
APPENDIX 4: Oceanic transform earthquakes with unusual mechanisms or locations: Relation to fault geometry and state of stress in the lithosphere	10
APPENDIX 5: Constraints for the present fault configuration in the Imperial Valley, California: Evidence for northwestward propagation of the Gulf of California rift system	12
APPENDIX 6: Joint inversion of shear wave travel time residuals and geoid and depth anomalies for long-wavelength variations in upper mantle temperature and composition along the Mid-Atlantic Ridge	21

This is a Semi-Annual Status Report on research conducted between 22 March 1991 and 21 September 1991 under NASA Grant NAG 5-814, entitled "The Interpretation of Crustal Dynamics Data in Terms of Plate Motions and Regional Deformation near Plate Boundaries." This grant has supported the research of one Investigator (S. C. Solomon), one Research Staff (R. Reilinger), and two Ph. D. students (A. F. Sheehan and C. J. Wolfe) on behalf of the NASA Geodynamics and Crustal Dynamics Programs.

The focus of the research has been in two broad areas during the most recent 6-month period: (1) the nature and dynamics of time-dependent deformation and stress along major seismic zones, and (2) the nature of long-wavelength oceanic geoid anomalies in terms of lateral variations in upper mantle temperature and composition. The principal findings of our research to date are described in the accompanying appendices. The first is an abstract of a paper given at the SSA Annual Meeting in March 1991, the next three are abstracts of papers to be delivered at the Fall AGU Meeting in December 1991, and the last two are reprints of recently published papers.

APPENDIX 1

GPS measurements of deformation associated with the 1987 Superstition Hills earthquake, Imperial Valley, California: Evidence for conjugate faulting

by S.C. Larsen, R. E. Reilinger, H. Neugebauer, and W. Strange

Presented at the 86th Annual Meeting of the Seismological Society of America, 25-27 March 1991,

San Francisco

Abstract published in *Seismol. Res. Lett.*, 62, 34, 1991.

Large station displacements observed from Imperial Valley GPS campaigns are attributed to the November 24, 1987 Superstition Hills earthquake sequence. Thirty sites from a 42 station GPS network established in 1986 have been reoccupied during 1988 and/or 1990. Displacements at three sites within 3 kilometers of the surface rupture approach 0.5 m. Eight additional stations within 20 km of the seismic zone are displaced at least 10 cm. This is the first occurrence of a large earthquake (M_s 6.6) within a preexisting GPS network. Best-fitting uniform slip models of rectangular dislocations in an elastic half-space indicate 130 cm right-lateral displacement along the northwest trending Superstition Hills fault and 30 cm left-lateral offset along the conjugate northeast trending Elmore Ranch fault. The geodetic moments are 9.4×10^{25} dyne-cm and 2.3×10^{25} dyne-cm for the Superstition Hills and Elmore Ranch faults, respectively. Distributed slip solutions using Singular Value Decomposition suggest near uniform displacement along the Elmore Ranch fault and concentrated slip to the northwest and southeast along the Superstition Hills fault. A significant component of non-seismic secular displacement is observed across the Imperial Valley, which is attributed to interseismic plate-boundary elastic deformation.

APPENDIX 2

A comparison of STRC90 and STRC91 campaign results: Strain in the Coachella Valley, southeastern California

by Lewis E. Gilbert, Shawn Larsen, Robert Reilinger, John Beavan, Ken Hudnut, Bill Young, and Bill Strange

To be presented at the Fall Meeting of the American Geophysical Union, San Francisco, 9-13 December 1991

Abstract published in *AGU 1991 Fall Meeting, Eos Trans. AGU*, suppl., 117, 1991.

The consortium of organizations indicated in the author list and symbolized by our unpronounceable acronym has been monitoring deformation in the Imperial and Coachella Valleys with increasing detail since the establishment of a first epoch in the southern Imperial Valley by NGS in 1986. In 1988 the first epoch measurements were repeated and station coverage was densified. In addition to reoccupation of the 1988 network, 1989 saw the network extend into the Coachella Valley. During 1990, in cooperation with colleagues working south of the Mexican border, 103 stations spanning the region from just south of the intersection of the San Andreas (SAF) and San Jacinto faults to the head of the Gulf of California were occupied. In addition to the primary marks, thirty-one additional marks were occupied for short sessions to provide increased station density along the Banning-Mission Creek section of the SAF. In 1991, our emphasis was on the Coachella section of the network, with few observations in the southern part of the network.

Comparison of the 1986 and 1988 results shows considerable deformation associated with the Superstition Hills earthquake sequence. Displacements at 3 sites within 3 km of the surface rupture approach 0.5 m. Eight additional stations within 20 km of the seismic zone are displaced at least 10 cm. Geodetic moments for the events are 9.4×10^{25} dyne-cm and 2.3×10^{25} dyne-cm for the Superstition Hills and Elmore Ranch faults, respectively. These values are comparable to the calculated seismic moments.

The 1990 data have been processed and will be compared with measurements in the south and with the 1991 data from the Coachella Valley.

APPENDIX 3

**Lateral variations in upper mantle temperature and composition inferred from
shear-wave travel time and attenuation, geoid, and bathymetry**

by Anne F. Sheehan and Sean C. Solomon

To be presented at the Fall Meeting of the American Geophysical Union, San Francisco, 9-13 December 1991

Abstract published in *AGU 1991 Fall Meeting, Eos Trans. AGU*, suppl., 514, 1991.

By means of a large data base of digital seismograms and waveform cross-correlation and spectral ratio techniques, we have measured SS-S differential travel time residuals and differential attenuation in order to determine lateral variations in upper mantle structure beneath the Mid-Atlantic Ridge and East Pacific Rise. After removing the signature of lithosphere age, we find evidence for variations in travel time residuals and attenuation along both ridge systems at wavelengths of 1000 to 7000 km. These travel time anomalies correlate qualitatively with along-axis variations in bathymetry, geoid height, and Love wave phase velocity. We formulate a joint inversion of SS-S travel time residual, geoid height, and bathymetry under that assumption that all arise from variations in upper mantle temperature or bulk composition (parameterized in terms of Mg#). Analysis of differential attenuation places further constraints on the lateral heterogeneity of the temperature field. Inversion for temperature perturbations alone provides good fits to travel time and geoid variations in the north Atlantic region. Compositional variations alone are unable to match the travel time and geoid or bathymetry data simultaneously. Temperature variations are ± 50 K and compositional variations are ± 0.5 -3 % Mg# for models with the temperature variations uniformly distributed over the uppermost 300 km and the compositional variations either distributed uniformly over the same interval or concentrated at shallower depths. The magnitudes of these variations along the Mid-Atlantic Ridge are consistent with the chemistry and geothermometry of dredged peridotites and with variations in the depth extent of mantle melting implied by the chemistry of dredged basalts. Differential travel times of SS-S pairs in the vicinity of the East Pacific Rise show less age dependence than residuals in the north Atlantic and are more consistent with the presence of azimuthal anisotropy. These contrasts may arise from differences in the dynamics of slow and fast spreading ridges.

APPENDIX 4

**Oceanic transform earthquakes with unusual mechanisms or locations: Relation to
fault geometry and state of stress in the lithosphere**

by Cecily J. Wolfe, Eric A. Bergman, and Sean C. Solomon

To be presented at the Fall Meeting of the American Geophysical Union, San Francisco, 9-13 December 1991

Abstract published in *AGU 1991 Fall Meeting, Eos Trans. AGU*, suppl., 518, 1991.

On oceanic transforms, most earthquakes are expected to occur on the principal transform displacement zone (PTDZ) and to have strike-slip mechanisms consistent with offset of a spreading ridge. We conducted a search along the global ridge system for transforms departing from this pattern using the Harvard centroid moment tensor catalogue and earthquake locations from the International Seismological Centre. Events with unusual mechanisms occur on several oceanic transforms. We have analyzed source mechanisms and centroid depths of earthquakes on the St. Paul's, Marathon, Owen, Heezen, Tharp, and Menard transforms from an inversion of long-period body waveforms. Relative locations of earthquakes along these transforms have been determined with a multiple-event relocation technique.

Much of the anomalous earthquake activity can be associated with the presence of complex fault geometry or large structural features that influence the fault. Reverse-faulting earthquakes occur at the St. Paul's transform near St. Paul's Rocks and at a compressional bend at the Owen transform in the area of Error Seamount. An extensional event on the Heezen transform is located at the edge of an extensional offset of the transform, and extensional activity along the Tharp and Menard transforms may also be correlated with extensional offsets. In general, prominent gaps in seismicity can exist near both extensional and compressional bends in a transform.

Some earthquakes with unusual mechanisms occur outside of the transform fault zone and do not appear related to fault zone geometry. Earthquakes with thrust mechanisms are located beneath transverse ridges near the ridge-transform intersection of the St. Paul's transform and the Marathon transform. A normal-faulting earthquake occurred outside the Heezen transform fault zone, in an elongate transform-parallel basin.

Possible influences on the occurrence of such earthquakes include lithospheric thermal stresses, tractions at the base of the plate from asthenospheric flow, changes in plate motion, wrench tectonics, inherited structure, and rotation of principal stresses at a weak fault.

APPENDIX 5

Age constraints for the present fault configuration in the Imperial Valley, California: Evidence for northwestward propagation of the Gulf of California rift system

by Shawn Larsen and Robert Reilinger

Published in *J. Geophys. Res.*, 96, 10,339-10,346, 1991.

Age Constraints for the Present Fault Configuration in the Imperial Valley, California: Evidence for Northwestward Propagation of the Gulf of California Rift System

SHAWN LARSEN

Seismological Laboratory, California Institute of Technology, Pasadena

ROBERT REILINGER

Earth Resources Laboratory, Massachusetts Institute of Technology, Cambridge

Releveling and other geophysical data for the Imperial Valley of southern California suggest the northern section of the Imperial-Brawley fault system, which includes the Mesquite Basin and Brawley Seismic Zone, is much younger than the age of the valley itself. A minimum age of 3000 years is calculated for the northern segment of the Imperial fault from correlations between surface topography and geodetically observed seismic/interseismic vertical movements. Calculation of a maximum age of 100,000 years is based upon displacements in the crystalline basement along the Imperial fault, inferred from seismic refraction surveys. This young age supports recent interpretations of heat flow measurements and the evolution of geothermal systems, which also suggest that the current patterns of seismicity and faulting in the Imperial Valley are not long lived. The current fault geometry and basement morphology suggest a northwestward growth of the Imperial fault and a northwestward migration of the Brawley Seismic Zone. If this localized process is representative of more regional tectonic processes along the extent of the Salton Trough, we suggest that this migration is a manifestation of the propagation of the Gulf of California rift system into the North American continent.

INTRODUCTION

The Salton Trough is a complex transition zone between crustal spreading in the Gulf of California and right-lateral transform motion along the San Andreas fault system (Figure 1). The Imperial Valley is that section of the Salton Trough north of the U.S.-Mexico border and south of the Salton Sea (Figure 2). The Trough is characterized by predominately right-stepping, right-lateral en echelon faults, presumably linked by zones of crustal extension [Lomnitz *et al.*, 1970; Elders *et al.*, 1972]. It forms a 150 by 300 km structural depression which is filled by up to 15 km of late Cenozoic sediments. The seismic velocity of the lower 5-10 km ($V_p = 5.7$ km/s) suggests these sediments are greenschist-facies, metasedimentary rocks [Fuis *et al.*, 1984]. The age of the Imperial Valley-Salton Trough region is suggested to be between 4 and 12 million years [Larson *et al.*, 1968; Moore and Buffington, 1968; Ingle, 1974].

The Imperial Valley and its major fault systems trend northwesterly, nearly parallel to the relative motion between the North American and Pacific plates. Dextral faulting predominates, although northeast-trending sinistral structures, as well as dip-slip motion along north-south surface breaks, play a significant role in the regional tectonics [Johnson and Hutton, 1982; Nicholson *et al.*, 1986; Reilinger and Larsen, 1986].

The Mesquite Basin is a subaerial topographic low bounded on the west by the northern Imperial fault and on the east by the Brawley fault (Figure 2). Maximum basin

relief is about 10 m relative to its periphery. Evidence that the Mesquite Basin is actively subsiding includes geodetic measurements of surface deformation and measurements of vertical slip along the Imperial and Brawley faults. We provide evidence that the Mesquite Basin is extremely young compared to the age of the Imperial Valley, suggesting this section of the Imperial-Brawley fault system is at an early stage of tectonic development. We extend this hypothesis and suggest ongoing northwestward propagation of the Gulf of California rift system.

IMPERIAL VALLEY SEISMICITY AND FAULTING

The Imperial Valley is one of the most seismically active regions of California (Figure 3). A significant fraction of this seismicity occurs within the Brawley Seismic Zone, a region of high activity between the northern Imperial and southern San Andreas faults [Johnson, 1979; Johnson and Hill, 1982]. The Imperial fault ruptured historically in 1940 (M_L 6.4, M_S 7.1) and in 1979 (M_L 6.6, M_S 6.9); episodes of creep have been recognized along the fault since 1966 [Allen *et al.*, 1972]. The seismic moment of the 1979 earthquake is well determined (6×10^{25} dyn cm) [e.g., Kanamori and Regan, 1982], while that for the 1940 event ranges between 10 and 80×10^{25} dyn cm [Trifunac and Brune, 1970; Hanks *et al.*, 1975] although the 48×10^{25} dyn cm moment estimated from long-period surface waves is preferred [Doser and Kanamori, 1987]. Other major earthquakes in the Imperial Valley include the recent 1987 Superstition Hills earthquake sequence: a M_S 6.2 event produced by slip along a northeast-trending seismic lineament, followed 12 hours by a M_S 6.6 earthquake produced by slip along the Superstition Hills fault [Magistrale *et al.*, 1989; Williams and Magistrale, 1989].

The 1979 surficial rupture of the Imperial fault extended from a point 5 km north of the border northwestward

Copyright 1991 by the American Geophysical Union.

Paper number 91JB00618.

0148-0227/91/91JB-00618\$05.00

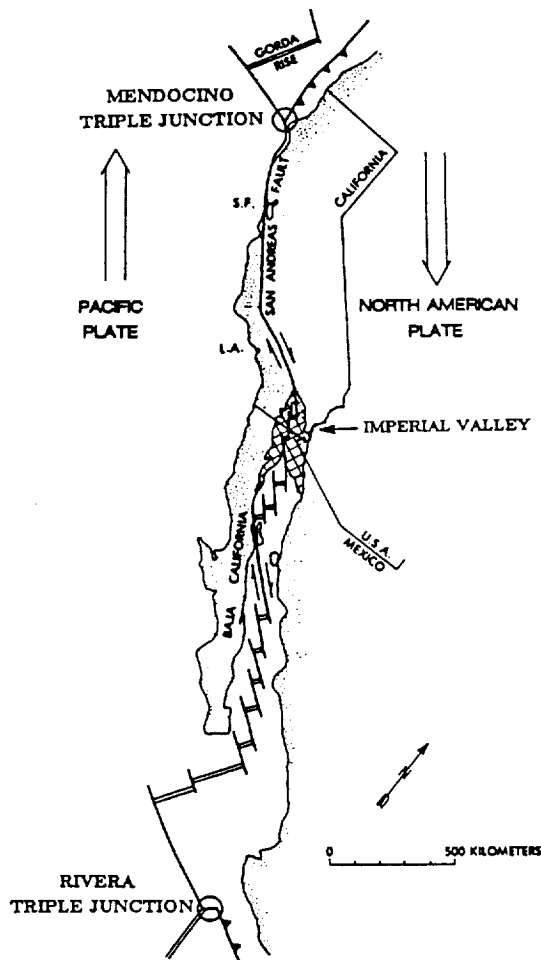


Fig. 1. The Salton Trough (hatch pattern) is a transition zone between crustal spreading in the Gulf of California and right-lateral transform motion along the San Andreas fault. The Imperial Valley is that portion of the Salton Trough north of the U.S.-Mexico border and south of the Salton Sea. Abbreviations are S.F., San Francisco; L.A., Los Angeles. Map modified from *Lachenbruch et al.* [1985].

33.1 km to a point south of Brawley (Figure 4). The predominate strike of the Imperial fault is $N37^{\circ}W$. Along the northwestern most 5 km, however, the fault bends and trends north; we refer to this segment as the north extension. Trending parallel and lying 6 km east of the north extension, the Brawley fault ruptured in 1979 along a 13 km surface break. This rupture pattern generally featured left-stepping en echelon cracks that extended a few millimeters to a few centimeters [Sharp *et al.*, 1982]. A third, relatively minor 1 km north-trending break named the Rico fault was mapped 6–7 km east of the Brawley fault (Figure 4). The surface breakage along this structure resembled that of the Brawley fault zone. The geometrical similarity in strike and separation shown by the north extension, Brawley, and Rico faults, suggest a similar tectonic origin.

The epicenter of the 1940 earthquake was north of the U.S. border, but right-lateral surficial offsets were larger in Mexico (Figure 3). A maximum surface offset of 6 meters was recorded near the border, with displacement tapering off rapidly to the north [Trifunac and Brune, 1970; Sharp, 1982]. Geodetic measurements indicate 4.5 and 3.0 m of right-lateral slip (coseismic plus postseismic) along the southern and northern halves of the Imperial fault, respectively (i.e., north and south of the epicenter), with 2.0 m postseismic slip along a northwest extension of the Brawley fault [Reilinger, 1984]. The 1979 epicenter was south of the border, although surficial displacement was observed only in the United States. Maximum coseismic surficial offset was 55–60 cm, with considerable afterslip (~ 30 cm) during the following 6 months [Sharp *et al.*, 1982]. Strong ground motion and geodetic modeling [Archuleta, 1984; Hartzell and Heaton, 1983; Reilinger and Larsen, 1986] suggest an average slip of about 1 m along the fault plane, with small patches of greater displacement (inferred to be asperities).

The mechanism of strain transfer between the Imperial and San Andreas faults within the Brawley Seismic Zone has been the focus of considerable investigation [e.g., Johnson, 1979]. A conjugate relationship of right-lateral, northwest-

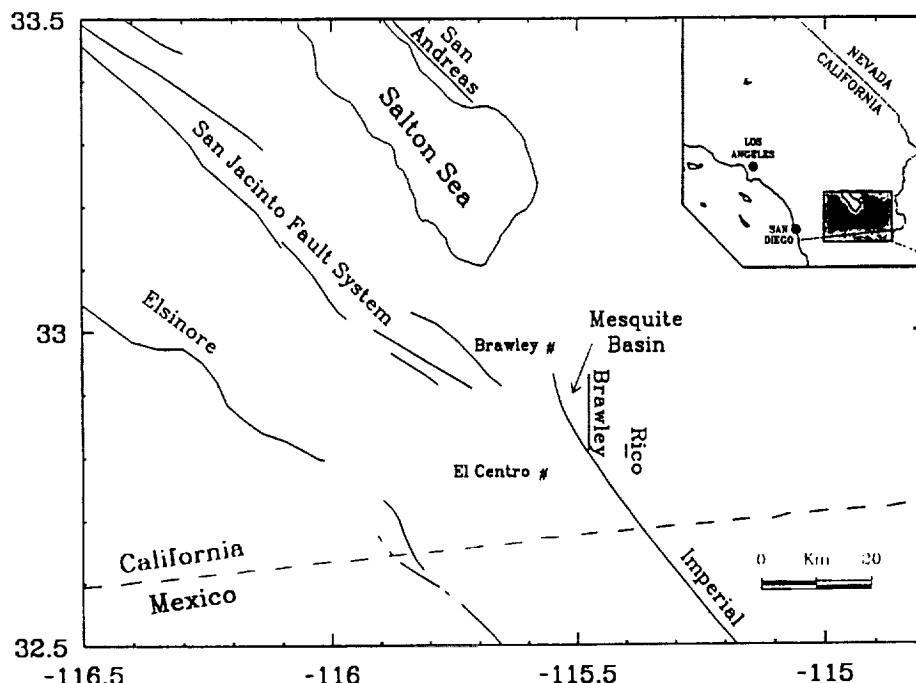


Fig. 2. The Imperial Valley and important faults. The Mesquite Basin is a subaerial topographic depression of about 10 m between the Imperial and Brawley faults.

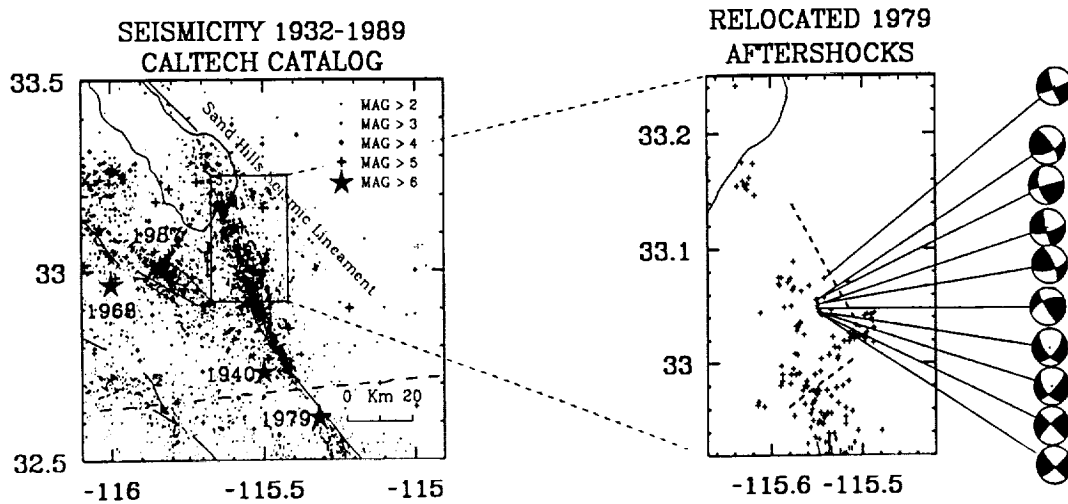


Fig. 3. Seismicity in the Imperial Valley between 1932 and 1989 (Caltech/USGS Catalog). Major events include the 1940 Imperial Valley (M_S 7.1), 1968 Borrego Mountain (M_L 6.5), 1979 Imperial Valley (M_S 6.6), and the 1987 Superstition Hills (M_S 6.6, M_S 6.2) earthquakes. The Brawley Seismic Zone is the active region between the northern reach of the Imperial fault and the southern extent of the San Andreas. The Sand Hills Seismic Lineament is shown by the shaded strip outlining earthquakes trending southeast from the southern end of the San Andreas fault. Shown in the inset are aftershocks of the 1979 earthquake which have been relocated following the methods outlined by *Doser and Kanamori* [1986]. The dashed lines represent orthogonal faults used to satisfy the observed vertical deformation from the 1979 event [*Reilinger and Larsen*, 1986]. Focal mechanisms (lower hemisphere, equal area projections [*Reasenberg and Oppenheimer*, 1985]) for events defining a northwest trend indicate right-lateral strike slip motion.

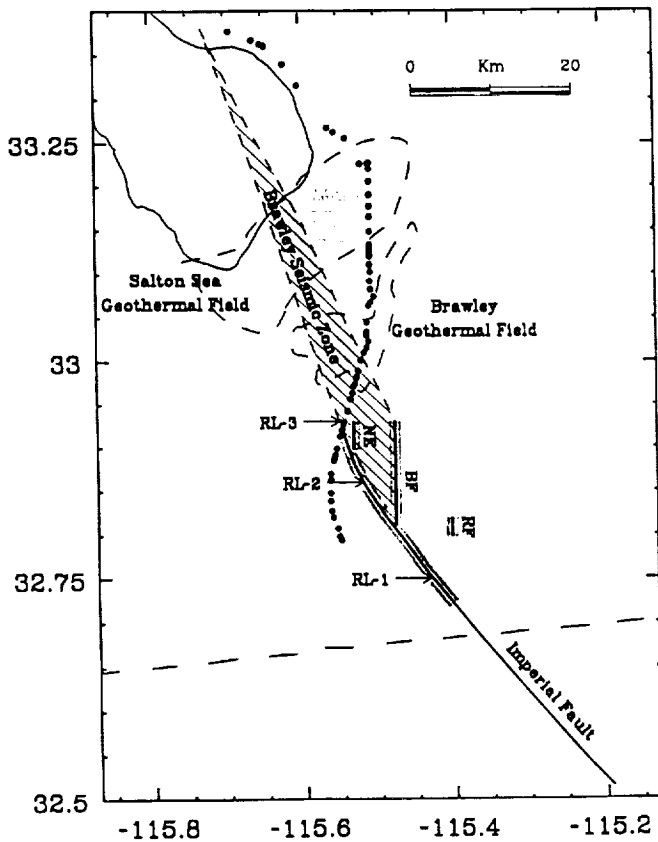


Fig. 4. Map of the Imperial Valley and important tectonic features. Abbreviations are RF, Rico fault; BF, Brawley fault; NE, North Extension. The shaded pattern along each fault indicates the surface rupture from the 1979 earthquake. The Brawley Seismic Zone (hatched) is the region of high seismicity extending northwest from the northern reach of the Imperial fault. The Salton Sea and Brawley geothermal fields are indicated by the shaded patterns. Refraction surveys [*Fuis et al.*, 1984] cross the Imperial fault at RL-1, RL-2, RL-3. The leveling route is shown by the series of dots from the central Imperial Valley to the eastern border of the Salton Sea (each dot representing a benchmark).

trending faults perpendicular to left-lateral, northeast-trending structures may play a significant role in the regional tectonics [*Nicholson et al.*, 1986]. Although the Imperial and San Andreas faults strike predominately northwest (right-lateral), a left-lateral structure extending northeast from the northern terminus of the Imperial fault is indicated from focal mechanisms and the aftershock pattern of the 1979 earthquake [*Johnson and Hutton*, 1982]. A conjugate fault mechanism is supported by *Reilinger and Larsen* [1986], who suggested several tectonic models of the Brawley Seismic Zone satisfying geodetically determined measurements of vertical surface displacement. The preferred model consists of a northeast-trending left-lateral fault conjugate to a right-lateral northwest-trending fault dipping 70° to the southwest (Figure 3, dashed lines). Neither fault broke the surface, but roughly 1 m of slip at depth is required to fit the geodetic measurements. A similar conjugate fault relationship was observed for the 1987 Superstition Hills earthquake sequence [e.g., *Magistrale et al.*, 1989].

Aftershocks from the 1979 earthquake have been relocated following the methods of *Doser and Kanamori* [1986] and *Klein* [1985] (Figure 3). The northeast-trending seismic lineament first identified by *Johnson and Hutton* [1982] is clearly defined. To the north, a tightly constrained group of events following a northwesterly direction is indicated. Epicentral depths for this cluster range from 5 to 11 km, possibly putting them on the 70° west-dipping structure suggested by *Reilinger and Larsen* [1986]. We have computed focal mechanisms for these events and find them consistent with a northwest-trending right-lateral fault (Figure 3). Thus, both seismic and geodetic data suggest the tectonic framework of the Brawley Seismic Zone is marked by an echelon northwest-trending right-lateral faults linked by conjugate left-lateral structures.

Extending southeast from the southern tip of the San Andreas fault is a linear alignment of earthquakes [e.g., *Johnson and Hutton*, 1982], here referred to as the Sand Hills Seismicity Lineament (Figure 3). This feature may signify the southeasterly extension of the San Andreas fault. Although

there is no surfacial geological evidence to support this hypothesis [Sharp, 1982], creep is suggested along northwest segments of the Sand Hills lineament [Jennings, 1975].

The earthquake recurrence interval along the Imperial fault is not well constrained. Sykes and Nishenko [1984] use the 39 year interval separating the 1940 and 1979 shocks as well as a 1915 earthquake sequence located near El Centro [Beal, 1915] to estimate a 32 year recurrence rate. Anderson and Bodin [1987] suggest the fault north of the border will next rupture between 2010 and 2050 (50 year recurrence), and the next break along the southern segment to occur between 2170 and 2290 (300 year recurrence). Measurements of surface offset, as well as seismic and geodetically determined estimates of fault slip at depth, indicate the 1940 fault rupture was several times larger than in 1979, in agreement with the larger moment for the 1940 event. North of the border, however, the magnitude of horizontal surface displacement was relatively constant for the two earthquakes. One explanation for this is that the fault north of the border may rupture more frequently but with smaller events. Alternatively, the large postseismic slip following the 1940 earthquake indicated by geodetic data, suggests that a significant fraction of strain buildup may be relieved aseismically.

If the entire 49 mm/yr movement between the Pacific and North American plates predicted by new global plate models (NUVEL-1) [DeMets *et al.*, 1987, 1990] is accommodated across the Imperial fault, 1.0 m of seismic or aseismic fault slip would require a 20 year interval of strain buildup. More likely, however, a significant component of plate motion is distributed along the Elsinore and San Jacinto fault systems [Sharp, 1981; Pinault and Rockwell, 1984; Snay *et al.*, 1986], as well as faults off the coast of southern California [e.g., Weldon and Humphreys, 1986]. Trilateration and triangulation measurements from 1941 to 1987 in the central Imperial Valley indicate an average displacement across the Imperial fault of 35–43 mm/yr [Prescott *et al.*, 1987; Snay and Drew, 1988]. Preliminary results utilizing the Global Positioning System (GPS) suggest a slightly larger rate between 1986 and 1989, although interpretation of these measurements have been complicated by large displacements from the 1987 Superstition Hills earthquake sequence [Larsen, 1991].

Assuming 40 mm/yr of plate motion across the Imperial fault, 1.0 m of potential slip will accumulate in 25 years. This is equivalent to the earthquake recurrence interval, at least for the northern segment of the Imperial fault, if the ~ 1.0 m surface displacement measured in 1940 and 1979 is characteristic of fault displacement and if all slip is generated seismically. Considering the likelihood of aseismic deformation, as well as seismic and geodetic models indicating 2–3 m slip asperities along the 1979 rupture plane, it is reasonable to expect that the average slip generated along the northern Imperial fault during each earthquake cycle is somewhat greater than 1.0 m. Assuming 2–3 m of slip (based on the seismic plus postseismic offset estimated for the 1940 earthquake and the maximum slip observed for the 1979 earthquake), more reasonable estimates of earthquake recurrence would be 50 to 75 years for this segment of the Imperial fault.

SUBSIDENCE OF THE MESQUITE BASIN

First-order leveling surveys crossing the northern Mesquite Basin were conducted by the National Geodetic Survey (NGS) in 1931, 1941, 1974, 1978, and 1980 (Figure 4). Profiles of elevation change from 1931 to 1941, 1941

to 1974, and 1978 to 1980 are shown in Figure 5. The procedure used to determine these crustal movement profiles is described in Brown and Oliver [1976]. Briefly, an estimate of relative elevation change between successive benchmarks is obtained by subtracting the elevation difference between benchmarks measured at some reference time from the difference measured at some later time. These movement profiles have not been connected to any external reference. Therefore, only relative movements along the level lines are significant.

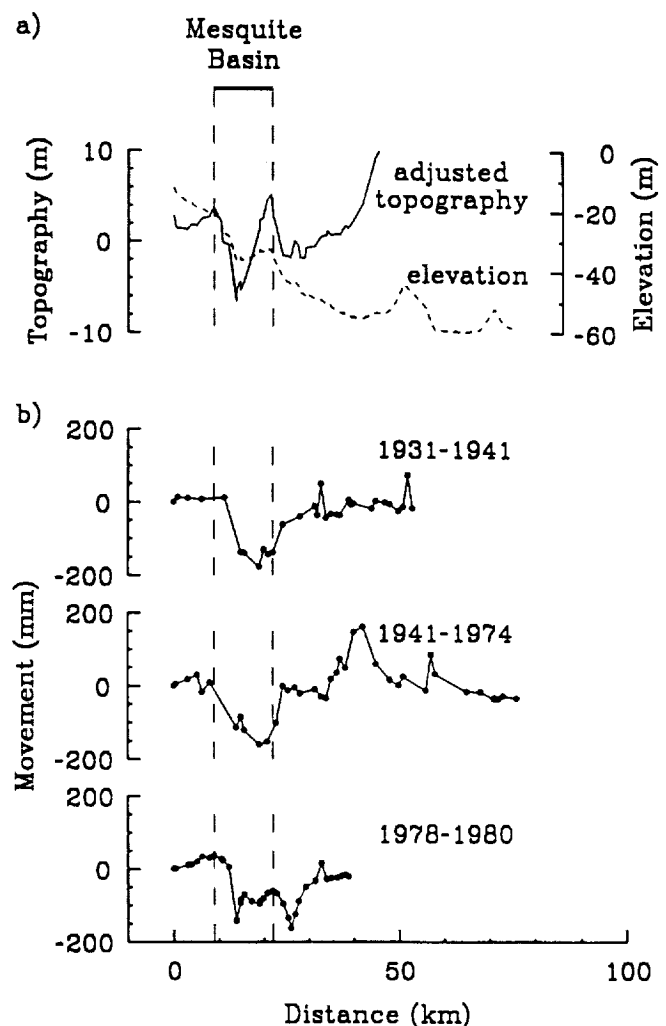


Fig. 5. (a) Elevation (dashed line) along the leveling route between El Centro and the Salton Sea. The adjusted topography (solid line) is the elevation with the northward tilt of -0.0011 radians removed. The 10 m depression between 9 and 22 km is the surfacial expression of the Mesquite Basin. (b) Elevation changes along the leveling route from 1931 to 1941, 1941 to 1974, and 1978 to 1980. Note the strong correlation between deformation and the surface expression of the Mesquite Basin.

The random error for these measurements is comparatively small, less than 1 cm. In addition, elevation-correlated errors (i.e., rod calibration and atmospheric refraction) which can obscure or be mistaken for real tectonic deformation, will not seriously affect the data because of negligible topographic variation along the leveling route (Figure 5a).

The 1931–1941 and 1941–1974 profiles have been modeled as coseismic and postseismic deformation from the 1940 Imperial Valley earthquake [Reilinger, 1984]. Displacements for the most recent interval (1978 to 1980) have been

modeled as surface deformation from the 1979 earthquake [Reilinger and Larsen, 1986]. The most striking feature of the leveling data is the similar pattern of subsidence across the Mesquite Basin observed on all three profiles, suggesting this deformation style is characteristic for the region. Coseismic subsidence for the 1940 and 1979 events are on the order of 10–15 cm, with an additional 15 cm following the 1940 earthquake. Total subsidence for the period 1931 to 1980 is about 40 cm.

Elevation along the leveling route is shown in Figure 5a (dashed line). A relatively constant northward slope of -0.0011 radians is observed. This long-wavelength trend may mask small scale variations, so we construct a modified topographic profile by removing this regional slope (we add 0.0011 radians to the true profile). The modified profile, or adjusted topography, is shown as the solid line in Figure 5a. The 10-meter depression between 9 and 22 km marks the boundary and surface relief along the northern part of the Mesquite Basin. The topographic relief is well correlated with the seismically generated subsidence, strongly suggesting the Mesquite Basin formed by many episodes of seismic activity similar to the 1940 and 1979 events.

Vertical surface slip along the northern section of the 1979 rupture plane ranged from 0 to 30 cm (including 6 months afterslip), while vertical offset along the Brawley fault was 0 to 24 cm [Sharp *et al.*, 1982]. Measurements of vertical slip following the 1940 earthquake were sparse, although the sense of displacement was generally the same as in 1979 [Sharp, 1982]. During an earthquake swarm in 1975, up to 20 cm of vertical displacement was observed along the Brawley fault and an additional 20 cm possibly occurred between 1960 and 1975 [Sharp, 1976]. In each case, slip was down to the east along the Imperial fault and down to the west along the Brawley fault. Displacement on the Rico fault during the 1979 event was down to the west.

Perhaps the most puzzling and intriguing aspect of deformation in the Mesquite Basin is shown by the offset pattern recorded in the crystalline basement along the Imperial fault. Seismic refraction experiments were conducted by the U.S. Geological Survey in the Imperial Valley during 1979 [Fuis *et al.*, 1984]. Three refraction lines RL-1, RL-2, and RL-3 cross the Imperial fault where shown in Figure 4. (These correspond to Fuis *et al.* [1984] lines 6NW-1SE-1NW, 1ESE, 1E-2W.) The seismic measurements indicate a 1000 m basement offset across the Imperial fault at RL-1, a 500 m offset at RL-2, whereas no basement offset is observed at RL-3. That is, the offset increases to the southeast. Where detectable, the subsurface morphology is down to the east. The basement is defined as rock with $V_p = 5.6$ km/sec, which approximately corresponds to 5 km depth. What makes the basement structure so unusual is its opposite arrangement to the deformation displayed at the surface, where vertical fault offsets measured for the 1940 and 1979 earthquakes generally increased to the northwest. In fact, where the basement structure is maximum (at RL-1), the coseismic vertical surface displacements were either small or non-existent. Presumably, this apparent discrepancy between surface and sub-surface structure must illustrate an important tectonic feature.

AGE OF FAULTING

The correlation between geodetically measured subsidence and the topographic expression shown in Figure 5 strongly suggests this region developed from episodes of seis-

mic activity similar to the 1940 and 1979 earthquakes. In fact, this example clearly illustrates that earthquakes are a fundamental building block of tectonic structures. The 10 m surface depression, together with the subsidence rate and basement morphology, places constraints on the age of the Mesquite Basin, and correspondingly the northern segment of the Imperial fault.

About 5 m of seismic and postseismic slip along the Imperial fault north of the border is required to form the 40 cm subsidence between the earliest and most recent levelings across the Mesquite Basin (1931–1980) [Reilinger, 1984; Reilinger and Larsen, 1986]. At a slip rate of 40 mm/yr across the Imperial fault, 5 m of potential slip will accumulate in 125 years. The equivalent basin subsidence rate is thus about 3 mm/yr. While depending heavily on the rate of strain accumulation, this analysis is invariant to the earthquake recurrence interval.

At a tectonic subsidence rate of 3 mm/yr, the 10 m depression which outlines the Mesquite Basin would form in 3000 years. This suggests that the tectonic framework underlying the basin, namely the northern Imperial and Brawley faults, is extremely young compared to the 4 to 12 million year age of the Imperial Valley. However, this estimate does not include sediment influx into the Mesquite Basin. While the measured seismic subsidence is about an order of magnitude larger than typical fill rates in arid regions [Ollier, 1981], the basin is located in one of the largest river deltas in the United States; presumably sediment influx is high. In fact, the average rate of deposit in the central Imperial Valley is about 1 mm/yr (5 km over the last 5 million years), only slightly smaller than the rate of tectonic subsidence. Overlying sediments may mask a deeper basin, so 3000 years is an extreme minimum duration for basin development.

The lack of an observed basement offset at RL-3 places further constraint on fault age. The geometry and dextral motion of the San Andreas and Imperial faults require extension in the Brawley Seismic Zone. Dip-slip motion along the northern Imperial and Brawley faults helps to fill this requirement. Although geodetic, geologic, and strong-motion data indicate significant vertical displacements along the northern segment of the Imperial fault (north of its intersection with the Brawley fault), apparently insufficient time has elapsed to allow the formation of a detectable basement offset at its northern extent. The lack of offset suggests this region formed relatively recently and is at its earliest stage of tectonic development. Fuis *et al.* [1984] suggest that on intersecting refraction lines in the Imperial Valley, structural boundaries to about 5 km depth agree to within a few tenths of a kilometer. Assuming the refraction data can resolve offsets of 300 m (about 1/2 of the offset measured at RL-2), at a tectonic subsidence rate of 3 mm/yr the maximum age for the northern Imperial fault is about 100,000 years; again very young compared to the 4–12 million year age of the Imperial Valley.

Other evidence support a young age for this segment of the Imperial fault. Models of heat transfer mechanisms suggest the Salton Sea geothermal field (Figure 4) formed within the last 3000 to 20,000 years [Kasameyer *et al.*, 1980, 1984], consistent with the 3000 to 100,000 year age range calculated for the Mesquite Basin. If representative of central Imperial Valley tectonics, this geothermal field likely formed contemporaneously with the Brawley Seismic Zone and the northern Imperial fault. To achieve a balance between thermal constraints and the current composition of the crust,

Lachenbruch *et al.* [1985] calculate that heat flow measurements within the Imperial Valley indicate an average extension rate of $\sim 10^{-14} \text{ s}^{-1}$ since the formation of the Salton Trough. At this rate, the differential velocity between the Pacific and North American plates requires that extension and faulting must have been distributed over a relatively wide region ($\sim 150 \text{ km}$) during the last several million years. Presumably, tectonic and seismic activity, which is presently highly concentrated along the Imperial fault and within the Brawley Seismic Zone, is part of an evolutionary process in which tectonic activity is shifted from one region of the valley to another. The northern Imperial and Brawley faults, Mesquite Basin, and Brawley Seismic Zone may represent the most recent epoch of activity in a rapidly changing fault geometry.

PROPAGATING RIFT?

As discussed above, the relationship between seismicity, dip-slip faulting, and basement offset indicates a young age for the northern segment of the Imperial fault. Similarly, the large basement offset along the central section of the fault (at RL-1) suggests significant vertical slip along this segment in the past. We suggest here a scenario for the recent history of the Imperial fault and the Brawley Seismic Zone, that includes the northwestward propagation of the Gulf of California oceanic rift system.

Although rupture along the Imperial fault is predominately strike slip, the large component of normal motion along the northern segment of the fault is presumably in response to the en echelon geometry of the San Andreas and Imperial faults. These faults may act as transforms associated with a spreading center beneath the Brawley Seismic Zone [Elders *et al.*, 1972; Johnson, 1979]. If the northern extent of the Imperial fault, as well as the Brawley Seismic Zone were previously further south (perhaps southeast of El Centro), dip-slip motion would be expected along this segment of the fault. Eventually, a detectable offset would develop in the crystalline basement. As the spreading center (Brawley Seismic Zone) migrated northwest to its present position, so would the vertical movements during seismic events. Although rupture along the fault becomes increasingly strike slip with age, the vertical offset equals the integrated offset through time, and therefore increases with age. This model accounts for the apparent disparity between long-term vertical offsets on the Imperial fault (increasing basement offset to the southeast) and present-day seismic fault slip (maximum dip-slip along the northern segment of the fault).

The rupture pattern for the 1979 earthquake supports this hypothesis (Figure 4). Clearly the northern Imperial and Brawley faults are active components in the stress/strain transfer mechanism between the Imperial and San Andreas faults. Both structures show significant seismic displacements at the surface and at depth. Although displacement along the Rico fault was 10–20 cm vertical with no horizontal offset [Sharp *et al.*, 1982; Reilinger and Larsen, 1986], the 1 km rupture length suggests it is only a minor constituent in the regional tectonics. The Rico, Brawley, and the north extension of the Imperial fault, each follow a north-south trend and are uniformly spaced at distances of 6 to 7 km. This geometrical similarity suggests a similar tectonic origin. In fact, the Rico fault may be an older structure reactivated during the 1979 earthquake, although little is known about its past history [Sharp *et al.*, 1982].

A schematic illustration of the temporal evolution of this region is shown in Figure 6. If the Brawley Seismic Zone was further southeast than at present, the Rico fault may have acted as the Brawley fault does today. Similarly, the Brawley fault would have been the northern splay of the Imperial fault, identical to the present north extension. A prehistoric basin would have developed between the Rico and Brawley faults (forming the observed fault offset), similar to the Mesquite Basin. Presumably, as the Imperial fault lengthened to the northwest, the Rico-Brawley fault system no longer influenced the stress/strain distribution between the northern Imperial and southern San Andreas faults. As a result, a new fault developed (north extension) and the

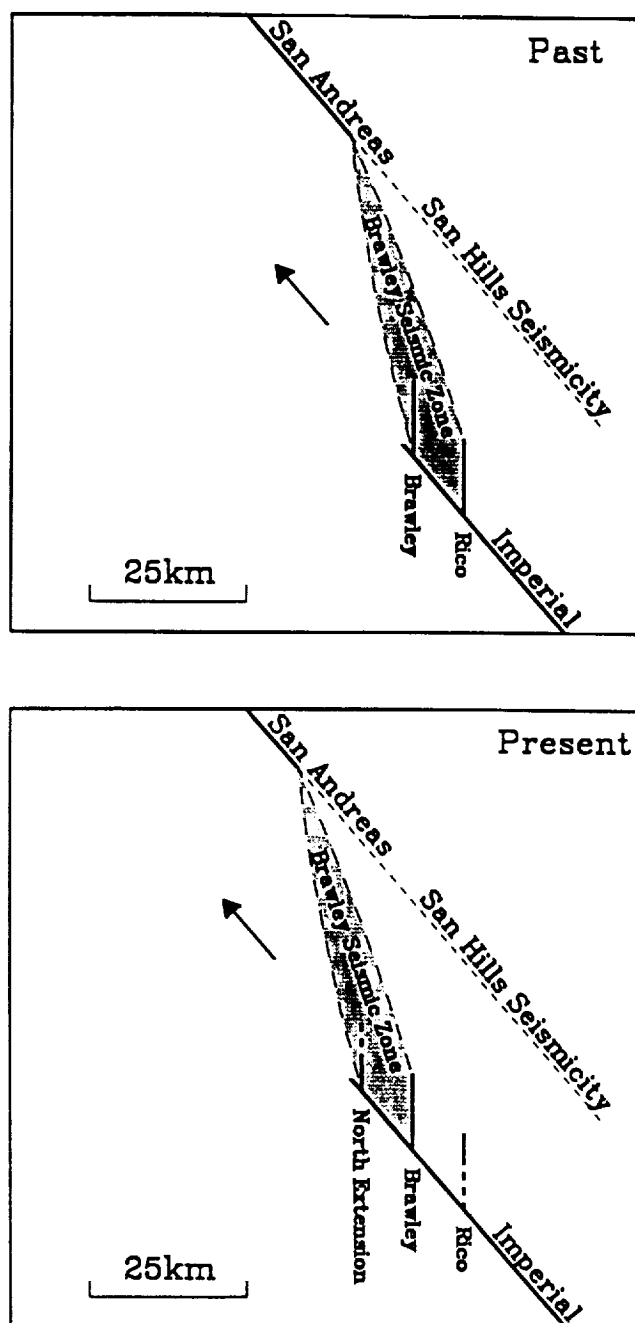


Fig. 6. Schematic diagram of past and present fault configurations in the Imperial Valley illustrating the hypothesized northwesterly migration of the Brawley Seismic Zone. In this model the San Hills Seismicity Lineament is the extension of the San Andreas, left dormant after the passage of the Brawley Seismic Zone.

Rico fault died out. Continued migration of the Brawley Seismic Zone may in the future create a new north-south trending structure northwest of the present terminus of the Imperial fault. As the Brawley Seismic Zone shifted to the northwest, so did the southern terminus of the San Andreas fault (Figure 6). The Sand Hills lineament appears to be the remnant of an older segment of the San Andreas, and except for residual seismic activity, left dormant with the northwest passage of the Brawley Seismic Zone.

An apparent inconsistency with this model is that the slip direction on the north extension is down to the east, while slip along the Brawley and Rico faults is down to the west. A distinction is made here between the northern Imperial fault and the north extension. It is the normal movement on the Imperial fault which generates the offset observed in the crystalline basement; the north-trending faults are subsidiary features. Once the Brawley Seismic Zone migrates past its present position, the north extension could maintain its current slip orientation without affecting the tectonic model suggested in Figure 6. It is also conceivable that the slip orientation on this fault could be reversed in the near future (down to the west), or that another fault could develop in its place.

It is possible to make a rough estimate for the migration rate of the Imperial fault and southern Brawley Seismic Zone. Assuming a dip-slip offset rate of 3 mm/yr (estimated above), approximately 330,000 years are required to create the 1000 m basement offset measured along the Imperial fault at RL-1. The 3000 to 100,000 year age for the fault segment 20 km to the northwest (at RL-3) indicates that the Brawley Seismic Zone has migrated about 20 km during the last 250,000 to 300,000 years. This yields a migration rate of about 7 cm/yr. While this rate is only a very crude estimate, it is significant to note that it is comparable to typical plate motion velocities (i.e., several centimeters per year). In fact, the estimated spreading rate in the mouth of the Gulf of California averaged over the last 3 million years is 4.9 cm/yr [e.g., DeMets et al., 1987].

If the Brawley Seismic Zone represents the crustal manifestation of a subcrustal spreading center, we speculate that its northwesterly migration is directly associated with the propagation of the Gulf of California rift system into the North American continent. This hypothesis assumes that the localized transient phenomenon observed along the northern Imperial fault is characteristic of more regional tectonic processes throughout the Salton Trough. Clearly, the Imperial Valley and Brawley Seismic Zone are undergoing rapidly changing tectonics. Understanding the kinematics of these changes will help constrain the dynamic processes which control the transition between crustal spreading in the Gulf of California and transform motion along the San Andreas fault.

CONCLUSIONS

Geodetic, seismic, tectonic, and heat flow data in the Imperial Valley suggest that the northern segment of the Imperial-Brawley fault system is extremely young compared to the 4 to 12 million year age of the Imperial Valley. We find a minimum age of 3000 years based upon the relationship between topography and earthquake induced geodetic displacements, and estimate a maximum age of 100,000 years based upon observed basement offsets across the Imperial fault determined from seismic refraction surveys. A young age is consistent with heat flow data, which indicate a dis-

tributed and ephemeral pattern of faulting in the Imperial Valley [Lachenbruch et al., 1985].

In addition, we speculate that the apparent incompatibility along the Imperial fault between the observed seismic vertical displacements (maximum to the north) and the offset recorded in the crystalline basement (maximum to the south) is a direct result of the northwestward propagation of the Imperial fault and Brawley Seismic Zone. A series of evenly spaced north-trending surface ruptures and the Sand Hills seismicity lineament are consistent with this hypothesis. A 7 cm/yr migration rate is calculated from measured surface displacements and from variations in basement morphology along the Imperial fault. The migration of the Brawley Seismic Zone and Imperial fault may be associated with the propagation of the Gulf of California rift system into the North American continent.

Acknowledgments. We thank the National Geodetic Survey and in particular Emery Balazs for providing the leveling data reported here. Reviews by Kerry Sieh, Hiroo Kanamori, William Prescott, Eugene Humphreys, and Carl Johnson were very helpful and substantially improved the present manuscript, as were comments by Gary Fuis on a much earlier version. We thank Liz Henderson for formatting the text for *JGR*. This work was supported in part by NASA grant NAG 5-814 and by U.S. Geological Survey contracts 14-08-0001-61679 (MIT) and 14-08-0001-61354 (Caltech). Caltech Division of Geological and Planetary Sciences contribution 4871.

REFERENCES

- Allen, C. R., M. Wyss, J. N. Brune, A. Grantz, and R. E. Wallace, Displacements on the Imperial, Superstition Hills, and San Andreas faults triggered by the Borrego Mountain earthquake, *U.S. Geol. Surv. Prof. Pap.*, 787, 84-104, 1972.
- Anderson, J. G., and P. Bodin, Earthquake recurrence models and historical seismicity in the Mexicali-Imperial Valley, *Bull. Seismol. Soc. Am.*, 77, 562-578, 1987.
- Archuleta, R. J., A faulting model for the 1979 Imperial Valley Earthquake, *J. Geophys. Res.*, 89, 4559-4585, 1984.
- Beal, C. H., The earthquake in the Imperial Valley, California, July 22, 1915, *Bull. Seismol. Soc. Am.*, 5, 130-149, 1915.
- Brown, L. D., and J. E. Oliver, Vertical crustal movements from leveling data and their relations to geologic structure in the eastern United States, *Rev. Geophys.*, 14, 13-35, 1976.
- DeMets, C., R. G. Gordon, S. Stein, and D. F. Argus, A revised estimate of Pacific-North America motion and implications for western North America plate boundary zone tectonics, *Geophys. Res. Lett.*, 14, 911-914, 1987.
- DeMets, C., R. G. Gordon, D. F. Argus, and S. A. Stein, Current plate motions, *Geophys. J. Int.*, 101, 425-478, 1990.
- Doser, D. I., and H. Kanamori, Depth of seismicity in the Imperial Valley region (1977-1983) and its relationship to heat flow, crustal structure, and the October 15, 1979, earthquake, *J. Geophys. Res.*, 91, 675-688, 1986.
- Doser, D. I., and H. Kanamori, Long-period surface waves of four western United States earthquakes recorded by the Pasadena strainmeter, *Bull. Seismol. Soc. Am.*, 77, 236-243, 1987.
- Elders, W. A., R. W. Rex, T. Meidav, P. T. Robinson, and S. Bieher, Crustal spreading in southern California, *Science*, 178, 15-24, 1972.
- Fuis, G. S., W. D. Mooney, J. H. Healy, G. A. McMechan, and W. J. Lutter, A seismic refraction survey of the Imperial Valley region, California, *J. Geophys. Res.*, 89, 1165-1189, 1984.
- Hanks, T. C., J. A. Hileman, and W. Thatcher, Seismic moments of the larger earthquakes of the southern California region, *Geol. Soc. Am. Bull.*, 86, 1131-1139, 1975.
- Hartzell, S. H., and T. H. Heaton, Inversion of strong ground motion and teleseismic waveform data for the fault rupture history of the 1979 Imperial Valley, California, earthquake, *Bull. Seismol. Soc. Am.*, 73, 1553-1583, 1983.
- Ingle, J. C., Paleobathymetric history of Neogene marine sediments, northern Gulf of California, *Geology of Peninsular California*, pp. 121-138, Pacific Sections AAPG, SEPM, and SEG, 1974.

- Jennings, C. W. (compiler), Fault map of California, Calif. Div. of Mines and Geol., scale 1:750,000, 1975.
- Johnson, C. E., CEDAR—An approach to the computer automation of short-period local seismic networks: Seismotectonics of the Imperial Valley of southern California, Ph.D. thesis, 343 pp., Calif. Inst. of Technol., Pasadena, 1979.
- Johnson, C. E., and D. P. Hill, Seismicity of the Imperial Valley, The Imperial Valley, California, earthquake of October 15, 1979, *U.S. Geol. Surv. Prof. Pap.*, 1254, 14–22, 1982.
- Johnson, C. E., and L. K. Hutton, Aftershocks and preearthquake seismicity, *U.S. Geol. Surv. Prof. Pap.*, 1254, 59–76, 1982.
- Kanamori, H., and J. Regan, Long-period surface waves, *U.S. Geol. Surv. Prof. Pap.*, 1254, 55–58, 1982.
- Kasameyer, P. W., L. W. Younker, and J. M. Hanson, Age of the Salton Sea geothermal system as inferred from the thermal data, *Geol. Soc. Am. Abstr. Programs*, 12, 458, 1980.
- Kasameyer, P. W., L. W. Younker, and J. M. Hanson, Development and application of a hydrothermal model for the Salton Sea Geothermal Field, California, *Geol. Soc. Am. Bull.*, 95, 1242–1252, 1984.
- Klein, F. W., User's guide to HYPOINVERSE, a program for VAX and PC350 computers to solve for earthquake locations, *U.S. Geol. Surv. Open File Rep.*, 85-515, 24 pp., 1985.
- Lachenbruch, A. H., J. H. Sass, and S. P. Galanis, Jr., Heat flow in southernmost California and the origin of the Salton Trough, *J. Geophys. Res.*, 90, 6709–6736, 1985.
- Larsen, S. C., Geodetic measurement of deformation in southern California, Ph.D. thesis, 351 pp., Calif. Inst. of Technol., Pasadena, 1991.
- Larson, P. A., H. W. Menard, and S. M. Smith, Gulf of California: A result of ocean-floor spreading and transform faulting, *Science*, 161, 781–784, 1968.
- Lomnitz, C., F. Mooser, C. R. Allen, J. N. Brune, and W. Thatcher, Seismicity and tectonics of northern Gulf of California region, Mexico: Preliminary results, *Geofis. Int.*, 10, 34–48, 1970.
- Magistrale, H., L. Jones, and H. Kanamori, The Superstition Hills, California, earthquakes of 24 November, 1987, *Bull. Seismol. Soc. Am.*, 79, 239–251, 1989.
- Moore, D. G., and E. C. Buffington, Transform faulting and growth of the Gulf of California since late Pliocene, *Science*, 161, 1238–1241, 1968.
- Nicholson, C., L. Seeber, P. Williams, and L. R. Sykes, Seismic evidence for conjugate slip and block rotation within the San Andreas fault system, southern California, *Tectonics*, 89, 629–648, 1986.
- Ollier, C., *Tectonics and Landforms*, 324 pp., Longman Group Limited, New York, NY, 1981.
- Pinault, C. T., and T. K. Rockwell, Rates and sense of Holocene faulting on the Elsinore fault: Further constraints on the distribution of dextral shear between the Pacific and North American plates, *Geol. Soc. Am. Abstr. Programs*, 16, 624, 1984.
- Prescott, W. H., M. Lisowski, and J. C. Savage, Velocity field along the San Andreas fault in southern California, *Eos Trans., AGU*, 68, p. 1506, 1987.
- Reasenber, P., and D. Oppenheimer, FPFIT, FPLOT, FPAGE: Computer programs for calculating and displaying earthquake fault-plane solutions, *U.S. Geol. Surv. Open File Rep.*, 85-739, 46 pp., 1985.
- Reilinger, R. E., Coseismic and postseismic vertical movements associated with the 1940 Imperial Valley, California, earthquake, *J. Geophys. Res.*, 89, 4531–4537, 1984.
- Reilinger, R. E., and S. C. Larsen, Vertical crustal deformation associated with the 1979 $M_L = 6.6$ Imperial Valley, California, earthquake: Implications for fault behavior, *J. Geophys. Res.*, 91, 14,044–14,056, 1986.
- Sharp, R. V., Surface faulting in Imperial Valley during the Earthquake swarm of January–February 1975, *Bull. Seismol. Soc. Am.*, 66, 1145–1154, 1976.
- Sharp, R. V., Variable rates of late Quaternary strike slip on the San Jacinto fault zone, southern California, *J. Geophys. Res.*, 86, 1754–1762, 1981.
- Sharp, R. V., Comparison of 1979 surface faulting with earlier displacements in the Imperial Valley, *U.S. Geol. Surv. Prof. Pap.*, 1254, 213–221, 1982.
- Sharp, R. V., J. J. Lienkaemper, M. G. Bonilla, D. B. Burke, B. F. Fox, D. G. Herd, D. M. Miller, D. M. Morton, D. J. Ponti, M. J. Rymer, J. C. Tinsley, J. C. Yount, J. E. Kahle, E. W. Hart, and K. E. Sieh, Surface faulting in the central Imperial Valley, *U.S. Geol. Surv. Prof. Pap.*, 1254, 119–143, 1982.
- Snay, R. A., and A. R. Drew, Supplementing geodetic data with prior information for crustal deformation in the Imperial Valley, California, Technical Report Series, Geodetic Institute, University of Stuttgart, 1988.
- Snay, R. A., M. W. Cline, and E. L. Timmermand, Horizontal crustal deformation models for California from historical geodetic data, *R. Soc. N. Z. Bull.*, 24, 131–140, 1986.
- Sykes, L. R., and S. P. Nishenko, Probabilities of occurrence of large plate rupturing earthquakes for the San Andreas, San Jacinto, and Imperial faults, California, 1983–2003, *J. Geophys. Res.*, 89, 5905–5927, 1984.
- Trifunac, M. D., and J. N. Brune, Complexity of energy release during the Imperial Valley, California, earthquake of 1940, *Bull. Seismol. Soc. Am.*, 60, 137–160, 1970.
- Weldon, R., and E. Humphreys, A kinematic model of southern California, *Tectonics*, 5, 33–48, 1986.
- Williams, P. L., and H. W. Magistrale, Slip along the Superstition Hills fault associated with the 24 November 1987 Superstition Hills, California, earthquake, *Bull. Seismol. Soc. Am.*, 79, 390–410, 1989.

S. Larsen, Seismological Laboratory, California Institute of Technology, Pasadena, CA 91125.

R. Reilinger, Earth Resources Laboratory, Massachusetts Institute of Technology, Cambridge, MA 02139.

(Received May 3, 1990;
revised February 26, 1991;
accepted November 5, 1990.)

APPENDIX 6

Joint inversion of shear wave travel time residuals and geoid and depth anomalies for long-wavelength variations in upper mantle temperature and composition along the Mid-Atlantic Ridge

by Anne F. Sheehan and Sean C. Solomon

Published in *J. Geophys. Res.*, 96, 19,981-20,009, 1991.

Joint Inversion of Shear Wave Travel Time Residuals and Geoid and Depth Anomalies for Long-Wavelength Variations in Upper Mantle Temperature and Composition Along the Mid-Atlantic Ridge

ANNE F. SHEEHAN AND SEAN C. SOLOMON

Department of Earth, Atmospheric, and Planetary Sciences, Massachusetts Institute of Technology, Cambridge

We report measurements of *SS-S* differential travel time residuals for nearly 500 paths crossing the northern Mid-Atlantic Ridge. Differential travel times of such phases as *SS* and *S* with identical source and receiver have the advantage that residuals are likely to be dominated by contributions from the upper mantle near the surface bounce point of the reflected phase (*SS*). Under this assumption, differential *SS-S* travel time residuals are mapped at the *SS* bounce points as a means of delineating lateral variations in mantle structure. After removing the signature of lithosphere age, we find evidence for variations in *SS-S* residuals along the ridge at wavelengths of 1000–7000 km. These travel time anomalies correlate qualitatively with along-axis variations in bathymetry and geoid height. We formulate a joint inversion of travel time residual, geoid height, and bathymetry under the assumption that all arise from variations in upper mantle temperature or bulk composition (parameterized in terms of *Mg #*). The inversion employs geoid and topography kernels which depend on the mantle viscosity structure. Inversion for thermal perturbations alone provides good fits to travel time and geoid data. The fit to topography, which is likely dominated by unmodeled crustal thickness variations, is not as good. The inversions for temperature favor the presence of a thin low-viscosity layer in the upper mantle and temperature perturbations concentrated at depths less than 300 km. Compositional variations alone are unable to match the travel time and geoid or bathymetry data simultaneously. A joint inversion for temperature and composition provides good fits to both geoid and travel time anomalies. Temperature variations are ± 50 K and compositional variations are ± 0.5 –3% *Mg #* for models with the temperature variations uniformly distributed over the uppermost 300 km and the compositional variations either distributed uniformly over the same interval or concentrated at shallower depths. The magnitudes of these variations are consistent with the chemistry and geothermometry of dredged peridotites along the Mid-Atlantic Ridge.

INTRODUCTION

Seismic velocity and density of upper mantle material are expected to be functions of temperature and composition. The delineation of long-wavelength variations in these physical properties thus provides important constraints on mantle convection, crust-mantle differentiation, and mantle chemical heterogeneity. In this study we determine lateral variations in upper mantle temperature and composition along the Mid-Atlantic Ridge through the combined inversion of shear wave differential travel times, geoid height, and bathymetric depth anomalies.

The advent of seismic tomography has led to a number of three-dimensional maps of lateral variations in seismic velocity in the upper mantle, and several such models of the North Atlantic region have been developed, both as parts of global studies [e.g., Woodhouse and Dziewonski, 1984; Nakanishi and Anderson, 1984; Tanimoto, 1990] and through regional investigations of long-period surface waves [e.g., Honda and Tanimoto, 1987; Mocquet *et al.*, 1989; Mocquet and Romanowicz, 1990]. With surface wave methods, each wave samples the average vertical variation in upper mantle structure along its path, but because of the long wavelengths involved, the inversion of phase or group velocity from many paths tends to smooth out lateral variations. Body wave travel times can provide independent information about upper mantle heterogeneity at potentially shorter horizontal scales than surface waves can resolve,

and progress has been made in the determination of lateral heterogeneity in the North Atlantic through the use of both differential and absolute travel times of body waves [Kuo *et al.*, 1987; Grand, 1987, 1989].

The travel times used in this study are differential times of the body wave phase pair *SS-S*. Differential travel times of shear wave pairs are well suited to the study of upper mantle heterogeneity [Sipkin and Jordan, 1976, 1980; Stark and Forsyth, 1983; Butler, 1979; Kuo *et al.*, 1987; Woodward and Masters, 1991a] and have the advantage that source and receiver effects are approximately common to both phases and are thus largely eliminated by differencing. Under the assumption that the lower mantle is relatively homogeneous and that the portions of the wave paths in the upper mantle are steep, the differential travel time anomaly can be associated with upper mantle structure within a small volume centered beneath the surface bounce point of the reflected (*SS*) phase. This technique is thus well suited to the investigation of horizontal variations in structure, but the resolution of variations with depth is poor.

Oceanic bathymetry and geoid height data are sensitive to variations in mantle density at depth. Such variations can be either thermal or compositional in origin and, like seismic velocity, are presumably related to mantle convection and differentiation. Geoid (or gravity) and topography have become the most commonly used tools for mapping and constraining models of upper mantle convection [e.g., Anderson *et al.*, 1973; McKenzie and Bowin, 1976; McKenzie, 1977; McKenzie *et al.*, 1980; Parsons and Daly, 1983; Buck and Parmentier, 1986; Craig and McKenzie, 1986]. In addition, measurement of the admittance (the spectral ratio

Copyright 1991 by the American Geophysical Union.

Paper number 91JB01988.
0148-0227/91/91JB-01988\$05.00

of geoid to topography) has been widely utilized to estimate the depth and mode of compensation of oceanic swells and plateaus [e.g., Watts *et al.*, 1985; Cazenave *et al.*, 1988; Sandwell and MacKenzie, 1989; Sheehan and McNutt, 1989]. Several workers [Dziewonski *et al.*, 1977; Nakanishi and Anderson, 1984; Tanimoto and Anderson, 1984; Stark and Forsyth, 1983; Dziewonski, 1984; Kuo *et al.*, 1987] have noted correlations of geoid and travel time (or velocity structure) at a number of different wavelengths, although only a few [Hager *et al.*, 1985; Hager and Clayton, 1989; Hager and Richards, 1989] have combined observational seismology with geoid anomalies in a quantitative and dynamically consistent manner.

Since very different convective flows can produce the same geoid and surface topography, the inversion of these data alone for the thermal or compositional source function is nonunique. Because this inverse problem is not well posed, most studies have concentrated on forward modeling, i.e., varying the parameters of a simple model until a good fit to the data is achieved. With this approach, there is no guarantee that the set of parameters which give the best fit to the data is unique and that the correct solution has been isolated. Including seismic data provides additional constraints which are sufficient to allow us to formulate simple one-dimensional inversions. These inversions, of course, are still nonunique, but they are better constrained than those using only geoid or bathymetry data.

In this paper we present the first formal inversion of geoid, depth, and SS-S differential travel time anomaly data for lateral variations in upper mantle temperature and composition along the Mid-Atlantic Ridge. Given a distribution of temperature or density perturbations in the upper mantle, the forward problem of calculating differential travel time, geoid, and depth anomalies is straightforward. This forward problem forms the basis for a joint linear inversion of these three types of observations under the assumption that all arise from parameterized long-wavelength variations in upper mantle temperature or composition. Results of a set of inversions carried out under different assumptions regarding the depth extent of lateral heterogeneity and the mantle viscosity structure are compared with other constraints on variations in mantle temperature and degree of melt removal.

MEASUREMENT OF DIFFERENTIAL TRAVEL TIMES

The seismic data used in this study consist of long-period *S* and *SS* phases obtained from the Global Digital Seismic Network (GDSN) [Peterson *et al.*, 1976; Peterson and Hutt, 1982]; the Network of Autonomously Recording Seismographs (NARS), a linear broadband array in western Europe [Nolet and Vlaar, 1982]; and several broadband stations from the global GEOSCOPE network [Romanowicz *et al.*, 1984, 1991]. We use only transversely polarized (*SH*) seismograms (rotated from N-S and E-W components) to avoid interference from the *SKS* phase and contamination from *P-SV* conversions at the base of the crust and other near-surface discontinuities. Recent work by Gee and Jordan [1989] suggests that travel times depend on the frequency band used in the analysis. In order to maintain a self-consistent data set for our study, additional processing is applied to data from the NARS and GEOSCOPE networks in order to mimic the instrument response of the longer-period GDSN stations. This processing allows us to measure

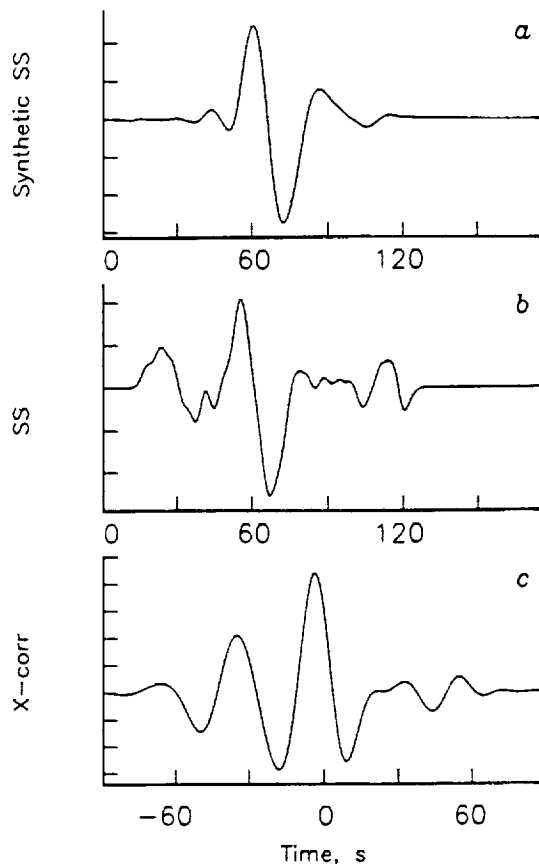


Fig. 1. An example of the measurement of SS-S differential travel time for the event of December 24, 1985 (10 km focal depth), at GDH (63° epicentral distance). (a) "Synthetic" SS pulse generated from *S*. The *S* pulse is windowed and attenuated to account for the additional time that SS travels in the mantle ($t^* = 3$ s), and a $\pi/2$ phase shift is applied. (b) Windowed SS wave pulse. (c) Cross correlation of the trace in Figure 1b with that in Figure 1a. The differential travel time residual is -5.0 s.

travel times from a set of seismograms that all have essentially the same frequency response. Data from the NARS and GEOSCOPE stations are decimated (with a low-pass antialiasing filter) to a common sampling interval of 1 s. The data are further filtered using a noncausal three-point Butterworth filter [Rader and Gold, 1967] with a frequency band pass of 0.01–0.20 Hz. This additional filtering greatly improves the signal-to-noise ratio of the SS phase.

A waveform cross-correlation method is utilized to determine the differential travel time between the phases *S* and *SS* [Butler, 1979; Stark and Forsyth, 1983; Kuo *et al.*, 1987]. The procedure involves the construction of a "synthetic" SS pulse from *S* and the evaluation of the cross-correlation function between the real and synthetic windowed SS phases (Figure 1). The synthetic SS pulse is created from *S* in the following manner. The *S* pulse is windowed and attenuated (with attenuation parameter $t^* = 3$ s) [Grand and Helmberger, 1984; Kuo *et al.*, 1987] to account for the additional time SS travels in the mantle, and then a $\pi/2$ phase shift (Hilbert transform) is applied to the attenuated *S* pulse to simulate the frequency-dependent phase shift which the SS wave undergoes at an internal caustic [Choy and Richards, 1975]. The differential time is obtained from the peak of the cross correlation between the synthetic SS

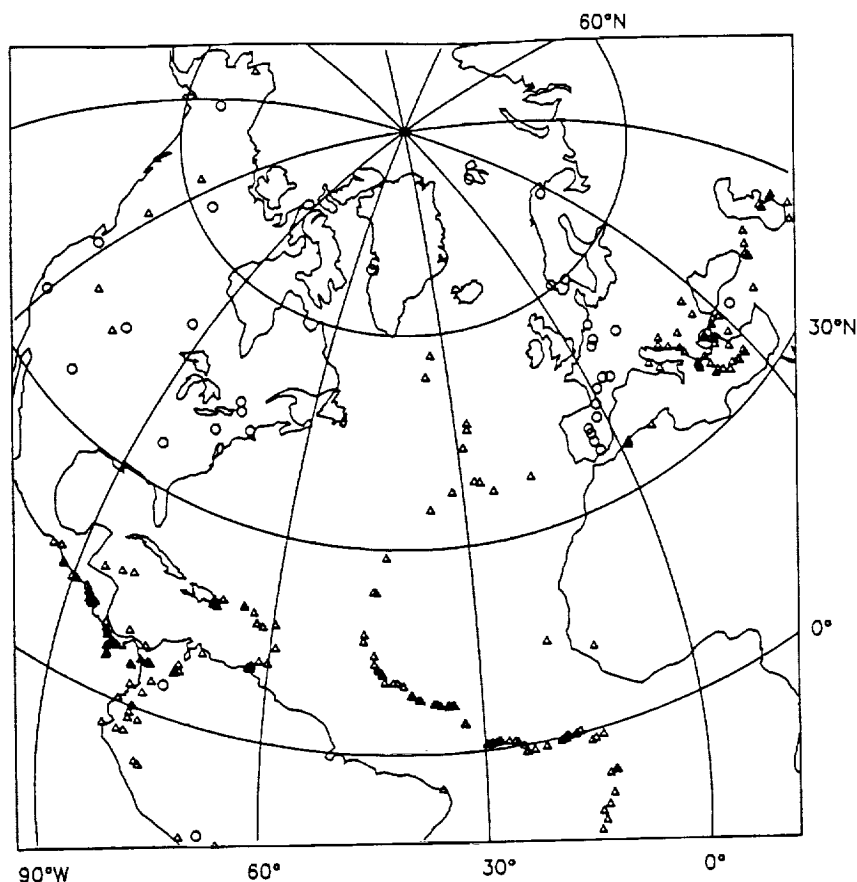


Fig. 2. Distribution of earthquakes (triangles) and seismograph stations (circles) used to measure $SS-S$ differential travel times. Stations are from the GDSN, NARS, and GEOSCOPE digital arrays. Earthquakes are from the Harvard CMT catalogue (generally $m_b > 5.0$) from the years 1977–1987. Lambert equal-area projection with pole of projection at 45°N , 40°W .

constructed from the S wave and the real SS . The residual $SS-S$ times are obtained by subtracting the observed differential time from that predicted by the preliminary reference earth model (PREM) [Dziewonski and Anderson, 1981] and correcting for Earth ellipticity [Dziewonski and Gilbert, 1976] and SS bounce point bathymetry. Our convention is that negative residuals are indicative of either early SS or late S .

Constant window lengths of 120 s are used for both the S and SS phases. In general, the observed differential travel times vary by as much as 1 s depending on how S and SS are windowed. Our modeling with synthetic seismograms indicates that emphasizing the onset of the SS waveform can lead to bias for bounce points in areas of oceanic sediments. The effect of sediments at long periods is to produce precursory arrivals from reflections at the base of the sediments and late arrivals from waves which travel through the low-velocity sediments and are reflected at the crust-water interface. The net effect, after convolving the crustal response with the long-period GDSN instrument response, is that the time center of the SS phase is effectively unchanged but the pulse is broadened both at the front and at the back. In our procedure the use of a constant window containing the entire SS pulse should yield differential travel times that are little affected by the presence of sediments.

DATA

The North Atlantic is an ideal area for conducting a differential travel time study in terms of the geographic

distribution of available events and stations at suitable distances. The range in source-receiver separation was taken to be 55° – 86° to ensure separation of S and ScS at the longer distances and to avoid triplication in SS at shorter distances. The SS and S phases bottom from about 670 to 2300 km depth. We performed a search over all earthquakes in the Harvard centroid moment tensor (CMT) catalog for the years 1977–1987 [Dziewonski et al., 1981; Dziewonski and Woodhouse, 1983] and over all GDSN, NARS, and GEOSCOPE digital seismic stations in order to find event-station pairs of the proper epicentral distance which provide SS bounce points in the North Atlantic region. Epicenters were obtained from the bulletin of the International Seismological Centre (ISC) for events occurring before 1987 and from the Preliminary Determination of Epicenters of the U.S. National Earthquake Information Service (NEIS) for events occurring in 1987. The final distribution of sources and stations used to measure $SS-S$ differential travel times is shown in Figure 2. The majority of data in this study comes from records of equatorial fracture zone earthquakes at North American and European stations, north and central Atlantic events at North American stations, Central American events at European stations, and Mediterranean and European earthquakes at North American stations.

This search yielded over 2000 event-station pairs with the proper epicentral separation. After winnowing the list because of station inoperation, poor signal-to-noise ratio for the phases of interest, and interfering events, the final data

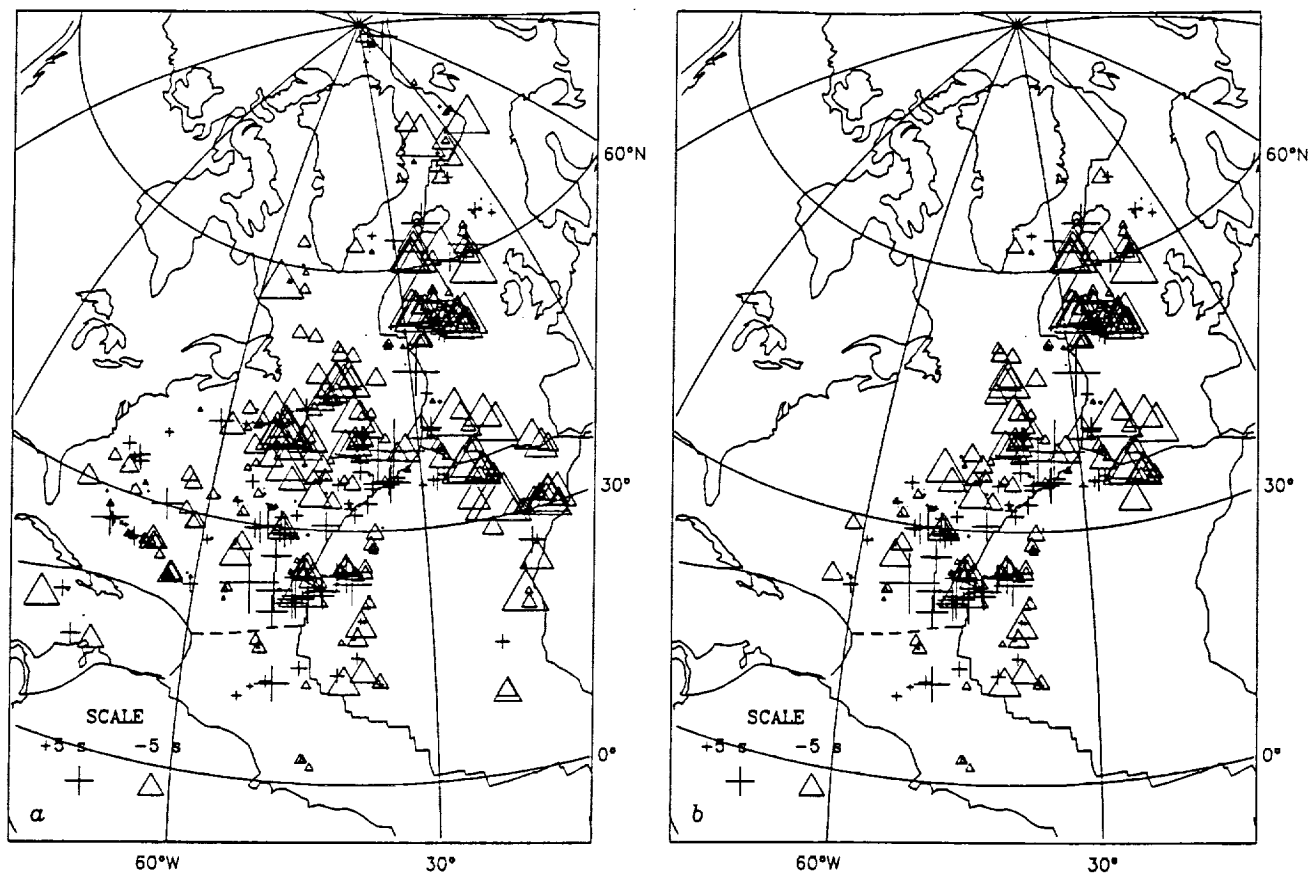


Fig. 3. (a) Map view of SS-S residuals relative to PREM [Dziewonski and Anderson, 1981], corrected for Earth ellipticity and seafloor bathymetry. Residuals are plotted at the SS bounce point. The size of each symbol scales linearly with the magnitude of the residual. Lambert equal-area projection with pole of projection at 40°N, 40°W. Negative residuals indicate either early SS or late S. Plate boundaries are from DeMets *et al.* [1990]. (b) Same as Figure 3a but including data only for SS bounce points on lithosphere younger than 100 Ma.

set consists of nearly 500 SS-S differential travel time residuals with bounce points in the North Atlantic (Figure 3). Uncertainties are determined for each measurement following the procedure outlined in Appendix A. A tabulation of all residuals, by station and source, is given by Sheehan [1991].

RESULTS

We interpret the variations in SS-S differential travel times in terms of lateral velocity variations within the crust and upper mantle beneath the surface reflection points of the SS wave path. Kuo *et al.* [1987] and Woodward and Masters [1991a] tested the validity of this assumption by plotting absolute S and SS residuals against SS-S residuals. They found that S and SS-S residuals are uncorrelated, while SS and SS-S residuals are strongly correlated, indicating that the assumption is justified. The validity of this assumption is further supported by the strong correlation of SS-S times with surface tectonic features in the vicinity of the SS bounce point. The residuals are further interpreted in terms of such upper mantle processes as lithospheric aging, flow-induced anisotropy, and along-axis heterogeneity in mantle structure.

Lithospheric Aging

Cooling and thickening of the lithosphere should yield a tendency toward an increase in seismic velocity with in-

creasing lithospheric age. A linear regression experiment was performed to examine the correlation of the SS-S residuals with seafloor age. A gridded map of seafloor ages was constructed for the North Atlantic from the magnetic anomalies of Klitgord and Schouten [1986] and ages assigned according to Kent and Gradstein [1986] and Klitgord and Schouten [1986]. The isochrons of Sclater *et al.* [1981] were used in a few regions which were not covered by the Klitgord and Schouten [1986] data set. To obtain a representative age value for the region spanning approximately one horizontal wavelength of the incident (SS) wave, an average seafloor age was estimated for a $1^\circ \times 1^\circ$ box centered on each SS bounce point. To reduce scatter, measurements whose bounce point depths differed by more than 2500 m from the depth predicted by the Parsons and Sclater [1977] plate cooling model were excluded from the final age regression. Although each SS wave samples the upper mantle at a finite range of lithosphere ages, we expect that the different travel time anomalies contributed by the SS path segments on the younger and older sides of the bounce point approximately cancel so that the age at the SS bounce point is appropriate to the associated SS-S residual.

The SS-S residuals for the North Atlantic are consistent with the expectation of an increase in seismic velocity with seafloor age. For bounce points between 0° and 60°N latitude, the coefficient derived by linear regression of residual

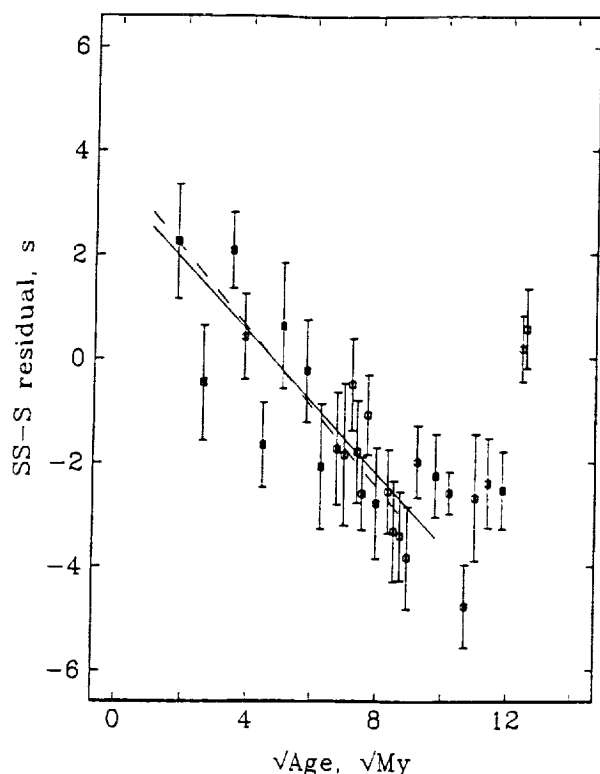


Fig. 4. SS-S travel time residual versus square root of seafloor age for data from 0 to 60°N. Each plotted point represents the weighted mean of 14 adjacent data points. Weights are constructed from variances determined as discussed in Appendix A. Horizontal and vertical bars are standard errors of the means of the travel time residuals and $(\text{age})^{1/2}$. Linear regression yields a slope of $-0.68 \pm 0.08 \text{ s Ma}^{-1/2}$ for a 0–100 Ma age range (solid line) or $-0.76 \pm 0.09 \text{ s Ma}^{-1/2}$ for a 0–80 Ma range (dashed line).

with square root of age is $-0.68 \pm 0.08 \text{ s Ma}^{-1/2}$ from 0 to 100 Ma, with a linear correlation coefficient of -0.85 (Figure 4). Residuals north of 60°N, however, do not seem to be strongly correlated with lithospheric age. This may be due to the fact that this area is more tectonically complicated than "normal" oceanic lithosphere [e.g., White, 1988; Zehnder and Mutter, 1990], includes several ridge jumps, is in close proximity to continental regions and does not closely follow the age-depth relation of Parsons and Sclater [1977]. Compared with the residuals for 0–60°N, those from north of 60°N are anomalously negative at young ages and anomalously positive at older ages. Although the age dependence of data from these high latitudes is anomalous, these data are no less reliable and will be retained in our analysis of heterogeneity. The slope of SS-S residual versus square root of age for data from 0 to 60°N is smaller than that inferred from S delays of intraplate earthquakes in the Atlantic by Duschene and Solomon [1977] (two-way S delay = $-1.2 \text{ s Ma}^{-1/2}$) and that reported by Kuo et al. [1987] ($-1 \text{ s Ma}^{-1/2}$). It is larger, however, than the global average obtained by Woodward and Masters [1991a] ($-0.51 \text{ s Ma}^{-1/2}$). Because the residual-age relation is not constant over the entire North Atlantic, some of these variations in slope may reflect real geographic differences.

We may compare the variation of SS-S residual versus age with that due only to lithospheric cooling. For a lithospheric structure given by the plate cooling model of Par-

sons and Sclater [1977], we may convert temperature variations to differences in shear velocity v_s by adopting a value for $\partial v_s / \partial T$, which we take to be uniform and equal to -0.6 m/s K^{-1} [McNutt and Judge, 1990]. For a horizontal slowness typical of the teleseismic S and SS waves of this study (0.1375 s km^{-1}), the slope of the line best fitting the SS-S travel time delay versus age given by the plate cooling model over 0–100 Ma is then $-0.64 \pm 0.07 \text{ s Ma}^{-1/2}$, a result indistinguishable from the observed slope. This agreement indicates that the dependence of travel time residual on plate age can be explained entirely by lithospheric cooling.

The trend of the travel time residual versus lithospheric age relation changes at about 100 Ma. After 100 Ma, the residuals appear to flatten out (Figure 4), in the same sense as the plate cooling model of Parsons and Sclater [1977]. Such a pattern may reflect the unmodeled effect of increased sediment or crustal thickness or, as suggested by Parsons and Sclater [1977] may be partially the result of secondary convection which supplies heat to the base of the plate at older ages. To avoid possible biases associated with any of these effects, we shall restrict our analysis to data with bounce points on seafloor younger than 100 Ma. To look for other systematic variations in the residuals, we correct for age by removing the linear relation shown by the solid line in Figure 4. This correction is effectively a normalization of residuals to 22-Ma-old lithosphere (the zero crossing of the regression line). Since the age correction is linear, normalization of the residuals to a different age would simply result in a constant value being added to or subtracted from all residuals.

Anisotropy

Another systematic velocity variation that has been suggested as a possible contributor to residual SS-S travel times is azimuthal anisotropy. Kuo et al. [1987] examined this phenomenon in detail and concluded that alignment of olivine crystals in the asthenosphere created a significant pattern of azimuthal anisotropy in SS-S residuals measured in the Atlantic region. We have also searched for evidence of azimuthal anisotropy with our data set.

Backus [1965] and Crampin [1977] demonstrated, from the general form of body wave anisotropy in a weakly anisotropic medium, that the linear form of the azimuthal variation of velocity is given by

$$V^2 = A_0 + A_1 \cos 2\theta + A_2 \sin 2\theta + A_3 \cos 4\theta + A_4 \sin 4\theta \quad (1)$$

where V is the body wave velocity, the A_n are linear functions of the elastic moduli, and θ is an azimuth, defined for our problem by the angle between the great circle path and the direction to geographic north measured at the SS bounce point. Equation (1) was further simplified by Kuo et al. [1987] and parameterized in terms of travel time residuals:

$$R = R_0 + R_1 \cos 2\theta + R_2 \sin 2\theta + R_3 \cos 4\theta + R_4 \sin 4\theta \quad (2)$$

where R is the travel time residual and the R_n are constants. By fitting a function of this form to our age-corrected

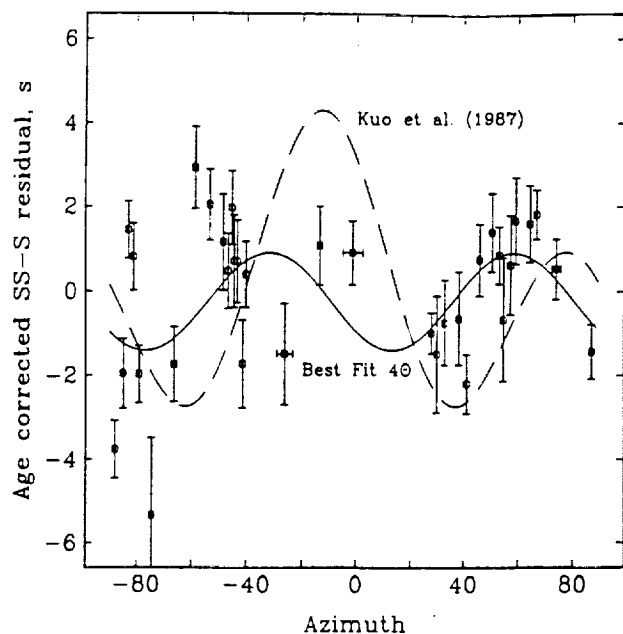


Fig. 5. Age-corrected SS-S residual (see text) versus azimuth θ . Each plotted point represents the weighted mean of 10 adjacent data points. The solid curve shows the best fitting 4θ variation derived from these data. The dashed curve shows the preferred model of Kuo *et al.* [1987], which corresponds to an alignment of the a axis of olivine in the approximate direction $N13^\circ W$.

measurements we can determine if our data are consistent with the presence of anisotropy.

We have conducted several tests of azimuthal anisotropy with our travel time data. We performed least squares inversions to determine 2θ and 4θ patterns which provide best fits to the age-corrected SS-S residuals. Data from the region north of $60^\circ N$ were included in the regressions discussed here, but a second set of regressions performed without these data yielded similar results. The anisotropy indicated by our regression experiments differs significantly from the preferred model of Kuo *et al.* [1987] both in magnitude and in phase (Figure 5). Our results indicate that for the 2θ model the slow direction for SS-S is $N4^\circ W$ and the peak-to-peak magnitude of the effect is less than 1 s; for the 4θ model the slow directions are $N32^\circ W$ and $N58^\circ E$ and the magnitude is 2.5 s; for the joint 2θ and 4θ model the slow direction is $N32^\circ W$ and the magnitude is just under 3 s. Kuo *et al.* [1987] obtained a peak-to-peak variation with azimuth of 5–7 s and a slow direction at $N13^\circ W$. The slowest residuals in the Kuo *et al.* [1987] study were from north-south paths, i.e., nearly along the ridge, and the fastest residuals were from northeast-southwest trending paths with bounce points north of the Azores-Gibraltar plate boundary (an area noted to be anomalously fast in their study), so their reported anisotropy may have been at least partly the result of unmodelled upper mantle heterogeneity. Our inversion for a 2θ pattern of anisotropy provided a variance reduction of only 2%, compared with 20% for a 4θ pattern and 22% for a combined 2θ and 4θ pattern. On the basis of these values of variance reduction and the number of free parameters involved, our results suggest that there is no single coherent pattern of upper mantle anisotropy in the North Atlantic. Inversions were performed on geographic subsets of the data to test whether there may be several distinct patterns of

anisotropy acting in the North Atlantic region, but the results were inconclusive because of a poor sampling of azimuths in the smaller subregions. The latest anisotropic upper mantle models obtained from surface wave tomography [Montagner and Tanimoto, 1990] show a complex pattern of anisotropy in the North Atlantic region. Any azimuthal anisotropy in the asthenosphere induced by plate motions in the North Atlantic may be heterogeneous because the three plates in the region are slow moving and the return flow is not closely related to plate divergence [Hager and O'Connell, 1979, 1981; Parmentier and Oliver, 1979].

Spatial Patterns of Age-Corrected Residuals

After removal of the dependence on seafloor age, a plot of SS-S travel time residuals at the SS surface reflection point (Figure 6) shows several interesting features. Perhaps the most striking is that residuals in the western Atlantic north of about $35^\circ N$ are on average nearly 4 s more negative than those to the south. This feature is also noticeable in Figure 3 but is more obvious after age dependence is removed. A similar change at approximately this latitude was noted for SS-S residuals with SS bounce positions on the eastern side of the Mid-Atlantic Ridge by Kuo *et al.* [1987] and was attributed to a change in upper mantle structure across the Azores-Gibraltar plate boundary. The signal that we observe is predominantly from data with bounce points on the western side of the ridge. A map view of the azimuthal distribution is shown in Figure 7 and serves as an aid to assess qualitatively the geometry of wave paths to the south and north of $35^\circ N$. We examined the possibility that this signal may be from the Caribbean anomaly, a region of anomalously high velocity in the mantle between 600 and 1400 km depth beneath the Caribbean originally reported by Jordan and Lynn [1974] and further confirmed by Grand [1987]. If the first leg of the SS wave paths from South America to western Europe were to bottom in the high-velocity Caribbean region, the result would be early SS-S residuals. This would produce a feature of opposite sign from that observed, so we discount it as an influence here. Another possible explanation for the long-wavelength signal could be azimuthal anisotropy, but the examination above of possible patterns of azimuthal anisotropy does not support this suggestion.

Another distinctive feature of the residuals in Figure 6 is a row of negative values which trends northwest to southeast along the trace of the New England Seamounts and across the ridge to the vicinity of the Great Meteor Seamount. This feature in the residual map comes from event-station pairs at a number of different azimuths and distances, so cannot be attributed to a source or receiver effect. We do not observe distinctive anomalies in the vicinity of the Bermuda, Azores, or Canary Islands hotspots. The data density is poor for the Bermuda region, however, and any signal associated with the Canary Islands may be obscured by the ocean-continent transition. Recently active hotspot islands might be expected to display strong positive (late) residuals, such as Stewart and Keen [1978] observed for PP-P residuals at the Fogo Seamounts. In contrast, Woodward and Masters [1991a] found mostly negative (early) SS-S residuals in the vicinity of the Hawaiian hotspot, and Jordan [1979] and Sipkin and Jordan [1980] have suggested that the net effect of hotspots may be to produce early arrivals because of the presence of high velocities in a depleted mantle residuum.

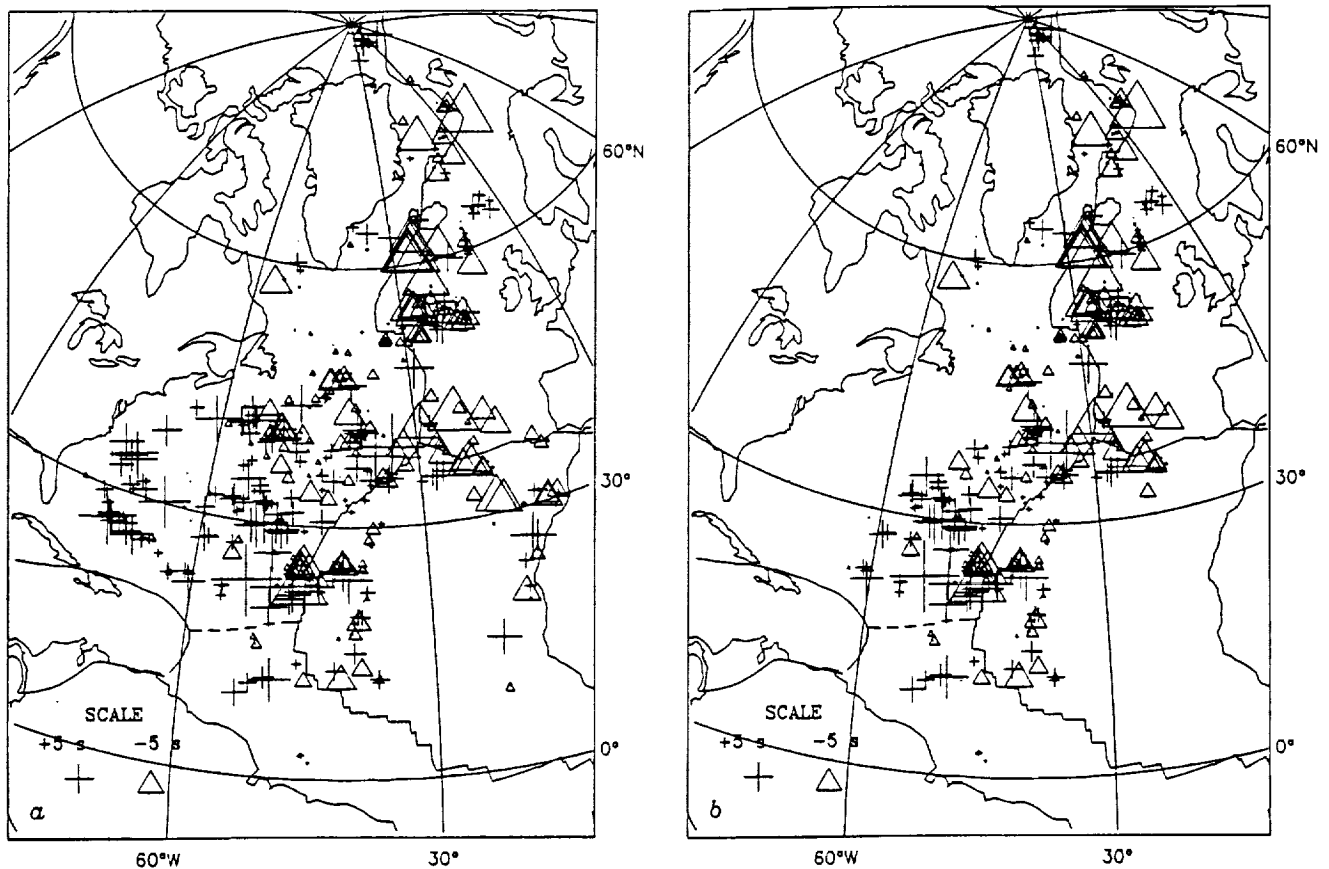


Fig. 6. (a) Map view of age-corrected SS-S residuals. (b) Same as Figure 6a but including data only with SS bounce points on lithosphere younger than 100 Ma.

There is a systematic variation of SS-S residual with latitude, i.e., effectively along the direction of the Mid-Atlantic Ridge axis. Age-corrected SS-S residuals with SS bounce points on lithosphere younger than 100 Ma are shown versus latitude in Figure 8. The along-axis variations show a variety of scales, notably at wavelengths of about 1000–2000 km in the region from 15° to 35°N, and at about 6000 km wavelength from late (positive residuals) in the south (20°–35°) to early (negative residuals) farther north (45°–55°N). The largest of these variations are robust with respect to selective removal of portions of the data. The Iceland region appears as a local maximum (positive SS-S delay) on the profile, but the Azores hotspot does not have a distinct seismic signal.

JOINT INVERSION OF TRAVEL TIME RESIDUALS AND GEOID AND DEPTH ANOMALIES

Long-wavelength variations in shear wave velocity of the sort depicted in Figure 8 presumably are a consequence of some combination of variations in temperature and composition of the upper mantle. Such lateral variations should also have signatures in other physical quantities measurable at these wavelengths, notably gravity (or geoid height) and topography (or residual bathymetry), because of the dependence of these quantities on bulk density. Travel time residuals, geoid anomalies, and residual depth anomalies are independent quantities dependent in different ways on temperature, bulk composition, and their variation with depth. We therefore seek a quantitative procedure for treating

travel time residuals jointly with geoid and bathymetry data and in particular for a combined inversion of all three quantities for horizontal variations in upper mantle temperature and composition.

To ensure complementarity of data sets, bathymetry and geoid height values are obtained at each SS bounce point, and both are corrected for subsidence with seafloor age by means of the plate cooling model [Parsons and Sclater, 1977; Parsons and Richter, 1980]. In this manner we effectively normalize all observations to zero age. Bathymetric data are obtained from the corrected Digital Bathymetric Data Base (5 arc min grid) [U.S. Naval Oceanographic Office, 1985]. Geoid data are taken from a combined set of Seasat and GEOS 3 altimeter data [Marsh *et al.*, 1986]. Data north of 70°N were not included in the Marsh *et al.* [1986] data set due to the high probability of being over sea ice, so our analysis below is confined to latitudes less than 70°N. We find that the correlation of SS-S residuals with the low-order geoid is negative but that at high order the correlation is positive (Figure 9). This relationship may indicate a depth dependence of contributions to geoid and travel time (e.g., the long-wavelength signal may be a lower mantle effect). Low-degree harmonics are likely linked to deep-seated density heterogeneities and subducting slabs [Hager, 1984; Hager *et al.*, 1985]. Since we are interested in upper mantle processes, we filter out the long-wavelength component of the geoid by subtracting a reference field [Lerch *et al.*, 1979] expanded in spherical harmonics to degree and order 7 and tapered to degree and order 11. To provide a comparable

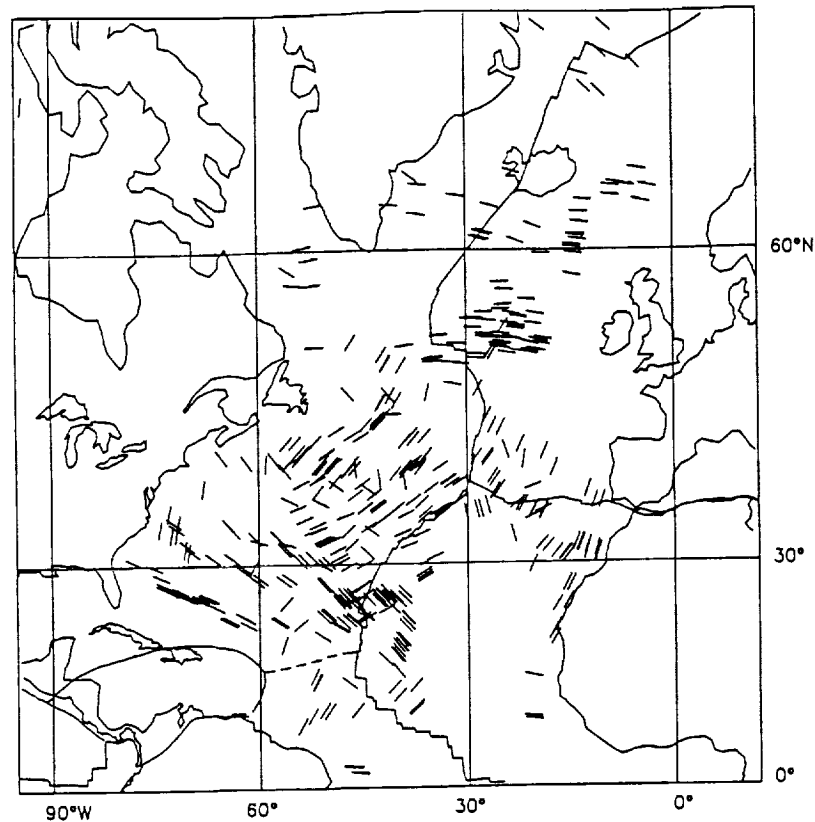


Fig. 7. Map view of the distribution of sampling azimuths. Lines indicate the wave path azimuth at the SS bounce point. Mercator projection.

bathymetric data set, bathymetry is high-pass-filtered (corner at 4000 km, cutoff at 6000 km) to remove long-wavelength trends. Along-axis profiles are constructed from the age-corrected and filtered geoid and bathymetry data. These profiles, of course, are only approximations to true

along-axis variations, but they share many features with similarly filtered geoid and bathymetry profiles obtained from observations along the ridge axis rather than at the SS bounce point locations.

Profiles of age-corrected travel time residuals, geoid, and

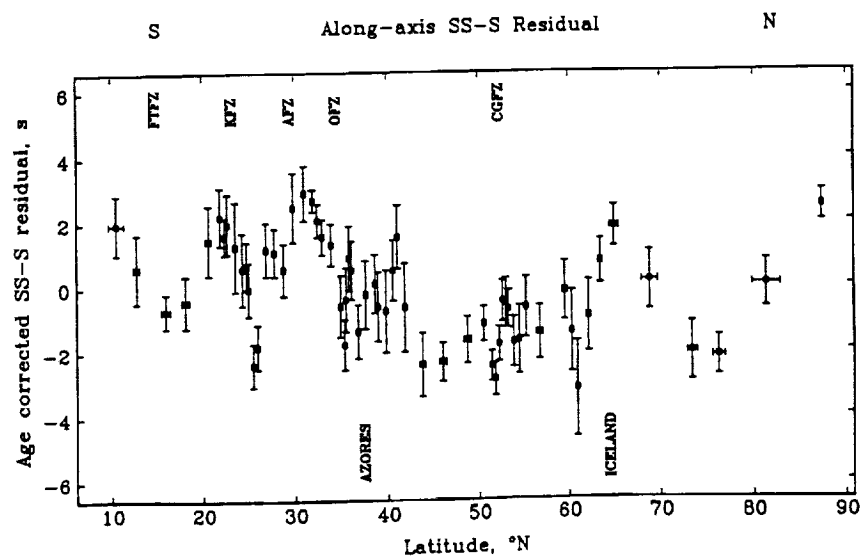


Fig. 8. Age-corrected SS-S residual versus latitude along the Mid-Atlantic Ridge from 10° to 90°N. The residuals shown are moving averages (such that each point is used twice) of 12 adjacent data points. Error bars indicate standard errors of the mean residual and position. Bounce points on lithosphere of age 0–100 Ma are used. The approximate locations of several fracture zones (Fifteen-Twenty, Kane, Atlantis, Oceanographer, and Charlie-Gibbs, denoted by abbreviations) and of the Iceland and Azores hotspots are indicated.

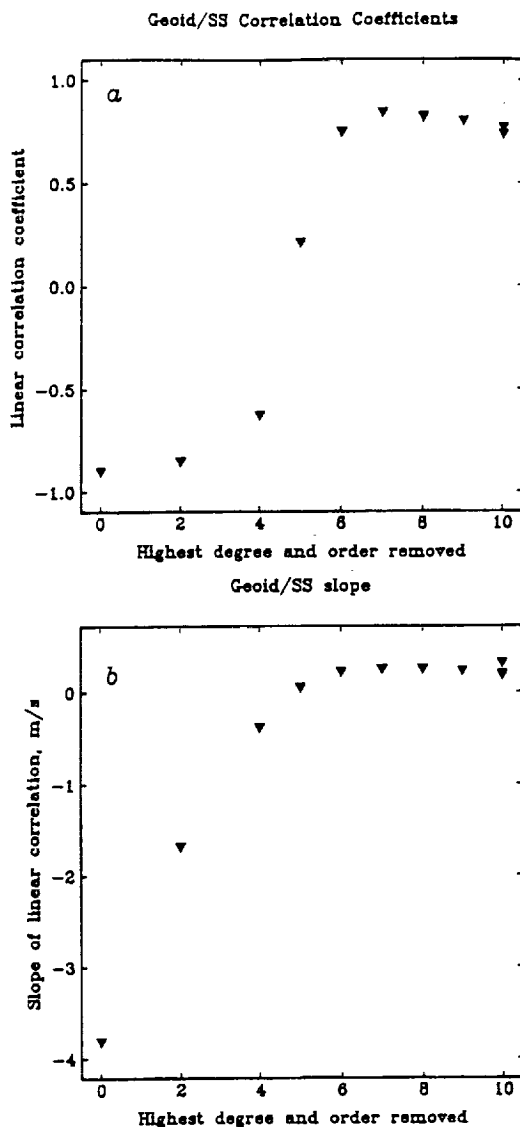


Fig. 9. Linear correlation, by highest harmonic degree removed from the geoid, of observed $SS-S$ residual with geoid height measured at the corresponding SS bounce point. Both travel time and geoid residuals are age-corrected. First, the uncorrected geoid data [Marsh *et al.*, 1986] are correlated with $SS-S$ residuals and a slope and correlation coefficient determined. Then a geoid reference field [Lerch *et al.*, 1979] up to degree and order 2 (with taper to degree and order 6) is calculated and removed from the geoid data, the slope and correlation coefficient with $SS-S$ residuals calculated, and so on for higher harmonic degrees ℓ removed from the geoid data, with appropriate tapers (up to $\ell + 4$). (a) Linear correlation coefficient between geoid and $SS-S$ residuals versus highest harmonic degree and order removed from the geoid. (b) Slope of the correlation between geoid and $SS-S$ residual data, as a function of highest harmonic degree and order removed from the geoid. Extra points at degree and order 10 are obtained by using different tapers (no taper, taper to $\ell = 14$, and taper to $\ell = 15$).

bathymetry are compared in Figure 10. All profiles have been smoothed by applying a running average. While qualitative correlations among profiles are apparent, we seek to quantify possible models of temperature and compositional variations that can match these observations. Oceanic bathymetry and geoid height are both sensitive to variations in mantle density at depth. Such variations can be either thermal or compositional in origin and, like seismic velocity,

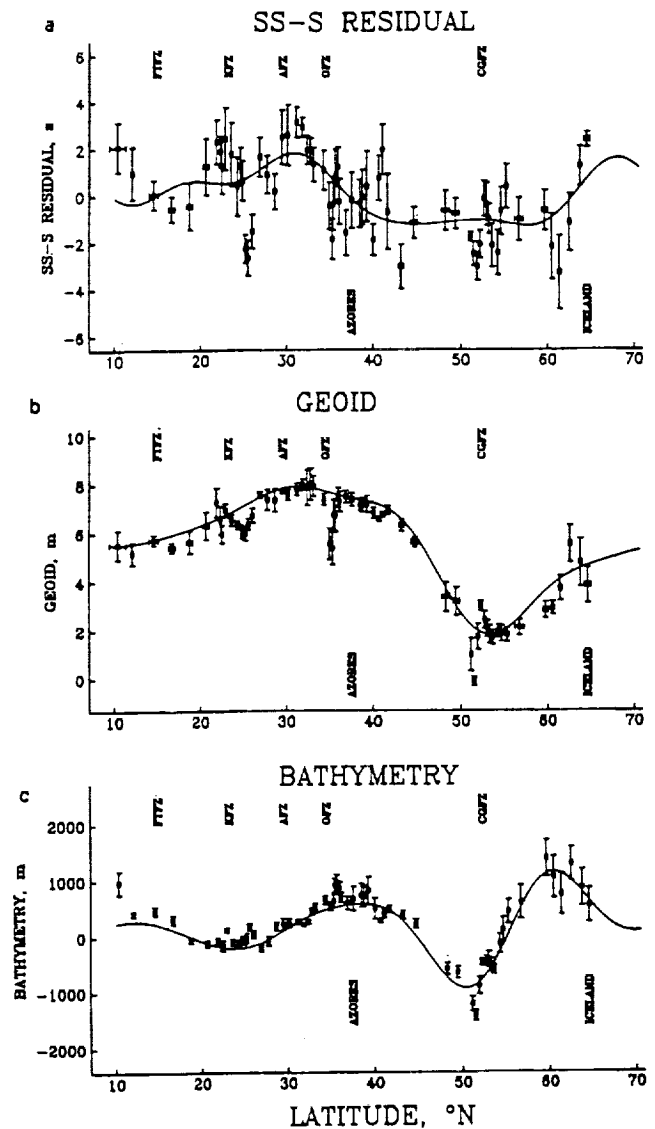


Fig. 10. Comparative plots of age-corrected (a) $SS-S$ residual, (b) geoid, and (c) bathymetry, along the Mid-Atlantic Ridge, 10°–65°N. Bathymetry and geoid have been high-pass-filtered (see text). All of the data points shown are moving averages of 10 adjacent data points. Bounce points from lithosphere of age 0–100 Ma are used, except that data from the Labrador Sea region are omitted. The solid line represents a filtered version of the depicted observations, containing only the wavelengths used in the inversions (1400–7100 km).

are presumably related to mantle convection and differentiation. For a given density change, the seismic signature of thermal and compositional heterogeneity are of opposite sign, so travel time residuals constitute key information for distinguishing between mechanisms of heterogeneity.

Inversion for Thermal Structure

We seek to formulate an inversion for the distribution of temperature anomalies $T(x, z)$ (where x is along-axis and z is depth) that can produce the along-axis geoid, bathymetry, and travel time anomalies shown in Figure 10. Topography and geoid kernels were calculated for prescribed models of viscosity for an incompressible, self-gravitating, Newtonian mantle with free slip at the surface and the core-mantle boundary. The convecting region is assumed to be overlain by a high-viscosity

layer 40 km thick. We performed calculations both for a mantle of constant viscosity and for a mantle with a shallow low-viscosity layer. Topography and geoid anomalies depend on the viscosity structure, but the predicted travel times do not. Kernels were calculated using a method similar to that of *Richards and Hager [1984]* except that the solution was directly integrated across the layers instead of being obtained via propagator matrices [*McNutt and Judge, 1990*].

The inversion is best conducted in the horizontal wavenumber domain. The thermal anomalies $\Delta T(k, z)$ at depth are related to the predicted dynamic topography $h(k)$ for wavenumber k via an integral of the form

$$\Delta h(k) = \frac{\rho_0 \alpha}{\rho_0 - \rho_w} \int_{z_{\min}}^{z_{\max}} H(k, z) \Delta T(k, z) dz \quad (3)$$

[*Parsons and Daly, 1983*], where α is the volumetric coefficient of thermal expansion, ρ_0 and ρ_w are the densities of the mantle and of water at standard temperature and pressure, and z_{\min} and z_{\max} are the upper and lower boundaries of the layer in which temperatures are allowed to vary. Table 1 contains a summary of the constants adopted here. The depth- and wavenumber-dependent topography kernel $H(k, z)$ is calculated from the equations of continuity and motion given a set of boundary conditions, a viscosity model, and a constitutive relation between stress and strain [*Parsons and Daly, 1983*]. Similarly, the kernel $G(k, z)$ for the geoid relates the thermal anomalies to the geoid $N(k)$ via

$$\Delta N(k) = \frac{2\pi\Gamma\rho_0\alpha}{gk} \int_{z_{\min}}^{z_{\max}} G(k, z) \Delta T(k, z) dz \quad (4)$$

[*Parsons and Daly, 1983*], where Γ is the gravitational constant and g is the surface gravitational acceleration.

Sample geoid and topography kernels calculated for different wavenumbers and viscosity structures are shown in Figures 11 and 12. Cartesian kernels are used throughout this study because of their computational efficiency and straightforward application to Fourier transform techniques. We have compared extrema of the upper mantle portions of the geoid and topography kernels for a layered Cartesian Earth and a spherical Earth for a number of wavelengths and different viscosity structures (Figure 12), and we note good agreement even at very long wavelengths (spherical harmonic order $\ell = 6$). This agreement suggests that the results presented here should be applicable to the spherical Earth without introducing unreasonably large errors.

Temperature perturbations at depth can be converted to seismic velocity perturbations by assuming a value for the partial derivative of shear wave velocity with respect to temperature, $\partial v_s / \partial T$. The resulting two-way travel time perturbation is given by

$$\Delta t(k) = 2 \frac{\partial v_s}{\partial T} \int_{z_{\min}}^{z_{\max}} \frac{\Delta T(k, z) dz}{v_s(z)^2 [1 - p^2 v_s(z)^2]^{1/2}} \quad (5)$$

where $v_s(z)$ is from the reference shear velocity model [*Dziewonski and Anderson, 1981*] and p is the ray parameter, generally taken to be a representative value for the range of epicentral distances considered here. We use a value of $-0.6 \text{ m s}^{-1} \text{ K}^{-1}$ for $\partial v_s / \partial T$. This value is more negative than the values of *Anderson et al. [1968]* and *Kumazawa and Anderson [1969]* at standard temperature and pressure but is

similar to the value of $-0.62 \text{ m s}^{-1} \text{ K}^{-1}$ determined by *McNutt and Judge [1990]* by a least squares fit of Love wave phase velocities to predicted temperature of the lithosphere. Such a value is consistent with the change in P wave velocity with temperature, $\partial v_p / \partial T = -0.5 \text{ m s}^{-1} \text{ K}^{-1}$, found from modeling wave propagation along subducting slabs [*Creager and Jordan, 1986; Fischer et al., 1988*] if we assume that $\partial v_s / \partial T = 1.1 \partial v_p / \partial T$ [*Woodhouse and Dziewonski, 1984*]. Partial melt would increase the value of $\partial v_s / \partial T$ [*Sleep, 1974; Sato and Sacks, 1989*], but simultaneous analysis of both shear and compressional differential travel times by *Woodward and Masters [1991a]* indicates that significant partial melting is not required to explain the differential travel time residuals in the North Atlantic region.

The forward problem consists of calculating geoid, topography, and travel time residual profiles given a starting two-dimensional temperature structure $T(x, z)$. The inverse problem consists of finding a temperature structure that predicts (via equations (3)–(5)) geoid, topography, and travel time profiles which best fit those observed. The familiar matrix equation $\mathbf{d} = \mathbf{A} \mathbf{m}$ is formed from discrete versions of equations (3)–(5). The data vector \mathbf{d} consists of the topography, geoid, and travel time residuals, the model vector \mathbf{m} contains the temperature variations for which we are solving, and the matrix \mathbf{A} contains the coefficients and kernels which relate the data to the model. As a check on our procedure, we constructed a forward problem for geoid and topography and found good agreement with the modelling results of *McKenzie et al. [1980]*.

The observed profiles of bathymetry, geoid, and travel time are interpolated to a constant spacing, demeaned, tapered at both ends with a 10% sine squared taper, and Fourier transformed (Figure 10). Since the profiles for which these operations were performed extend from 10° to 72°N , the first and last 10% of the profile (10° – 16°N and 66° – 72°N) will be affected by the taper. The $3n \times 1$ data vector \mathbf{d} is then constructed, using the complex (to retain both amplitude and phase) bathymetry, geoid, and travel time data sampled at n discrete wavenumbers:

$$\mathbf{d} = [\Delta h(k_1), \dots, \Delta h(k_n),$$

$$\Delta N(k_1), \dots, \Delta N(k_n), \Delta t(k_1), \dots, \Delta t(k_n)]^T \quad (6)$$

where T denotes transpose and n in our problem is equal to 5, representing the first five coefficients of the Fourier series expansion (wavelengths of 7104, 3552, 2368, 1776, and 1420 km). For the case where temperature perturbations are constrained to be in a single layer, the $n \times 1$ model vector \mathbf{m} is given by

$$\mathbf{m} = [\Delta T(k_1), \dots, \Delta T(k_n)]^T \quad (7)$$

For the more general case of a multilayer system, the $n_j \times 1$ model vector \mathbf{m} is given by

$$\mathbf{m} = [\Delta T(k_1, z_1), \dots, \Delta T(k_1, z_j), \Delta T(k_2, z_1), \dots,$$

$$\Delta T(k_2, z_j), \dots, \Delta T(k_n, z_1), \dots, \Delta T(k_n, z_j)]^T \quad (8)$$

where z_i is the layer index and j is the total number of layers. In this paper we perform inversions for single-layer models only. The "layers" of temperature variations are independent of the "layering" system of lid, low-viscosity zone, and mantle

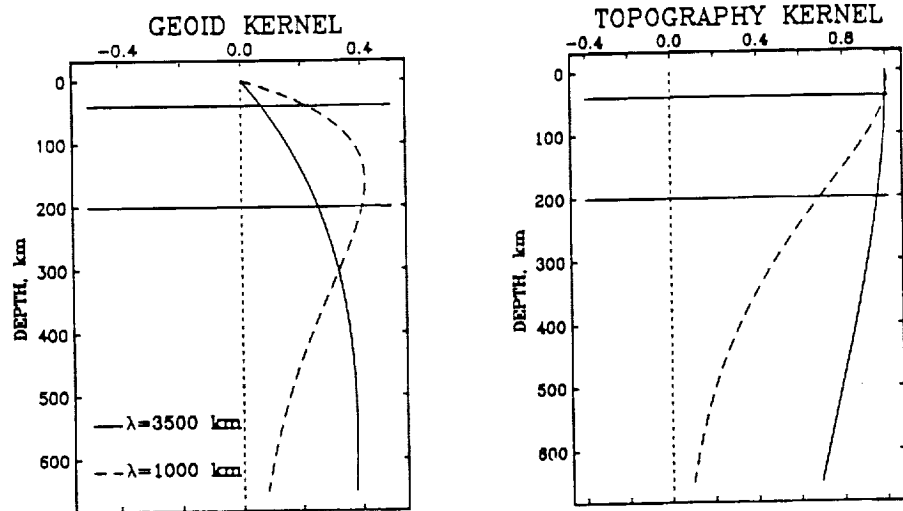
TABLE 1. Adopted Constants

Variable	Description	Value
α	volumetric coefficient of thermal expansion	$2.5 \times 10^{-5} \text{ K}^{-1}$ *
ρ_0	average mantle density	3300 kg m^{-3}
ρ_w	density of seawater	1000 kg m^{-3}
Γ	gravitational constant	$6.67 \times 10^{-11} \text{ N m}^2 \text{ kg}^{-2}$
g	surface gravitational acceleration	9.8 m s^{-2}
$\partial v_s / \partial T$	thermal coefficient of shear velocity	$-6.0 \times 10^{-4} \text{ km s}^{-1} \text{ K}^{-1}$
$\partial v_s / \partial Mg$	variation of shear velocity with Mg #	$1.8 \times 10^{-2} \text{ km s}^{-1} \text{ Mg}^{-1}$ †
$\partial \rho / \partial Mg$	variation of density with Mg #	$-12 \text{ kg m}^{-3} \text{ Mg}^{-1}$ †
p	average SS ray parameter at 70°	0.1375 s km^{-1}

*Stacey [1977] and Duffy and Anderson [1989].

†Akimoto [1972].

(a) CONSTANT VISCOSITY



(b) LOW VISCOSITY LAYER

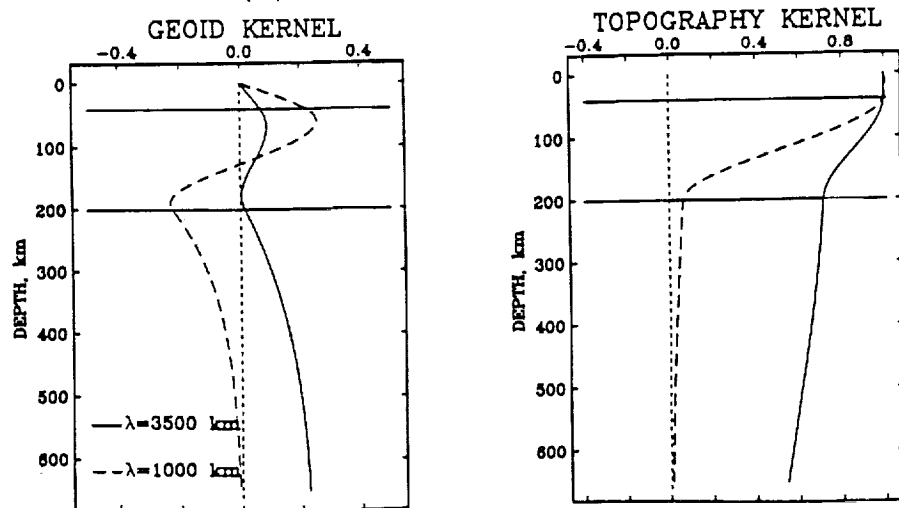


Fig. 11. Upper mantle portion of the kernels for geoid and topography at two wavelengths $\lambda = 2\pi/k$ for two viscosity models. The convecting region in both models is overlain by a high-viscosity layer 40 km thick, with viscosity 10^4 that of the underlying mantle. (a) High-viscosity lid is underlain by a mantle of uniform viscosity and other physical parameters. (b) High-viscosity lid is underlain by a zone extending to a depth of 200 km having a viscosity equal to 0.01 that of the underlying mantle.

which we use for the calculation of kernels, although major changes in viscosity would tend to segment ΔT as well. The temperature layering simply refers to that region bounded by z_{\min} and z_{\max} in the integrals of equations (1)–(3).

The $3n \times n$ matrix A contains the coefficients and kernels that relate the temperature perturbations to the observations, which for the single-layer case is given by

$$A = \begin{pmatrix} \frac{\rho_0 \alpha}{\rho_0 - \rho_w} \sum_{z=z_{\min}}^{z_{\max}} H(k_1, z) \Delta z & 0 & \cdots & 0 \\ 0 & \frac{\rho_0 \alpha}{\rho_0 - \rho_w} \sum_{z=z_{\min}}^{z_{\max}} H(k_2, z) \Delta z & \cdots & 0 \\ 0 & 0 & \ddots & 0 \\ 0 & 0 & \cdots & \frac{\rho_0 \alpha}{\rho_0 - \rho_w} \sum_{z=z_{\min}}^{z_{\max}} H(k_n, z) \Delta z \\ \frac{2\pi\Gamma\rho_0\alpha}{gk_1} \sum_{z=z_{\min}}^{z_{\max}} G(k_1, z) \Delta z & 0 & \cdots & 0 \\ 0 & \frac{2\pi\Gamma\rho_0\alpha}{gk_2} \sum_{z=z_{\min}}^{z_{\max}} G(k_2, z) \Delta z & \cdots & 0 \\ 0 & 0 & \ddots & 0 \\ 0 & 0 & \cdots & \frac{2\pi\Gamma\rho_0\alpha}{gk_n} \sum_{z=z_{\min}}^{z_{\max}} G(k_n, z) \Delta z \\ 2 \frac{\partial v_s}{\partial T} \sum_{z=z_{\min}}^{z_{\max}} \frac{v_s(z)^{-2}}{[1 - p^2 v_s(z)^2]^{1/2}} \Delta z & 0 & \cdots & 0 \\ 0 & 2 \frac{\partial v_s}{\partial T} \sum_{z=z_{\min}}^{z_{\max}} \frac{v_s(z)^{-2}}{[1 - p^2 v_s(z)^2]^{1/2}} \Delta z & \cdots & 0 \\ 0 & 0 & \ddots & 0 \\ 0 & 0 & \cdots & 2 \frac{\partial v_s}{\partial T} \sum_{z=z_{\min}}^{z_{\max}} \frac{v_s(z)^{-2}}{[1 - p^2 v_s(z)^2]^{1/2}} \Delta z \end{pmatrix} \quad (9)$$

The matrix A contains both bathymetry and topography kernels and is thus viscosity dependent; that is, a viscosity structure must be assumed. We solve the equation $\bar{d} = A\mathbf{m}$ by least squares

$$\mathbf{m} = (\bar{A}R_{dd}^{-1}A)^{-1}\bar{A}R_{dd}^{-1}\bar{d} \quad (10)$$

where \bar{A} is the complex conjugate transpose of the matrix A . Construction of the data covariance matrix R_{dd} is discussed in Appendix B. Equation (10) is solved for the solution vector \mathbf{m} , and variance reduction is calculated via

$$\text{variance reduction} = 1 - \frac{(\bar{d} - A\mathbf{m})R_{dd}^{-1}(\bar{d} - A\mathbf{m})}{\bar{d}R_{dd}^{-1}\bar{d}} \quad (11)$$

The resulting model vector \mathbf{m} is inverse Fourier transformed back to the spatial domain to produce an along-axis temperature profile. The solution \mathbf{m} is also substituted into equations (3)–(5) to compare predicted geoid, bathymetry, and travel time residuals with those observed.

To assess how well the various data are being fit, reduced χ^2 values are calculated in the spatial domain from

$$\chi^2_\nu = \frac{\sum_{i=1}^N \frac{1}{\sigma_i^2} (y_{oi} - y_{pi})^2}{\nu} \quad (12)$$

where $\nu = N - p$ is the number of degrees of freedom, N is the number of data points, p is the number of parameters being fit, σ_i^2 is the estimated variance of the data (see Appendix B), and y_p and y_o are the predicted and observed values of the smoothed profiles, respectively. If the model is a good fit to the observations, then χ^2_ν should be approximately unity. A χ^2_ν greater than 1 indicates a poorer fit. A value of χ^2_ν less than 1 does not necessarily indicate a physically meaningful improvement in fit, however; it can

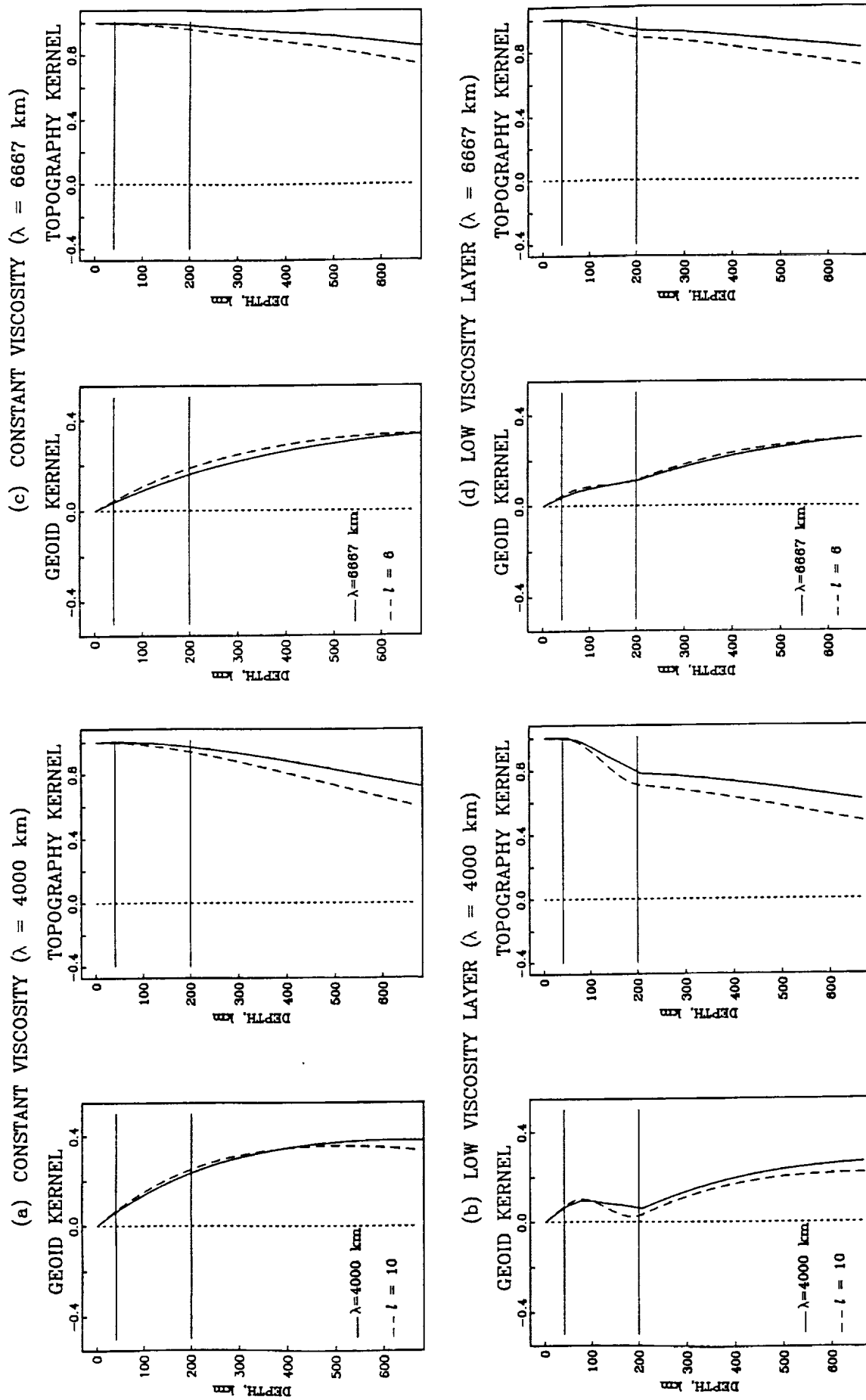


Fig. 12. Upper mantle portion of the kernels for geoid and topography at two wavelengths in spherical versus Cartesian coordinates. The convecting region is overlain by a high-viscosity layer 40 km thick in each of two models for viscosity structure. (a) Underlying mantle is of uniform viscosity. Cartesian kernels are for 4000-km wavelength (solid lines) and spherical kernels are for $l = 10$ (dashed lines). (b) High-viscosity lid is underlain by zone extending to 200 km depth having a viscosity equal to 0.01 that of the underlying mantle. Cartesian kernels are for 4000-km wavelength and spherical kernels are for $l = 10$. (c) Same as Figure 12a but with Cartesian kernels for 6667-km wavelength and spherical kernels for $l = 6$. (d) Same as Figure 12b but with Cartesian kernels for 6667-km wavelength and spherical kernels for $l = 6$.

TABLE 2. Inversion Models and Measures of Fit

Layer Thickness, km	Viscosity Structure*	ΔT Range, K	ΔMg # Range	Variance Reduction, %				Reduced χ^2 Values			
				Total	Bathymetry	Geoid	SS-S	Total	Bathymetry	Geoid	SS-S
Temperature Variations Only											
0-150	cvm	180		53	25	79	58	1.82	2.90	0.72	1.84
0-150	lvz	230		57	27	79	66	1.68	2.83	0.72	1.49
0-300	cvm	60		47	21	85	41	2.05	3.09	0.49	2.57
0-300	lvz	110		57	24	85	65	1.65	2.94	0.49	1.51
0-650	cvm	20		41	14	91	25	2.30	3.33	0.29	3.27
0-650	lvz	33		49	17	83	51	1.96	3.21	0.55	2.11
Compositional Variations Only											
0-150	cvm		1.1	33	46	74	-9	2.60	2.12	0.89	4.80
0-150	lvz		2.4	44	75	76	-9	2.19	0.98	0.81	4.76
0-300	cvm		0.4	33	29	87	-6	2.62	2.78	0.43	4.65
0-300	lvz		1.3	43	73	73	-7	2.22	1.03	0.92	4.71
0-650	cvm		0.1	32	19	93	-3	2.63	3.16	0.22	4.52
0-650	lvz		0.5	49	65	86	+5	1.99	1.33	0.46	4.17
Thermal and Compositional Variations in Same Layer											
0-150	cvm	210	1.5	75	44	78	100	1.01	2.24	0.78	0.00
0-150	lvz	235	2.1	86	75	80	100	0.56	1.01	0.69	0.00
0-300	cvm	110	0.7	73	28	89	100	1.09	2.88	0.39	0.00
0-300	lvz	125	1.1	84	74	76	100	0.62	1.03	0.83	0.00
0-650	cvm	55	0.4	71	18	94	100	1.15	3.27	0.20	0.00
0-650	lvz	60	0.8	85	66	88	100	0.58	1.33	0.42	0.00
Thermal Inversion in Layers as Noted, Compositional Variations 0-50 km Only											
0-150	cvm	210	5.5	84	83	77	91	0.63	0.66	0.81	0.42
0-150	lvz	240	4.5	85	85	70	96	0.60	0.60	1.04	0.16
0-300	cvm	80	5.9	80	84	86	72	0.80	0.64	0.50	1.27
0-300	lvz	120	4.7	86	90	77	89	0.56	0.39	0.80	0.48
0-650	cvm	25	6.0	73	85	92	47	1.07	0.59	0.27	2.35
0-650	lvz	35	4.6	75	82	73	71	0.98	0.72	0.95	1.29

*cvm, constant viscosity mantle; lvz, mantle with low-viscosity zone.

simply be a consequence of overfitting data more closely than the estimated variance. χ^2_v values were calculated for all three data types simultaneously as well as for each individual data type. In the estimation of overall χ^2_v , N is equal to the sum of the number of data in the three different profiles (residual geoid and bathymetry and differential travel time). In the estimation of χ^2_v values for individual profiles, N is the number of data points and p is equal to one third the number of parameters used in the inversion, since the χ^2_v value is being calculated using only one third the data going into the inversion.

Six inversion experiments for temperature structure were performed (Table 2). Inversions were carried out for two different viscosity models and for three different thicknesses of the layer in which lateral temperature variations were assumed to occur. Because topography and geoid anomalies depend only on the ratios of viscosity in different layers [Richards and Hager, 1984; Robinson *et al.*, 1987; Hong *et al.*, 1990], we set the dimensionless viscosity of the layer representing the bulk of the mantle to unity. In one viscosity model, termed the "constant viscosity mantle," a 40-km-thick high-viscosity lid overlies a unit viscosity mantle. We set the viscosity in the lid to 10^4 , which effectively mimics rigid behavior. In a second model, a 160-km-thick low-viscosity zone is present beneath a 40-km-thick lid; the viscosity in the low-viscosity zone is a factor of 100 less than in the underlying mantle. The thickness of the layer of temperature perturbations was taken variously to extend from 0 to 150 km depth, 0 to 300 km depth, and 0 to 650 km depth. The matrix A is different for each of these cases, as it

involves viscosity-dependent geoid and topography kernels and also a summation over depth. Since the geoid and bathymetry kernels do not include any phase information (except that a sign change produces a 180° phase shift), large differences in phase between the observed profiles of geoid and bathymetry would indicate that these components cannot simultaneously be well fit by our models. Spectral coefficients for both the filtered profiles and models are given by Sheehan [1991] and serve to indicate how well the various spectral components of the data are fit.

Inversion results for the constant-viscosity-mantle cases are shown in Figure 13. Predicted profiles for each inversion solution were calculated from equation (5). For these solutions, the long-wavelength fit to the geoid is better than at short wavelengths. The fit to bathymetry is poor. The predicted magnitude of the SS-S residuals range from a factor of 5 too small for the 650-km-thick layer to a factor of about 1.5 too small for the 150-km-thick layer. Increasing the temperature variations to improve the fit to the SS-S residuals leads to predicted geoid variations that are too large. The highest total variance reduction and best fit for the constant-viscosity cases come when lateral variations are constrained to shallow (0-150 km) depth. The variance reduction is 25% for bathymetry, 79% for geoid, and 58% for travel times, and the reduced χ^2 values are 2.9 for bathymetry, 0.7 for geoid, and 1.8 for travel times (Table 2). The total variance reduction is 53%, and the total χ^2_v value is 1.8. The variation in temperature is 180 K for the 150-km-thick layer and only 60 K for the 300-km-thick layer.

Figure 14 shows inversion results for the models with a

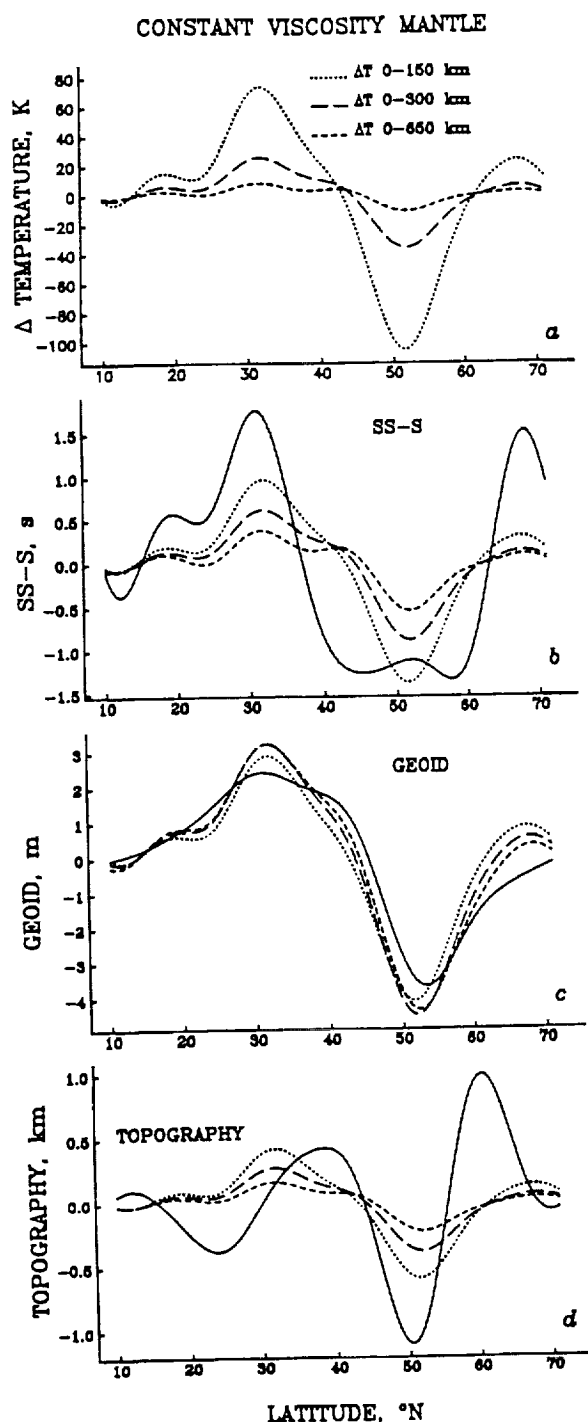


Fig. 13. Results of combined inversion of geoid, bathymetry, and SS-S travel time residuals for upper mantle temperature variations. The viscosity structure is taken to consist of a 40-km-thick high-viscosity lid overlying a constant-viscosity half-space. (a) Three solutions for along-axis temperature variations: Dotted line indicates temperature perturbations constrained to be uniform over 0–150 km depth. Long-dashed line indicates temperature perturbations constrained to be uniform over 0–300 km depth. Short-dashed line indicates temperature perturbations constrained to be uniform over 0–650 km depth. (b) Observed (solid line) and predicted along-axis profiles of SS-S travel time residual. The “observed” profile is the filtered profile of Figure 10 and contains only the wavelengths used in the inversion (1400–7100 km). Predicted profiles were calculated from equation (5). Line types correspond to those of the temperature models. (c) Observed and predicted along-axis geoid profiles. Same treatment as in Figure 13b. (d) Observed and predicted along-axis bathymetry profiles. Same treatment as in Figure 13b.

thin low-viscosity zone. A good fit to both geoid and travel time is found, although the alignment in phase of predicted and observed geoid is not as good as for the constant-viscosity case. The fit to bathymetry is again poor. The total variance reduction for the 150-km-thick and 300-km-thick layers are both 57% (χ^2_v values are 1.68 and 1.65, respectively), so the total fit is slightly better for the 300-km-thick layer), although the shallow model provides slightly higher variance reduction for bathymetry (27% for 0–150 km deep layer, 24% for 0–300 km deep layer; χ^2_v values of 2.8 and 2.9, respectively) and the 300-km-thick-layer model provides higher variance reduction for geoid (79% for 0–150 km deep layer, 85% for 0–300 km deep layer; χ^2_v values of 0.7 and 0.5, respectively). The variation in temperature for the 150-km-thick layer is 230 K and in the 300-km-thick layer is 110 K.

We have explored the hypothesis that the lack of correlation of predicted and observed topography is an indication that the source of variations in the geoid and travel time anomalies is deep. To test this hypothesis, we performed inversions with temperature variations restricted to deeper layers and found that fits to topography were still poor. It is possible that the bathymetric signal is dominated by crustal thickness variations which are not included in our calculation of dynamic topography. An assessment of such thickness variations is discussed further in Appendix B.

Inversion for Compositional Variations

A possible alternative to along-axis variation in mantle temperature is lateral variation in bulk mantle composition, due perhaps to a variable extent of melt extraction or different degrees of mixing of compositionally distinct volumes of mantle material. The dynamical effects of compositionally induced density variations can be large [O'Hara, 1975; Boyd and McCallister, 1976; Oxburgh and Parmentier, 1977; Sotin and Parmentier, 1989]. The fraction of mantle potentially extractable as basaltic melt is thought to be 15–25% [e.g., Green and Liebermann, 1976]. Thus, for every volume of basalt removed from the mantle, a volume of residuum several times larger is left behind. The effect of basalt depletion is to increase the molar ratio $Mg/(Mg + Fe)$ (or $Mg \#$) in the residuum, which reduces the density and increases the seismic velocities [e.g., Liebermann, 1970; Akimoto, 1972]. For example, subtraction of 20 mol % olivine basalt from pyrolite can decrease the density of the residuum by nearly 2%, equivalent to a thermal perturbation of nearly 500 K [Jordan, 1979]. Thus compositional changes need only be slight to produce effects of the order of 100 K, comparable to values obtained from the inversions for temperature variations. In this section we explore the effects of compositional variations parameterized in terms of the variation in the $Mg \#$ in the upper mantle along the ridge. Our motivation for parameterizing compositional variations simply in terms of $Mg \#$ is that differences in this quantity yield significant variations in seismic velocity and density, in contrast to most other measures of degree of melt extraction.

Partial derivatives of density and seismic velocity with respect to $Mg \#$ are those for olivine, obtained from Akimoto [1972]. These values were measured on a suite of samples ranging from pure forsterite (Mg_2SiO_4) to pure fayalite (Fe_2SiO_4). While these partial derivatives are at standard temperature and pressure, it is expected that a change to elevated temperature and pressure will have only a second

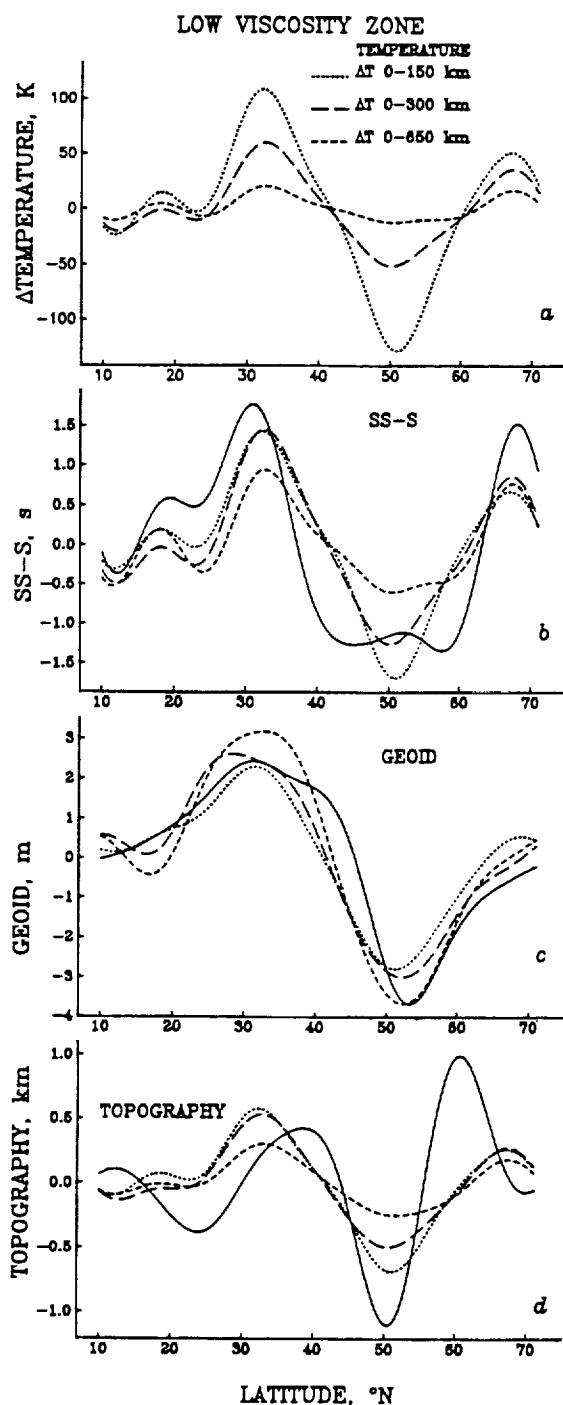


Fig. 14. Same as Figure 13 except for that the viscosity structure includes a zone extending from the base of the lid to a depth of 200 km with a viscosity equal to 0.01 that of the underlying mantle.

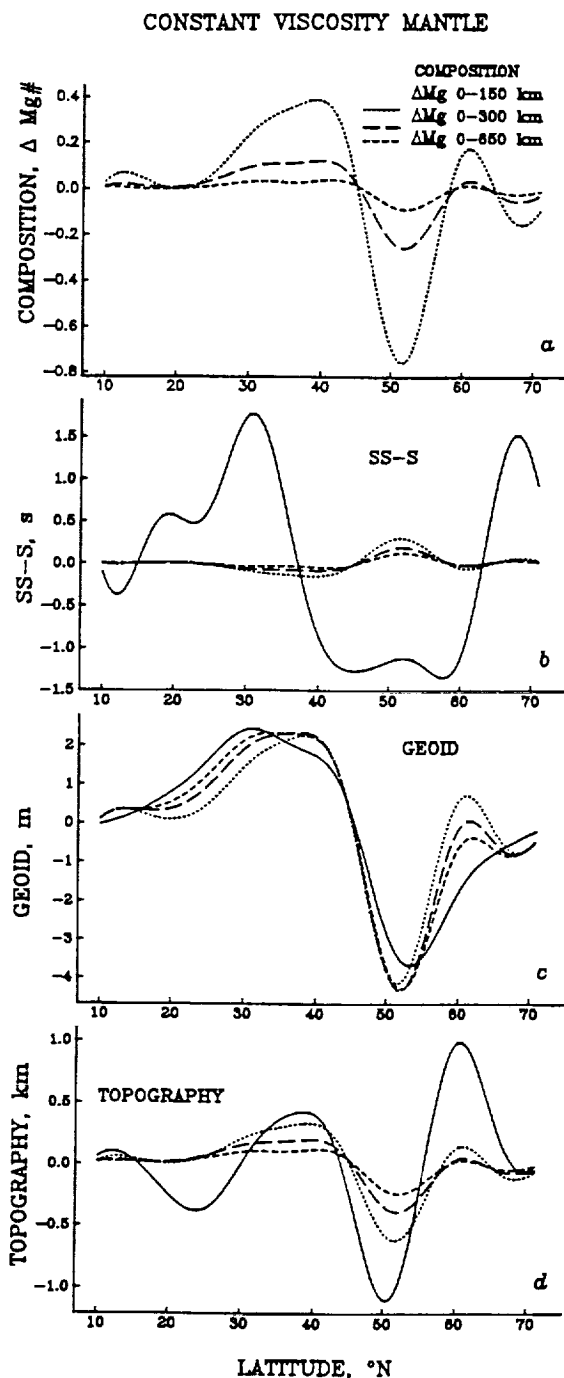


Fig. 15. Results of combined inversion of geoid, bathymetry, and SS-S travel time residuals for variations in upper mantle composition (Mg #). The viscosity structure is taken to consist of a 40-km-thick high-viscosity lid overlying a constant-viscosity half-space. (a) Three solutions for along-axis composition variations: Dotted line indicates composition perturbations constrained to be uniform over 0-150 km depth. Long-dashed line indicates composition perturbations constrained to be uniform over 0-300 km depth. Short-dashed line indicates composition perturbations constrained to be uniform over 0-650 km depth. (b) Observed (solid line) and predicted along-axis profiles of SS-S travel time residual. (c) Observed and predicted along-axis geoid profiles. (d) Observed and predicted along-axis bathymetry profiles.

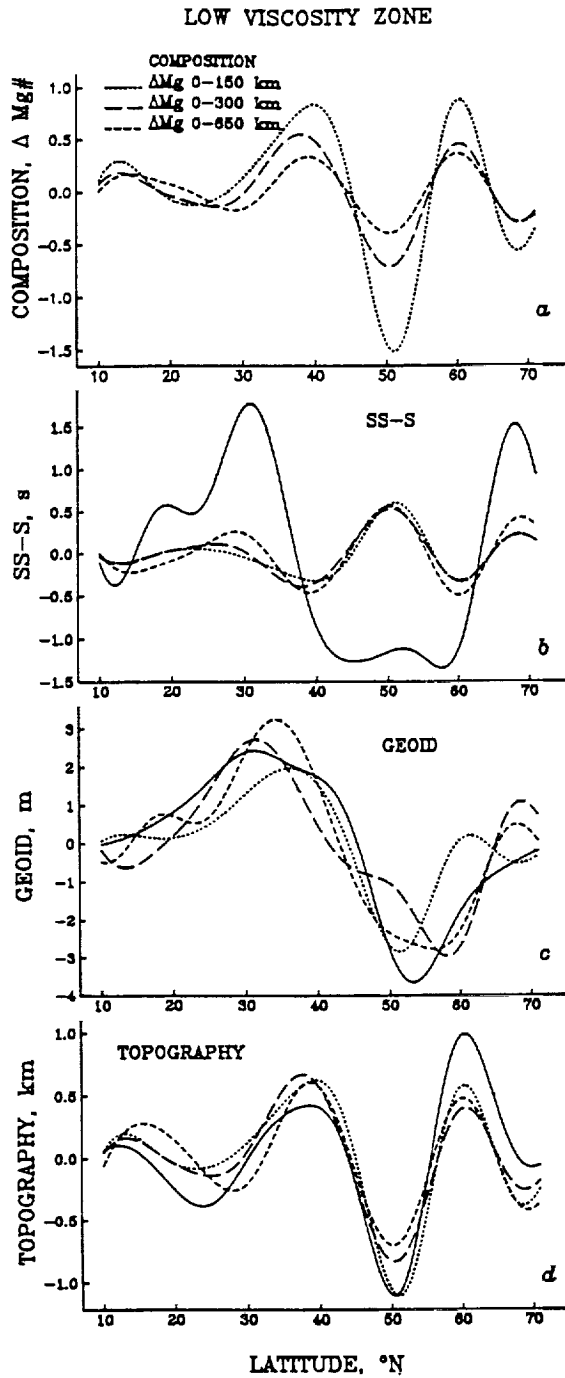


Fig. 16. Same as Figure 15 except for that the viscosity structure includes a zone extending from the base of the lid to a depth of 200 km with a viscosity equal to 0.01 that of the underlying mantle.

order effect, since temperature and pressure corrections work in opposite directions [Jordan, 1979]. Above the solidus temperature, however, the amount and distribution of partial melt, which may depend strongly on composition and particularly volatile content, are important. The presence of melt is likely to have a larger effect on shear wave velocities than on bulk density. Calculations of melt migration, however, suggest that once created, melt segregates rapidly by a percolation mechanism [e.g., Scott and Stevenson, 1989], so that the melt fraction present in the mantle at any given time

is probably small. Studies of mantle peridotites [Johnson *et al.*, 1990] also support the importance of fractional melting.

It is straightforward to convert equations (3) and (4) to relations between geoid or topography and a compositionally induced density perturbation by means of the relation

$$\Delta\rho = -\rho_0\alpha\Delta T \quad (13)$$

Compositional anomalies at depth yield a dynamic topography $h(k)$ given by

$$\Delta h(k) = \frac{1}{\rho_0 - \rho_w} \frac{\partial \rho}{\partial \text{Mg}} \int_{z_{\min}}^{z_{\max}} H(k, z) \Delta \text{Mg}(k, z) dz \quad (14)$$

where ΔMg represents the fractional change in the Mg #. Compositional anomalies yield a geoid anomaly

$$\Delta N(k) = \frac{2\pi\Gamma}{gk} \frac{\partial \rho}{\partial \text{Mg}} \int_{z_{\min}}^{z_{\max}} G(k, z) \Delta \text{Mg}(k, z) dz \quad (15)$$

For a compositional perturbation at depth the resulting two-way travel time perturbation is given by

$$\Delta t(k) = 2 \frac{\partial v_s}{\partial \text{Mg}} \int_{z_{\min}}^{z_{\max}} \frac{\Delta \text{Mg}(k, z) dz}{v_s(z)^2 [1 - \rho^2 v_s(z)^2]^{1/2}} \quad (16)$$

Using equations (14)–(16), an inversion scheme similar to that used for thermal perturbations is formed. The solution vector now has the form

$$\mathbf{m} = [\Delta \text{Mg}(k_1), \dots, \Delta \text{Mg}(k_n)]^T \quad (17)$$

The data vector remains the same as in equation (6), while the matrix of coefficients, \mathbf{A} , changes to reflect the relation between the data and mantle composition, rather than temperature, as outlined in equations (14)–(16).

The results of the inversions for compositional variations are summarized in Table 2 and in Figures 15 and 16. We are unable to match simultaneously both SS-S travel time residuals and geoid and bathymetric anomalies with solely mantle compositional variations for either a constant-viscosity mantle or one with a low-viscosity zone. This is not surprising as the travel times are for the most part positively correlated with geoid and bathymetry, but compositional variations (at least for the $\text{Mg}_2\text{SiO}_4\text{-Fe}_2\text{SiO}_4$ system examined here) have an opposite effect on travel time and geoid-bathymetry. The χ^2_ν values for differential travel time (Table 2) are extremely large (>4), indicating that the fitting function poorly describes the travel time data.

For the constant-viscosity case, the fit to the geoid is excellent, and the fit to bathymetry is slightly better than in the inversion for temperature. The fit to SS-S residuals is so poor that the variance reduction is negative for travel time. Large compositional changes would be required to affect travel times, whereas only small compositional changes are needed to produce significant density contrasts to match the geoid signal. The total variance reduction and χ^2_ν values for the constant viscosity case do not vary greatly (variance reduction from 32 to 33%, χ^2_ν values from 2.60 to 2.63) for compositional changes constrained to be over different depth intervals, although the variance reductions and χ^2_ν values for individual data sets (bathymetry, geoid, travel time) vary

CONSTANT VISCOSITY MANTLE

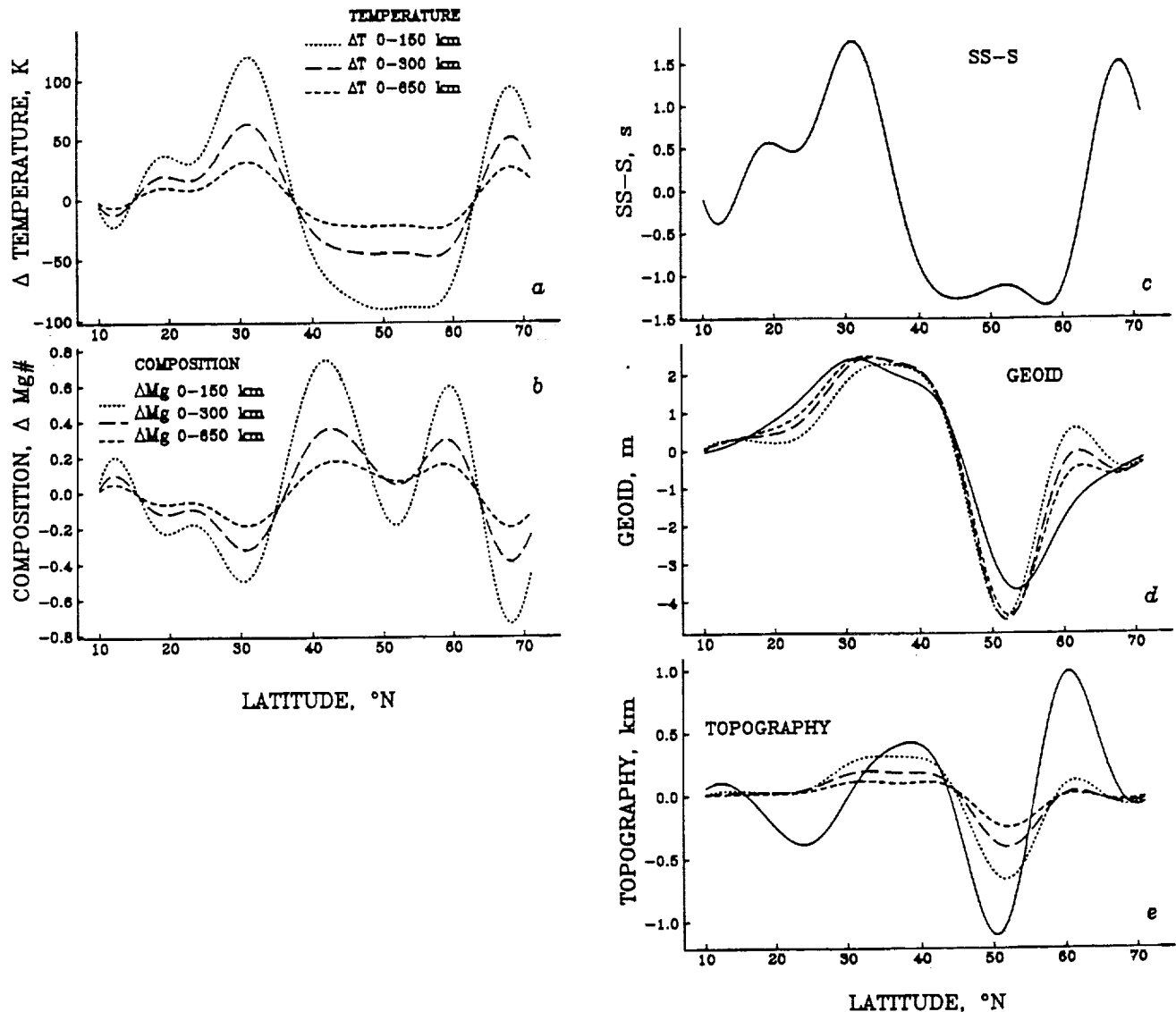


Fig. 17. Results of combined inversion of geoid, bathymetry, and SS-S travel time residuals for both upper mantle temperature and composition variations. The viscosity structure is taken to consist of a 40-km-thick high-viscosity lid overlying a constant-viscosity half-space. (a) Three solutions for along-axis temperature variations: Dotted line indicates composition perturbations constrained to be uniform over 0–150 km depth. Long-dashed line indicates composition perturbations constrained to be uniform over 0–300 km depth. Short-dashed line indicates composition perturbations constrained to be uniform over 0–650 km depth. (b) The corresponding solutions for along-axis composition variations. (c) Observed (solid line) and predicted along-axis profiles of SS-S travel time residual. (d) Observed and predicted along-axis geoid profiles. (e) Observed and predicted along-axis bathymetry profiles.

significantly from model to model (see Table 2). The range in Mg # is about 1% if the variation is constrained to the depth range 0–150 km and only 0.1% for the 0–650 km depth range.

Figure 16 shows inversion results for the model with a low-viscosity zone. A good fit to both geoid and bathymetry is found, although the alignment of predicted and observed geoid is not as good as in the constant-viscosity case. The fit to bathymetry is the best of any models so far. The total variance reduction is still low (43–49%) and total χ^2_p values are high (2.0–2.2), due to the poor fit to travel times (negative variance reduction in all cases except the 0–650 km model).

The range in Mg # is 2.4% if constrained to 0–150 km depth, 1.3% over 0–300 km depth, and 0.5% over 0–650 km depth.

Joint Inversion for Temperature and Composition

We next explore whether a combination of temperature and compositional variations can provide a good match to the observed geoid, travel time, and bathymetry. Joint inversions provide improved fits to all data at the expense of introducing additional free parameters. For these inversions the data vector remains the same as in equation (6), the

LOW VISCOSITY ZONE

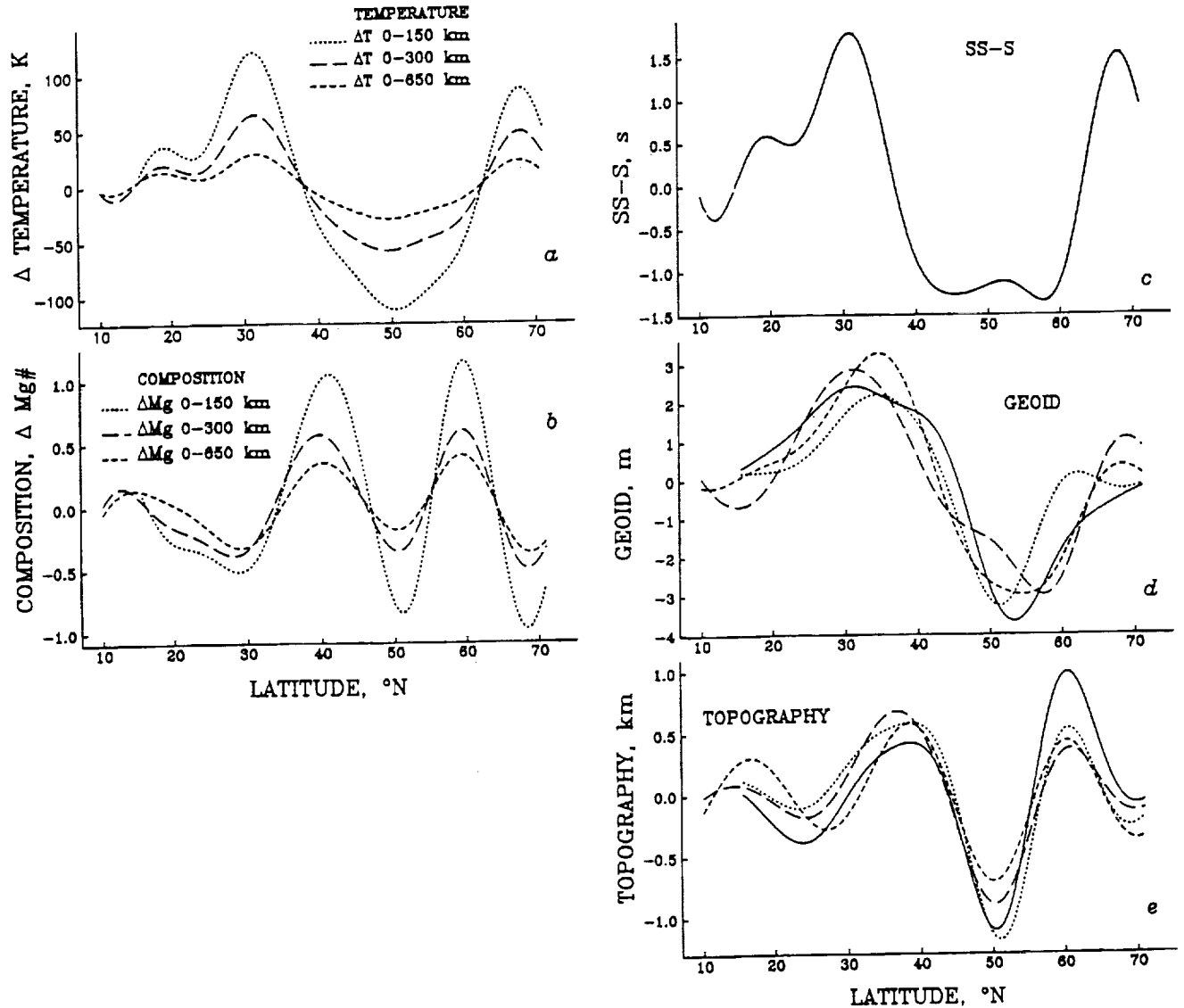


Fig. 18. Same as Figure 17 except for that the viscosity structure includes a zone extending from the base of the lid to a depth of 200 km with a viscosity equal to 0.01 that of the underlying mantle.

solution vector is modified to include both temperature and composition, and the matrix of coefficients, A , includes the effects of both temperature and composition. The matrix-building equations become, for example, for topography,

$$\Delta h(k) = \frac{\rho_0 \alpha}{\rho_0 - \rho_w} \int_{z_{\min}}^{z_{\max}} H(k, z) \Delta T(k, z) dz + \frac{1}{\rho_0 - \rho_w} \frac{\partial \rho}{\partial Mg} \int_{z_{\min}}^{z_{\max}} H(k, z) \Delta Mg(k, z) dz \quad (18)$$

which is simply a combination of equations (3) and (14). The new geoid equation comes from a combination of equations (4) and (15) and the travel time equation from a combination of equations (5) and (16). Cross terms, such as compositional changes induced by increases or decreases in temperature, are neglected.

The travel time residuals are perfectly fit in the joint inversions for temperature and composition (Table 2). This occurs because of the way the model parameters act in a similar manner on both geoid and bathymetry, producing a singular matrix if only geoid and bathymetry data are inverted for both temperature and composition. Undamped least squares always provides perfect solutions when the number of equations is equal to the number of unknowns unless the matrix to be inverted is singular. If we perform an inversion including only travel time and geoid data, we have the same number of equations as unknowns, the matrix is nonsingular, and we obtain perfect fits to both travel time and geoid. Similarly, if we perform an inversion of travel time and bathymetry data, we again obtain perfect fits to both data sets. If we perform an inversion of geoid and bathymetry data, however, we are unable to obtain solutions without applying damping. In the joint inversion of travel

CONSTANT VISCOSITY MANTLE

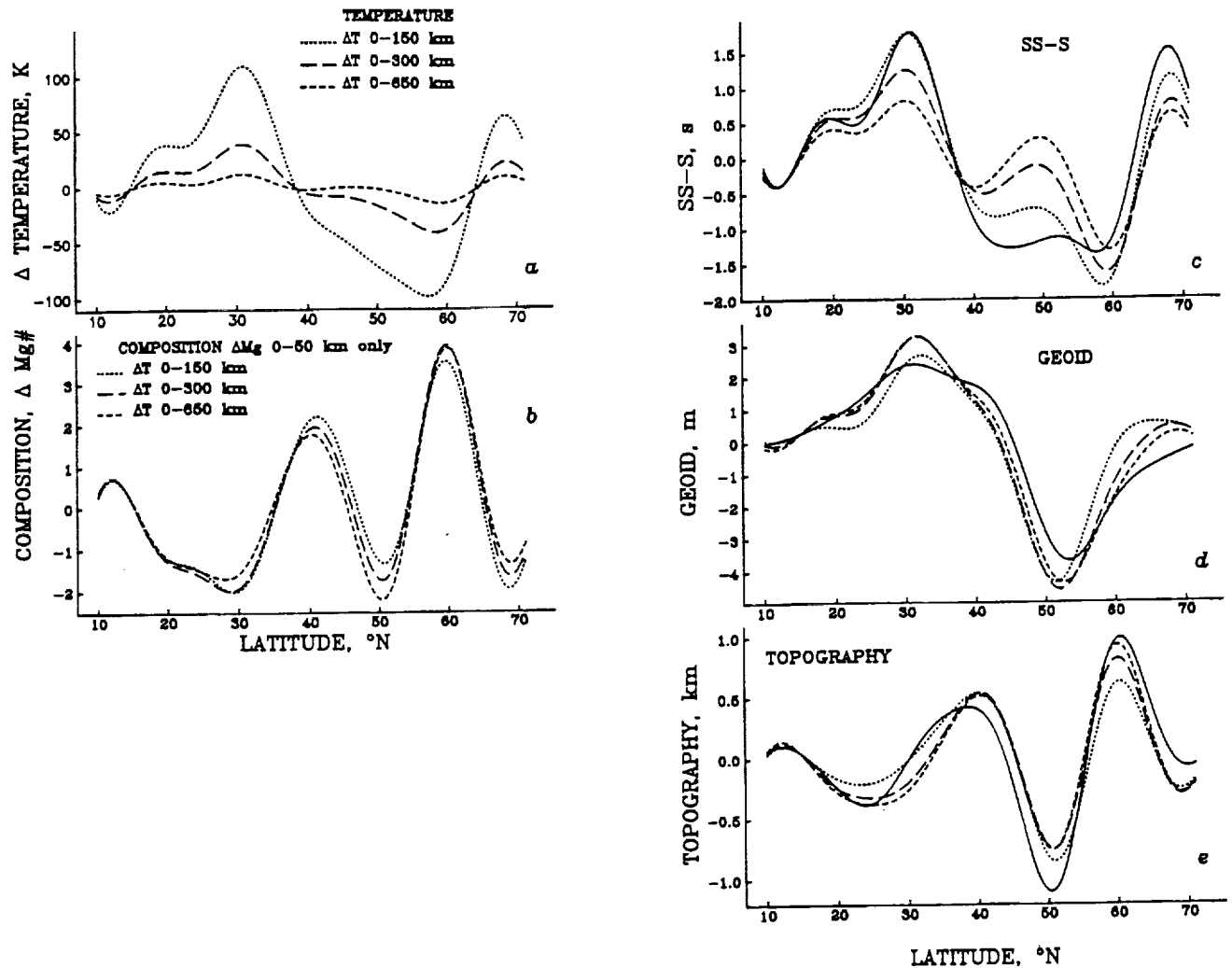


Fig. 19. Same as Figure 17 but compositional variations are constrained to be from 0–50 km depth only.

time, geoid, and bathymetry, we have more equations than unknowns, and the inversion is overdetermined. However, the travel times are perfectly determined in this case because of the nonuniqueness inherent with geoid and bathymetry. We have performed undamped inversions with various weightings on the geoid, bathymetry, and travel time data, and in all cases the travel times remain perfectly fit.

The results for the joint inversion for temperature and composition are summarized in Table 2 and Figures 17 and 18. The geoid residuals are well-modeled in all cases. The topography is best fit for the case with a low viscosity zone. Resolution of the depth interval of the most important lateral variations is rather poor. The topography is fit marginally better for the case where temperature and compositional anomalies are constrained to be shallower than 300 km. For the constant viscosity mantle, the temperature variations range from 210 K, if constrained to 0–150 km depth, to 55K if over 0–650 km depth; variations in Mg # range from 1.5% if over 0–150 km depth to 0.4% for 0–650 km depth. For the case with an upper mantle low viscosity zone, the temperature variations are similar to those in the constant viscosity

case, but the variations in Mg # are larger, from over 2% for 0–150 km depth to nearly 1% for 0–650 km depth.

We have also performed joint inversion for temperature and composition with Mg # variations constrained to be in the upper 50 km of the lithosphere so as to mimic compositional variations due solely to variable melt extraction at the ridge. Temperature perturbations were allowed to remain within the depth ranges adopted earlier. The results for these inversions are summarized in Table 2 and Figures 19 and 20. The variance reduction was similar for the constant viscosity case and for the model with a low-viscosity zone. In general, the geoid is fit very well, the predicted amplitudes are a bit low for travel time residuals, and the topography fit is slightly out of phase. For the constant viscosity mantle, the range in temperature is 210 K over 0–150 km depth and 25 K over 0–650 km, while Mg # variations constrained to be confined to 0–50 km depth were over 5%. For the case with a low-viscosity zone, the temperature variations were not dramatically different from those in the constant viscosity case, and variations in Mg # were about 4.5%. The inversion solution shows high temperatures near 30°N and low tem-

LOW VISCOSITY ZONE

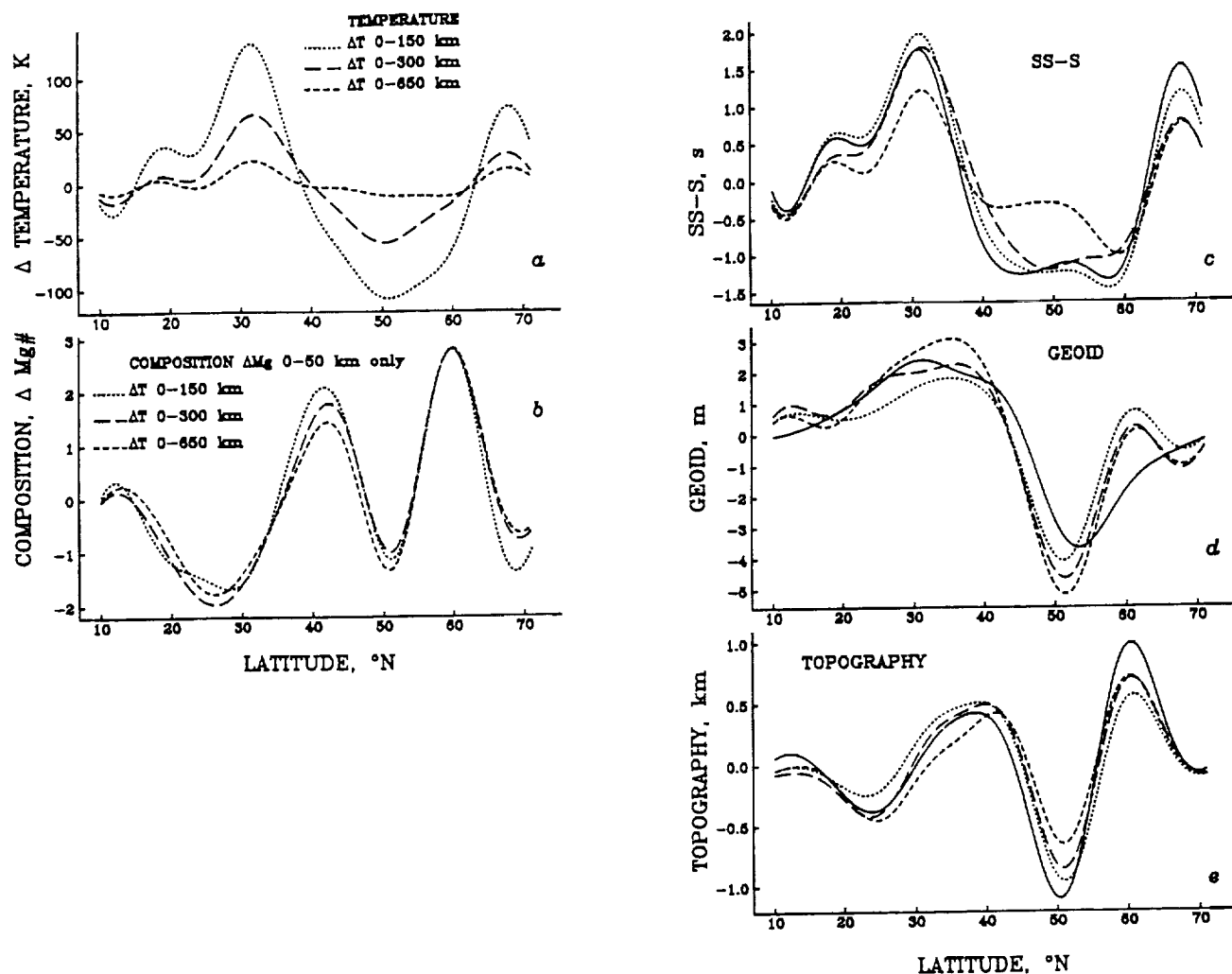


Fig. 20. Same as Figure 18 but compositional variations are constrained to be from 0–50 km depth only.

peratures in the region from 50° to 60°N. Iceland also appears to be underlain by high-temperature mantle. Going from south to north along the ridge, compositional variations indicate low Mg # in the vicinity of 20°–30°N, high Mg # in the Azores region (40°N), low values near 50°N, and high values near 60°N.

DISCUSSION

The temperature and compositional variations in Figures 13–20 are broadly consistent with observed travel time, geoid, and bathymetry anomalies in the North Atlantic region. Temperature variations alone can account for most of the observed anomalies. In contrast, compositional variations alone cannot match all anomalies simultaneously. We infer that a component of the observed anomalies is due to long-wavelength variations in upper mantle temperature. Joint inversions for temperature and composition provide better fits than single-variable models but at the expense of introducing additional free parameters.

It is difficult to select a “best” model from the suite of inversions presented. The variance reductions and χ^2_ν values

in Table 2 serve as guides, but independent criteria may allow us to reject some of the models, even those with high variance reductions and χ^2_ν values near 1. In particular, those models with large temperature variations (well in excess of 100 K) can be seriously questioned. Lateral temperature variations at upper mantle levels beneath oceanic ridges are thought to be no more than about 300 K globally [Klein and Langmuir, 1987], so a variation in temperature of 230 K (as in the inversion with a low-viscosity zone and a 150-km-thick layer of temperature perturbations) solely within a section of the North Atlantic is probably unreasonably large. Further, as McKenzie [1984] and White and McKenzie [1989] have noted, relatively small increases in mantle temperature above values typical for the mid-ocean ridge are sufficient to cause large increases in melt production. Their models indicate that for fixed bulk composition, an increase of 100 K above normal doubles the amount of melt while a 200 K increase can quadruple it. Such increased melt production should lead to approximately corresponding increases in crustal thickness. Variations in oceanic crustal thickness away from fracture zones, how-

ever, are generally thought to be small, with thicknesses typically 6–7 km and ranging from 4.5 to 8.5 km [Spudich and Orcutt, 1980; White, 1984; Purdy and Detrick, 1986]. In the joint inversion for temperature and composition, temperature variations if confined to 150 km depth are excessive (over 200 K) and if the variations extend over 0–650 km the fit to topography is poor, especially for the constant-viscosity mantle. On the basis of these results we prefer the models with temperature variations occurring over 0–300 km depth. For the constant viscosity mantle, the temperature variation is 110 K, and the variation in Mg # is 0.75%. For the case with an upper mantle low-viscosity zone, the predicted temperature variation is 125 K, and the variation in Mg # is 1.1%. The total variance reduction is greater in the model with a low-viscosity zone.

Even a temperature variation of about 100 K is high for a mantle of constant composition, since we do not observe increased crustal thickness in regions that our models indicate have high temperatures. The assumption of approximately constant upper mantle composition warrants discussion. In particular, lateral variation in trace amounts of mantle volatiles may have a large effect on seismic velocity at a given temperature. The presence of even a slight amount of water, for instance, is sufficient to cause a significant decrease in the initial melting temperature of peridotite [Wyllie, 1971]. Estimates of volatile contents and their lateral variations in the North Atlantic region have been made from measurements of abundances of halogens, SiO_2 , K_2O , and H_2O in basalts and from the volumes of vesicles in basalts [Schilling *et al.*, 1980, 1983; Schilling, 1986; Michael, 1988]. These studies indicate that Cl, Br, F, and H_2O contents increase toward the Azores and Iceland and that H_2O is 2–3 times more abundant in Mid-Atlantic Ridge basalts erupted over the Azores platform than at adjacent normal ridge segments. The effect of volatiles on density and shear wave velocity will be slight at subsolidus temperatures but can be major over the melting interval [Goetze, 1977]. The presence of melt will act to decrease significantly the seismic velocity [Duschenes and Solomon, 1977] and, to a lesser extent, lower the density of the mantle. To the extent that seismic velocity depends on proximity of the temperature to the solidus temperature [Sato *et al.*, 1988, 1989], volatile content can trade off with temperature in its effect on velocity at subsolidus conditions. Thus, variation in volatile content could lessen the variations in melt production implied by the inversion solutions.

Even without significant variations in volatile content, it is clearly an oversimplification to parameterize mantle composition in terms of only a single quantity. Further, we have assumed that the partial derivatives of bulk density and seismic velocity with respect to Mg # that are those for olivine [Akimoto, 1972]. The work of Jordan [1979] indicates that these derivatives remain nearly constant for many different mantle compositions (i.e., pyrolite-type compositions with various amounts of olivine, orthopyroxene, clinopyroxene, spinel, and garnet), so the latter assumption is sound. However, at any given Mg #, orthopyroxene and clinopyroxene have lower velocities and are less dense than olivine, while garnet and spinel are seismically faster and denser than olivine [Jordan, 1979], so an increase in the weight percent of orthopyroxene and clinopyroxene or a decrease in the weight percent of garnet and spinel with respect to olivine in the mantle could counteract some of the

temperature variations obtained under the assumption of effectively uniform mineralogy. Several studies [Wood, 1979; Jaques and Green, 1980; Dick *et al.*, 1984] have suggested that compositional variations in the mantle are plausible. Indeed a number of workers [e.g., Davies, 1984; Allègre *et al.*, 1984] favor dynamic models for the mantle in which dispersed heterogeneities of various sizes and shapes are passively embedded in a continually mixed, convecting mantle. Variations in modal fractions of olivine, orthopyroxene, and clinopyroxene in peridotites recovered along the Mid-Atlantic Ridge have been reported in several studies [Dick *et al.*, 1984; Michael and Bonatti, 1985]. These variations are typically attributed to different degrees of melt extraction but could also be partially due to intrinsic upper mantle heterogeneity. For example, the relative fractions of olivine, clinopyroxene, and orthopyroxene indicated by Michael and Bonatti [1985] at 26°N and 30°N, if extended to depth, could counteract a portion of the temperature differences indicated by the inversion solutions for these regions.

Chemical analysis of dredged peridotites in the north Atlantic indicate a range of about 2.5% variation in Mg # [Michael and Bonatti, 1985]. This value is intermediate between what we find for models with compositional variations constrained to be shallow (4.5–6% variation) and those models with compositional variations in the same depth ranges as the thermal variations (1–2%). This suggests that compositional variations may be concentrated slightly shallower than the temperature variations. Michael and Bonatti [1985] present an along-axis profile of Mg # variations from dredged peridotites which can be compared with our calculated profile. The main feature in their profile is a zone of high values of Mg # in the Azores region, from 34° to 45°N, relative to the rest of the ridge, consistent with our modelling results. Their data sampling is too sparse to delineate other long-wavelength features. Their average value for 26°N also has a high Mg # relative to adjacent data. This is consistent with our observation of early SS-S travel times and low geoid in this region. This anomaly is of too short a wavelength (<1000 km), however, to resolve in our inversions. We should note that such comparisons merit caution, as small-scale features, such as those due to ridge segmentation, can produce large differences in composition between peridotites over scales of tens of kilometers. In addition, dredged peridotites are mostly from fracture zone environments, which may not be representative of typical ridge mantle [Dick, 1989].

On the SS-S residual profile the Iceland region appears as a local maximum (late SS) but the Azores hotspot does not show a distinct seismic signal. The inversion results for these two regions are also markedly different. The results of the joint inversion for temperature and composition predict a high Mg # in the Azores region while indicated temperatures are not anomalously high. At Iceland, in contrast, high temperatures dominate. Work by Schilling [1986] and Bonatti [1990] outlines the differences in geochemical signatures between the Azores and Iceland hotspots. These workers suggest that Iceland is a "traditional" plume hotspot, with a predominantly thermal origin, but that the Azores might be more aptly named a "wet spot" because of the presence of excess hydrous phases and the lack of a thermal anomaly. Langmuir and Hanson [1980] noted low Fe contents for basalts from the Azores region and suggested that, in contrast to Iceland, the Azores overlie a mantle that is depleted

in basaltic constituents and has been modified by a volatile-rich component. *Bonatti* [1990] suggests that because the Azores hotspot is rich in volatiles, enhanced melt production could occur with little or no increase in temperature. The high Mg # indicated in our inversions allows the region to be seismically fast (as we observe) but of low density (as geoid and bathymetry require). The results are consistent with the hypothesis that the Azores hotspot is not associated with a significant plumelike thermal anomaly. Inversion of surface wave dispersion data can potentially provide further tests of these ideas, but studies to date have yielded apparently conflicting results. Results of several such investigations [*Nakanishi and Anderson*, 1984; *Tanimoto*, 1990; *Zhang and Tanimoto*, 1990, 1991] suggest that the Azores region is seismically slow at depths less than 300 km, but a study utilizing 50- to 200-s-period Rayleigh waves by *Mocquet et al.* [1989] does not. These differences may be partially attributable to the differences in wave periods employed and mode of analysis from study to study. It may be possible that what appear to be low velocities at the Azores are a result of horizontal smoothing of the low velocities along the ridge and have little to do with the actual structure in the Azores region. Few of these long-period surface wave studies resolve a distinctive anomaly at Iceland. Clearly, more work is needed to resolve the upper mantle velocity structure of hotspot regions.

Zhang and Tanimoto [1991] have constructed a profile of Love wave phase velocity variation along the Mid-Atlantic Ridge at a period of 100 s. Their profile has many features in common with our along-axis profile of SS-S differential travel time, but we also note several differences. In both profiles the region from 10° to 40°N is "slow" relative to the region 40°–70°N. The ridge section from 45° to 55°N is relatively "fast" in both profiles, with velocities becoming gradually lower northward to the Iceland platform and gradually higher again north of Iceland (65°–75°N). The most notable difference is at 40°N, in the vicinity near the Azores hotspot. The model of *Zhang and Tanimoto* [1991] has low velocities (–0.8% less than the average Love wave phase velocity), while our SS-S travel time residuals indicate no distinct anomaly in this region. This discrepancy could be caused by a number of different factors. The surface waves and body waves both average over a portion of the upper mantle, but each does so in a different manner. The 100-s surface waves have kernels which peak at shallow depth (0–100 km) and have decreased sensitivity to depths as great as about 400 km. The SS waves integrate anomalies through the entire upper mantle, with equal resolving power at all depths. The lateral averaging of surface wave and body wave data are also quite different. If a mantle plume underlying a hot spot has a shallow, extended "head" of anomalously hot mantle material [e.g., *White and McKenzie*, 1989], then a surface wave passing through the plume center may display a greater velocity anomaly than a body wave sampling the plume at nearly vertical incidence. By constructing a profile from data with bounce points distributed in age from 0 to 100 Ma, we perform lateral averaging which may further smooth out any hotspot signal. However, a map view of the individual travel time residuals in the immediate vicinity of the Azores (Figure 6) does not show any evidence for a significant anomaly. The Azores region is not anomalously slow in the Love wave phase velocity data of *Zhang and Tanimoto* [1991] at periods of 150 s and greater, indicating that the

source of the anomaly in the 100-s phase velocity most likely arises from the shallow mantle.

Bonatti [1990] has constructed profiles of the equilibrium temperature of dredged peridotites along the Mid-Atlantic Ridge axis from 0 to 60°N by means of two different geothermometers [*Wells*, 1977; *Lindsley*, 1983]. Comparison of these profiles with the along-axis temperature variations obtained from our inversions reveals a number of qualitative correlations as well as a few discrepancies. The range of temperature variations in the profile based on the *Lindsley* [1983] geothermometer is about 150 K, neglecting high values termed "anomalous." When the high values are included the range increases to 400 K. The profile utilizing the *Wells* [1977] geothermometer has a range of 100 K neglecting the anomalous values and 350 K including them. The highest temperatures in our inversions are near 30°N (Figures 17 and 18), a region showing a slight peak in *Bonatti's* temperature profile estimated according to *Lindsley* [1983] and a very weak rise in the profile utilizing the *Wells* [1977] geothermometer. There is a small dip in temperature at 26°N (a region which we find to be seismically fast) in the *Lindsley* [1983] and *Wells* [1977] profiles, but the difference may not be significant considering the errors. *Bergman and Solomon* [1989] also found the upper mantle near 26°N to be seismically fast from an analysis of teleseismic *P* wave travel time residuals from earthquakes in this region recorded by a local ocean bottom seismic network. The lowest temperatures on the profiles of *Bonatti* [1990] are at 43°N. Temperatures from our inversion solutions are also low in this region, although the *Bonatti* [1990] profiles indicate an increase in temperature proceeding north from 43°N to 53°N, whereas our results favor continued low temperatures. Part of the difference between our results and the geochemical studies may be attributed to the fact that the depth sampled by basalts and peridotites is likely to be shallower than the layer thicknesses of most of our models. Assuming that the 6-km-thick oceanic crust was formed by 9–22% partial melting of the mantle [*Klein and Langmuir*, 1987], then the volume of residual peridotite will extend from the base of the crust to somewhere between 30 and 70 km depth. The amount of depletion will vary with depth if we assume a fractional melting model. Our models with compositional variations confined to depths less than 50 km are most representative of shallow fractionation and differentiation.

Alternate petrological measures of upper mantle temperature may be obtained from the major element chemistry of mantle-derived basalts. *Klein and Langmuir* [1987, 1989] suggest that the quantity $Fe_{8.0}$ (basalt FeO content corrected to 8.0 wt % MgO) is related to mantle temperature in the source region, with low $Fe_{8.0}$ indicating a relatively cool mantle and a narrow depth interval of melt generation and high $Fe_{8.0}$ indicating a hotter mantle and a greater depth interval of melt generation. A comparison of the temperature variation obtained in our inversions with an along-axis profile of $Fe_{8.0}$ [*Klein and Langmuir*, 1989] shows several striking correlations, particularly peaks in both quantities near 30°N and near Iceland.

Several improvements in future studies of the type presented here may be envisioned. Our models thus far have been limited to simply parameterized one-dimensional variations in temperature and composition within a single layer. It is likely that these lateral variations are not constant

within a given layer and that there are two-dimensional lateral variations independent of lithospheric aging. The techniques outlined in this paper can be generalized to a multilayer system and to two-dimensional wavenumber (see equation (8)), but we do not feel that the resolution of our data can justify more complicated models at this time. Kernels for seismic surface waves are strongly peaked in the upper mantle, and such data would provide a useful constraint in future models. The inclusion of surface wave data would help to distinguish between lithospheric and asthenospheric effects and may allow for two or more independently resolved layers. Extension of the modelling to three dimensions would permit an assessment of the degree to which mantle anomalies beneath the ridge extend off axis. Implicit in our age correction is the assumption that the anomalous properties of the ridge mantle are steady state on a time scale of 100 Ma. Recent seafloor surveys and theoretical studies [e.g., *Pockalny et al.*, 1988; *Scott and Stevenson*, 1989] bring this assumption into question and suggest that at least on short time scales (<1 m.y.) and at slow spreading rates (as in the Atlantic) intermittent periods of melting and crustal formation may be separated by periods with little or no melt production. These temporal variations are likely to be averaged out, however, over the typical horizontal wavelength (>100 km) of a long-period SS wave.

Another limitation of our models is that they depend on the assumed values of several physical constants. It is straightforward, however, to estimate the effect of choosing different values. The viscosity structures that we employ are also quite simple but have been chosen to represent two models widely invoked in other studies, a constant or nearly constant viscosity mantle [e.g., *Peltier*, 1989] and a mantle with a thin low-viscosity layer [e.g., *Craig and McKenzie*, 1986; *Robinson et al.*, 1987]. The viscosity structure of the Earth may be temperature and pressure dependent or vary laterally, but we have not considered viscosity structures of this type [e.g., *Revenaugh and Parsons*, 1987]. Much work remains to be done to determine ways to incorporate lateral variations in viscosity into quantitative treatments of these problems. We have not modelled the effects of partial melting which could accompany the temperature variations that we predict. The effect of retained melt on the physical properties of the mantle depends critically on the melt fraction and geometry, characteristics presently poorly known. *Sato et al.* [1988, 1989] downplay the importance of partial melt and suggest that most mantle seismic velocity anomalies can be explained by temperature variations at subsolidus conditions. The combined analysis of both shear and compressional differential travel times also suggest that significant partial melting is not required to explain the travel time residuals in the North Atlantic region [*Woodward and Masters*, 1991a].

CONCLUSIONS

We have measured nearly 500 SS-S differential travel times for paths in the North Atlantic region. The SS-S travel time residual decreases linearly with square root of age, in general agreement with the plate cooling model, to an age of 80–100 Ma [*Parsons and Sclater*, 1977]. Azimuthal anisotropy is not clearly resolved; in particular, the azimuthal patterns of our data are not consistent with the preferred upper mantle anisotropy model of *Kuo et al.* [1987] for the

North Atlantic. If azimuthal anisotropy is present in the North Atlantic, it is not uniform over the entire region. An along-axis profile of age-corrected travel time residuals displays significant variations at wavelengths of 1000–7000 km. The largest of these variations are robust with respect to selective removal of portions of the data.

We have formulated a joint inversion of travel time residuals and geoid and bathymetric anomalies for lateral variation in upper mantle temperature and composition. On the basis of variance reduction, inversion for temperature favors the presence of an upper mantle low-viscosity zone and temperature anomalies concentrated at depths less than 300 km. We are unable to match travel time residuals simultaneously with geoid and bathymetry solely with lateral variations in bulk composition (Mg #). Joint inversions for temperature and composition provide good fits to both travel time and geoid regardless of viscosity structure or layer depth and thickness, but the best fits to bathymetry come from models with a low-viscosity zone and thermal or compositional variations confined to shallow depth. The Mg # variations predicted in the joint inversion for temperature and composition are comparable to those found by *Michael and Bonatti* [1985] in a study of dredged peridotites along the Mid-Atlantic Ridge and may be related to variations in melt production along the ridge.

The preferred inversion solutions have variations in upper mantle temperature along the Mid-Atlantic Ridge of about 100 K. For a constant bulk composition, such a temperature variation would produce about a 7-km variation in crustal thickness [*White and McKenzie*, 1989], larger than is generally observed [*Spudich and Orcutt*, 1980; *White*, 1984; *Purdy and Detrick*, 1986]. Introducing compositional variations as well as temperature variations in the inversions does not change the range of temperature appreciably. The presence of volatiles in the mantle can have a strong effect on temperatures required for melting, and variations in volatile content along the ridge may reduce the large variation in melt production implied by the lateral temperature variations indicated in our models.

APPENDIX A: ESTIMATION OF ERRORS FOR SS-S DIFFERENTIAL TRAVEL TIMES

It is important to quantify the uncertainties in the differential travel time measurements. After cross-correlation, the "quality" of each individual SS-S measurement is rated and a grade is assigned. The cross-correlation coefficient, which describes the degree of fit between the synthetic and real SS phases, is used as an objective aid in the assignment of quality. However, our final assignment of quality is largely subjective and based upon visual inspection of the "synthetic" SS, real SS, and cross correlogram, taking into account the sharpness of the arrivals and their alignment, the clarity of the seismogram, and the appearance of a single clear peak in the cross-correlation function. An "A" quality grade indicates an excellent fit, "B" quality indicates good phase alignment but only a fair fit, and a "C" quality grade indicates a poor fit or some ambiguity as to phase alignment. In addition to A, B, and C grades, there were data that were rejected due to poor signal to noise ratio for either the S or SS phases.

Assuming that the uncertainty in an individual measurement comes from a combination of measurement error,

unmodeled lower mantle structure, and epicentral error, we write, for example, for the measurement variance of an "A" quality datum:

$$\sigma_A^2 = \sigma_{Am}^2 + \sigma_{lm}^2 + \sigma_{epi}^2 \quad (A1)$$

where σ_A is the total uncertainty, σ_{Am} is the measurement error, σ_{lm} is the uncertainty due to unmodeled lower mantle structure, and σ_{epi} is the epicentral error. We assume that σ_{lm} and σ_{epi} are the same for A, B, and C quality measurements, but the measurement error is obviously a strong function of data quality.

Effect of Epicentral Error

In general, epicentral errors affect the travel times only slightly. The events used in this study were well recorded by a large number of stations over a wide range of azimuths, and typical epicentral mislocations are probably less than 10 km (which would yield a differential travel time error of 0.35 s at 75° distance). The travel times are even less sensitive to errors in focal depth; an error in depth of 25 km contributes only about 0.3 s to the SS-S residual. Using the rule of thumb that one standard deviation is about one half of the estimated extremes, we adopt $\sigma_{epi} = 0.75$ s as a conservative estimate of epicentral error.

Effect of Unmodelled Lower Mantle Heterogeneity

We estimate the likely magnitude of lateral variations in the shear wave velocity of the lower mantle from models of lower mantle heterogeneity in *P* wave velocity (such as model L02.56 of Dziewonski [1984]). The average variation in travel times of direct *P* waves bottoming in the lower mantle is in the range ± 0.5 s. Global tomographic studies by Dziewonski and Woodhouse [1987] indicate that the scaling ratio $(\delta V_s/V_s)/(\delta V_p/V_p) \approx 2$ in the lower mantle. Such a scaling is also suggested by comparison of lower mantle *P* wave models with the recent lower mantle *S* model of Tanimoto [1990]. Assuming such an *S* to *P* velocity anomaly scaling, the resulting variation in *S* wave arrival time contributed by the lower mantle would likely be about ± 1.5 s, a fraction of the observed range in SS-S residual. While the major features of lower mantle model L02.56 [Dziewonski, 1984] and the lower mantle portions of Tanimoto's [1990] model are for the most part similar, enough differences exist that the application of a lower mantle "correction" to our data might add more uncertainty than it removes. Further, absolute *S* wave travel times do not show enough variance for us to suspect large lower mantle effects [e.g., Randall, 1971; Girardin and Poupinet, 1974; Hart and Butler, 1978; Uhrhammer, 1978, 1979], and the work of Gudmundson *et al.* [1990] indicates that most of the variance from the ISC tables is attributable to the shallow mantle, i.e., most of the Earth's heterogeneity is in the upper mantle and the lower mantle is fairly homogeneous. On the basis of the above information, we set $\sigma_{lm} = 0.5$ s for our study. We note, however, that knowledge of global-scale structure in the lower mantle is still incomplete. Some recent studies [Woodward and Masters, 1991a, b] suggest that a larger value of σ_{lm} is warranted. However, the fact that our study involves only a limited geographic area may confine the lower mantle variation to only a fraction of the full global range.

Measurement Error

As an objective means to obtain error estimates, we examine the scatter in A, B, and C quality picks in a small region. We measured the root mean square (rms) difference between travel time residuals of the same grade (A, B, or C) with bounce points separated by less than 80 km and with differences in path azimuth at the bounce point of less than 10°. An 80-km distance is less than the horizontal wavelength of SS (which is about 180 km at 25-s period) so we do not expect much contribution to the rms difference from actual lateral variations in structure. The rms difference for the 16 A quality residual pairs which were within 80 km of each other was 1.15 s. For B quality picks, an rms difference of 2.08 s was measured using 20 residual pairs, and for C quality picks, 44 residual pairs yielded an rms difference of 2.96 s.

We interpret these estimates of the rms differences as representing the average overall errors in the A, B, and C grade measurements. (Unmodelled lower mantle structure should be nearly identical for data with bounce points within 80 km and at similar azimuths.) Under this interpretation we can write, for A quality residuals

$$\sigma_{Arms}^2 = \sigma_{Am}^2 + \sigma_{epi}^2 \quad (A2)$$

Substituting values of σ_{Arms} and σ_{epi} into (A2) yields $\sigma_{Am} = 0.87$ s. Similarly, for B and C quality measurements, we find $\sigma_{Bm} = 1.94$ s and $\sigma_{Cm} = 2.86$ s. From (A1), the total uncertainty for A, B, and C quality is, respectively, $\sigma_A = 1.25$ s, $\sigma_B = 2.14$ s, and $\sigma_C = 3.00$ s.

In the weighted regression experiments the A, B, and C quality measurements are weighted inversely by their measurement variance.

APPENDIX B: ERRORS IN THE ALONG-AXIS PROFILES AND CONSTRUCTION OF DATA COVARIANCE MATRIX

Errors in Bathymetry, Geoid, and Travel Time Profiles

Uncertainties in the along-axis profiles of geoid, bathymetry, and travel times are important information in the inversion. The gridded bathymetric data [U.S. Naval Oceanographic Office, 1985] include corrections for the deviation of water column acoustic velocity from the assumed value of 1500 m s⁻¹. The geoid data, provided in the form of a 0.25° × 0.25° grid [Marsh *et al.*, 1986], include corrections for orbit errors, instrument and atmospheric propagation effects, and solid Earth and ocean tides.

We have averaged the bathymetry and geoid height values within a 1° × 1° box centered at each SS bounce point. The averaging yields a representative value for a region over approximately one horizontal wavelength of the SS wave and acts to smooth out short-wavelength variations. Both bathymetry and geoid are corrected for subsidence with seafloor age, using the plate cooling model [Parsons and Sclater, 1977; Parsons and Richter, 1980]. Error introduced into depth and geoid anomalies by isochron mislocation is difficult to estimate precisely, but for an error in age of 2 m.y., depth and geoid errors at 80 Ma would be about 30 m and 0.2 m, respectively, while at 2 Ma, an error in age of 2 m.y. would have a much larger effect, giving depth and geoid errors of 350 and 0.3 m. The magnitude of this error

highlights the importance of accurate age determination, especially at young ages.

The presence of oceanic sediments is another source of error. In the Atlantic Ocean, the sediment thickness increases regularly from less than 100 m along the Mid-Atlantic Ridge toward continental margins where it can exceed 1 km [Ewing *et al.*, 1973; Tucholke, 1986]. A 1-km sediment thickness leads to corrections to residual depth and geoid of about 500 and 0.3 m, respectively [Cazenave *et al.*, 1988; Sheehan and McNutt, 1989]. On Atlantic lithosphere of 100 Ma age or less the sediment thickness is less than 500 m in most areas. Hence, neglecting the sediment loading correction should not be crucial in this region.

The along-axis profile of SS-S residual (Figure 10) is a

$$R_{dd} = \begin{pmatrix} \sigma_h(k_1)^2 & 0 & 0 & 0 & 0 & 0 & 0 & 0 & 0 \\ 0 & \dots & 0 & 0 & 0 & 0 & 0 & 0 & 0 \\ 0 & 0 & \sigma_h(k_n)^2 & 0 & 0 & 0 & 0 & 0 & 0 \\ 0 & 0 & 0 & \sigma_N(k_1)^2 & 0 & 0 & 0 & 0 & 0 \\ 0 & 0 & 0 & 0 & \dots & 0 & 0 & 0 & 0 \\ 0 & 0 & 0 & 0 & 0 & \sigma_N(k_n)^2 & 0 & 0 & 0 \\ 0 & 0 & 0 & 0 & 0 & 0 & \sigma_t(k_1)^2 & 0 & 0 \\ 0 & 0 & 0 & 0 & 0 & 0 & 0 & \dots & 0 \\ 0 & 0 & 0 & 0 & 0 & 0 & 0 & 0 & \sigma_t(k_n)^2 \end{pmatrix}$$

weighted moving average of 10 adjacent data points grouped by latitude, using the weights discussed in Appendix A. The same weights and moving average are applied to geoid and bathymetry values at a given SS bounce point, even though bathymetry and geoid data sets are each presumed to be of uniform quality, in order that these profiles will be consistent with the SS-S residuals. The standard error of the mean values for SS-S residual range from 0.2 to 1.6 s. For bathymetry the range of standard deviations from the mean value is from 24 to 370 m and for geoid is 0.08 to 1.0 m. The largest variances in the bathymetry and geoid data come from the Iceland region (north of 60°N), and may be due to the more complicated tectonics of this region [White, 1988].

Before Fourier transforming, the along-axis profiles must be interpolated to a constant spacing. We use a simple linear interpolation scheme to estimate values at 0.5° spacing. We estimate that the typical error in the interpolated data is comparable to that in the along-axis moving averages, which for bathymetry is of the order of 125 m, for geoid 0.4 m, and for travel time 1 s.

Effect of Crustal Thickness Variations

Our poor fit to topography in the inversion experiments can be at least partially attributed to unmodelled effects such as crustal thickness differences. Variations in oceanic crustal thickness about the typical value of 6–7 km [Spudich and Orcutt, 1980; White, 1984; Purdy and Detrick, 1986] are generally thought to be small at horizontal scales of 100 km and greater. However, the crust beneath the Azores plateau is estimated to be between 8 and 9 km thick [Searle, 1976; Whitmarsh *et al.*, 1982] and that beneath Iceland is at least

8–14 km thick [Bjornsson, 1983]. By simple isostatic mass balance, the depth anomaly due to excess crustal thickness in the Azores region would be about 400 m, and at Iceland, 200 m to 1.6 km. In general simple variations in crustal thickness are insufficient to produce a significant SS-S residual. For crustal and mantle S wave velocities of 3.5 and 4.4 km s⁻¹, a 2-km variation in crustal thickness would contribute less than 0.2 s to an SS-S differential travel time corrected for differences in bathymetry. However, at Iceland, where the crust is estimated to be as much as 14 km thick, the additional SS-S travel time could be up to 0.8 s.

Data Covariance Matrix

The data covariance matrix R_{dd} is of the form

where σ_h^2 , σ_N^2 , and σ_t^2 are the nominal variances of the bathymetry, geoid, and travel time data, respectively. We may choose to construct the data covariance matrix not to reflect the true variance of the data but rather to allow weighting between the different data sets. In this way, the data covariance matrix can be altered to test the relative contributions of different data sets to the inversion results.

In all of our inversions, the covariance matrix is constructed to weight the three data sets approximately equally. For example, examination of Figure 10 indicates that at 3000-km wavelength the amplitude of the geoid signal is approximately 4 m, bathymetry 1 km, and travel time 2 s. Thus if a value of 1 m is chosen for σ_N , then a value of 0.5 s for σ_t and 0.25 km for σ_h should yield approximately equal weighting of data sets. The corresponding $1/\sigma^2$ values are then 1 for geoid, 4 for travel time, and 16 for bathymetry.

Acknowledgments. We thank Marcia McNutt for suggesting the inverse problem, and Anne Judge for providing codes for computing geoid and topography kernels. Bob Woodward and Justin Revenaugh provided advice and subroutines for measuring travel times. We thank Fred Frey, Tim Grove, Brad Hager, Tom Jordan, Ban-Yuan Kuo, Charles Langmuir, Ted Madden, Justin Revenaugh, Bob Woodward and Yu-Shen Zhang for helpful comments. We thank the two reviewers and the associate editor for thorough, constructive reviews which helped clarify our presentation. We thank John Woodhouse and Adam Dziewonski for allowing us access to the digital data archives at Harvard University and Lind Gee for setting up the data retrieval software at MIT. This research was supported by the National Science Foundation under grant EAR-9004750 and the National Aeronautics and Space Administration under grant NAG 5-814.

REFERENCES

- Akimoto, S.-I., The system MgO-FeO-SiO_2 at high pressures and temperatures—Phase equilibria and elastic properties, *Tectonophysics*, 13, 161–187, 1972.
- Allègre, C. J., B. Hamelin, and B. Dupré, Statistical analysis of isotopic ratios in MORB: The mantle blob cluster model and the convective regime of the mantle, *Earth Planet. Sci. Lett.*, 71, 71–84, 1984.
- Anderson, O. L., E. Schreiber, R. C. Lieberman, and N. Soga, Some elastic constant data on minerals relevant to geophysics, *Rev. Geophys.*, 6, 491–524, 1968.
- Anderson, R. N., D. McKenzie, and J. G. Sclater, Gravity, bathymetry, and convection in the Earth, *Earth Planet. Sci. Lett.*, 18, 391–407, 1973.
- Backus, G. E., Possible forms of seismic anisotropy of the upper mantle under oceans, *J. Geophys. Res.*, 70, 3429–3439, 1965.
- Bergman, E. A., and S. C. Solomon, P wave travel times for Mid-Atlantic Ridge earthquakes and evidence for mantle heterogeneity (abstract), *Eos Trans. AGU*, 70, 1227, 1989.
- Björnsson, S., Crust and upper mantle beneath Iceland, in *Structure and Development of the Greenland-Scotland Ridge*, edited by M. H. P. Bott, S. Saxov, M. Talwani, and J. Thiede, *NATO Conf. Ser.*, 4, 8, 31–61, 1983.
- Bonatti, E., Not so hot "hot spots" in the oceanic mantle, *Science*, 250, 107–111, 1990.
- Boyd, F. R., and R. H. McCallister, Densities of fertile and sterile garnet peridotites, *Geophys. Res. Lett.*, 3, 509–512, 1976.
- Buck, W. R., and E. M. Parmentier, Convection beneath young oceanic lithosphere: Implications for thermal structure and gravity, *J. Geophys. Res.*, 91, 1961–1974, 1986.
- Butler, R., Shear-wave travel times from SS, *Bull. Seismol. Soc. Am.*, 69, 1715–1732, 1979.
- Cazenave, A., K. Dominh, M. Rabinowicz, and G. Ceuleneer, Geoid and depth anomalies over ocean swells and troughs: Evidence of an increasing trend of the geoid to depth ratio with age of plate, *J. Geophys. Res.*, 93, 8064–8077, 1988.
- Choy, G. L., and P. G. Richards, Pulse distortion and Hilbert transformation in multiply reflected and refracted body waves, *Bull. Seismol. Soc. Am.*, 65, 55–70, 1975.
- Craig, C. H., and D. McKenzie, The existence of a thin low viscosity layer beneath the lithosphere, *Earth Planet. Sci. Lett.*, 78, 420–426, 1986.
- Crampin, S., A review of the effects of anisotropic layering on the propagation of seismic waves, *Geophys. J. R. Astron. Soc.*, 49, 9–27, 1977.
- Creager, K. C., and T. H. Jordan, Slab penetration into the lower mantle beneath the Mariana and other island arcs of the Northwest Pacific, *J. Geophys. Res.*, 91, 3573–3589, 1986.
- Davies, G. F., Geophysical and isotopic constraints on mantle convection: An interim synthesis, *J. Geophys. Res.*, 89, 6017–6040, 1984.
- DeMets, C., R. G. Gordon, D. F. Argus, and S. Stein, Current plate motions, *Geophys. J. Int.*, 101, 425–478, 1990.
- Dick, H. J. B., Abyssal peridotites, very-slow spreading ridges and ocean ridge magmatism, in *Magmatism in the Ocean Basins*, edited by A. D. Saunders, and M. J. Norry, *Geol. Soc. Spec. Publ. London*, 42, 71–105, 1989.
- Dick, H. J. B., R. L. Fisher, and W. B. Bryan, Mineralogic variability of the uppermost mantle along mid-ocean ridges, *Earth Planet. Sci. Lett.*, 69, 88–106, 1984.
- Duffy, T. S., and D. L. Anderson, Seismic velocities in mantle minerals and the mineralogy of the upper mantle, *J. Geophys. Res.*, 94, 1895–1912, 1989.
- Duschenes, J. D., and S. C. Solomon, Shear wave travel time residuals from oceanic earthquakes and the evolution of oceanic lithosphere, *J. Geophys. Res.*, 82, 1985–2000, 1977.
- Dziewonski, A. M., Mapping the lower mantle: Determination of lateral heterogeneity in P velocity up to degree and order 6, *J. Geophys. Res.*, 89, 5929–5952, 1984.
- Dziewonski, A. M., and D. L. Anderson, Preliminary reference Earth model, *Phys. Earth Planet. Inter.*, 25, 297–356, 1981.
- Dziewonski, A. M., and J. F. Gilbert, The effect of small, aspherical perturbations on travel times and a re-examination of the corrections for ellipticity, *Geophys. J. R. Astron. Soc.*, 44, 7–17, 1976.
- Dziewonski, A. M., and J. H. Woodhouse, An experiment in systematic study of global seismicity: Centroid-moment tensor solutions for 201 moderate and large earthquakes in 1981, *J. Geophys. Res.*, 88, 3247–3271, 1983.
- Dziewonski, A. M., and J. H. Woodhouse, Global images of the Earth's interior, *Science*, 236, 37–48, 1987.
- Dziewonski, A. M., B. H. Hager, and R. J. O'Connell, Large-scale heterogeneities in the lower mantle, *J. Geophys. Res.*, 82, 239–255, 1977.
- Dziewonski, A. M., T.-A. Chou, and J. H. Woodhouse, Determination of earthquake source patterns from waveform data for studies of global and regional seismicity, *J. Geophys. Res.*, 86, 2825–2852, 1981.
- Ewing, M., G. Carpenter, C. Windisch, and J. Ewing, Sediment distribution in the oceans: The Atlantic, *Geol. Soc. Am. Bull.*, 84, 71–88, 1973.
- Fischer, K. M., T. H. Jordan, and K. C. Creager, Seismic constraints on the morphology of deep slabs, *J. Geophys. Res.*, 93, 4773–4783, 1988.
- Gee, L. S., and T. H. Jordan, Generalized seismological data functions I. Theory and observational procedures (abstract), *Eos Trans. AGU*, 70, 1201–1202, 1989.
- Girardin, N., and G. Poupinet, Teleseismic S travel-time delay for Mid-Atlantic Ridge earthquakes, *Phys. Earth Planet. Inter.*, 9, 306–313, 1974.
- Goetze, C., A brief summary of our present day understanding of the effect of volatiles and partial melt on the mechanical properties of the upper mantle, in *High-Pressure Research, Applications in Geophysics*, edited by M. H. Manghnani and S.-I. Akimoto, pp. 3–24, Academic, San Diego, Calif., 1977.
- Grand, S. P., Tomographic inversion for shear velocity beneath the North American plate, *J. Geophys. Res.*, 92, 14,065–14,090, 1987.
- Grand, S. P., Mantle shear structure from 30°S to 90°N and 120°W to 60°E (abstract), *Eos Trans. AGU*, 70, 389, 1989.
- Grand, S. P., and D. V. Helmberger, Upper mantle shear structure beneath the northwest Atlantic Ocean, *J. Geophys. Res.*, 89, 11,465–11,475, 1984.
- Green, D. H., and R. C. Liebermann, Phase equilibria and elastic properties of a pyrolite model for the oceanic upper mantle, *Tectonophysics*, 32, 61–92, 1976.
- Gudmundsson, O., J. H. Davies, and R. W. Clayton, Stochastic analysis of global traveltimes data: Mantle heterogeneity and random errors in the ISC data, *Geophys. J. Int.*, 102, 25–43, 1990.
- Hager, B. H., Subducted slabs and the geoid: Constraints on mantle rheology and flow, *J. Geophys. Res.*, 89, 6003–6015, 1984.
- Hager, B. H., and R. W. Clayton, Constraints on the structure of mantle convection using seismic observations, flow models, and the geoid, in *Mantle Convection*, edited by W. R. Peltier, pp. 657–763, Gordon and Breach, New York, 1989.
- Hager, B. H., and R. J. O'Connell, Kinematic models of large-scale flow in the Earth's mantle, *J. Geophys. Res.*, 84, 1031–1048, 1979.
- Hager, B. H., and R. J. O'Connell, A simple global model of plate dynamics and mantle convection, *J. Geophys. Res.*, 86, 4843–4867, 1981.
- Hager, B. H., and M. A. Richards, Long-wavelength variations in Earth's geoid: Physical models and dynamical implications, *Philos. Trans. R. Soc. London, Ser. A*, 328, 309–327, 1989.
- Hager, B. H., R. W. Clayton, M. A. Richards, R. P. Comer, and A. M. Dziewonski, Lower mantle heterogeneity, dynamic topography and the geoid, *Nature*, 313, 541–545, 1985.
- Hart, R. S., and R. Butler, Shear-wave travel times and amplitudes for two well-constrained earthquakes, *Bull. Seismol. Soc. Am.*, 68, 973–985, 1978.
- Honda, S., and T. Tanimoto, Regional 3-D heterogeneities by waveform inversion—Application to the Atlantic area, *Geophys. J. R. Astron. Soc.*, 91, 737–753, 1987.
- Hong, H. J., D. A. Yuen, and J. Wu, Dynamical effects of a hard garnet layer in the transition zone on geophysical signatures: Geoid anomalies and postglacial rebound, *Phys. Earth Planet. Inter.*, 64, 37–51, 1990.
- Jacques, A. L., and D. H. Green, Anhydrous melting of peridotite at 0–15 kb pressure and the genesis of tholeiitic basalts, *Contrib. Mineral. Petrol.*, 73, 287–310, 1980.
- Johnson, K. T. M., H. J. B. Dick, and N. Shimizu, Melting in the oceanic upper mantle: An ion microprobe study of diopsides in abyssal peridotites, *J. Geophys. Res.*, 95, 2661–2678, 1990.
- Jordan, T. H., Mineralogies, densities, and seismic velocities of garnet lherzolites and their geophysical implication, in *The Mantle*

- Sample: Inclusions in Kimberlites and Other Volcanics*, edited by F. R. Boyd and H. O. A. Meyer, pp. 1-14, AGU, Washington, D. C., 1979.
- Jordan, T. H., and W. S. Lynn, A velocity anomaly in the lower mantle, *J. Geophys. Res.*, 79, 2679-2685, 1974.
- Kent, D. V., and F. M. Gradstein, A Jurassic to recent geochronology, in *The Geology of North America*, vol. M, *The Western North Atlantic Region*, edited by P. R. Vogt and B. E. Tucholke, pp. 45-50, Geological Society of America, Boulder, Colo., 1986.
- Klein, E. M., and C. H. Langmuir, Global correlations of ocean ridge basalt chemistry with axial depth and crustal thickness, *J. Geophys. Res.*, 92, 8089-8115, 1987.
- Klein, E. M., and C. H. Langmuir, Local versus global variations in ocean ridge basalt composition: A reply, *J. Geophys. Res.*, 94, 4241-4252, 1989.
- Klitgord, K. D., and H. Schouten, Plate kinematics of the central Atlantic, in *The Geology of North America*, vol. M, *The Western North Atlantic Region*, edited by P. R. Vogt and B. E. Tucholke, pp. 351-378, Geological Society of America, Boulder, Colo., 1986.
- Kumazawa, M., and O. L. Anderson, Elastic moduli, pressure derivatives, and temperature derivatives of single-crystal olivine and single-crystal forsterite, *J. Geophys. Res.*, 74, 5961-5972, 1969.
- Kuo, B.-Y., D. W. Forsyth, and M. Wyssession, Lateral heterogeneity and azimuthal anisotropy in the North Atlantic determined from SS-S differential travel times, *J. Geophys. Res.*, 92, 6421-6436, 1987.
- Langmuir, C. H., and G. N. Hanson, An evaluation of major element heterogeneity in the mantle sources of basalts, *Philos. Trans. R. Soc. London, Ser. A*, 297, 383-407, 1980.
- Lerch, F. J., S. M. Klosko, R. E. Laubscher, and C. A. Wagner, Gravity model improvement using Geos 3 (GEM 9 and 10), *J. Geophys. Res.*, 84, 3897-3916, 1979.
- Liebermann, R. C. Velocity-density systematics for the olivine and spinel phases of Mg_2SiO_4 - Fe_2SiO_4 , *J. Geophys. Res.*, 75, 4029-4034, 1970.
- Lindsley, D. H., Pyroxene thermometry, *Am. Mineral.*, 68, 477-493, 1983.
- Marsh, J. G., A. C. Brenner, B. D. Beckley, and T. V. Martin, Global mean sea surface based upon the Seasat altimeter data, *J. Geophys. Res.*, 91, 3501-3506, 1986.
- McKenzie, D., Surface deformation, gravity anomalies and convection, *Geophys. J. R. Astron. Soc.*, 48, 211-238, 1977.
- McKenzie, D., The generation and compaction of partially molten rock, *J. Petrol.*, 25, 713-765, 1984.
- McKenzie, D., and C. Bowin, The relationship between bathymetry and gravity in the Atlantic Ocean, *J. Geophys. Res.*, 81, 1903-1915, 1976.
- McKenzie, D., A. Watts, B. Parsons, and M. Roufousse, Planform of mantle convection beneath the Pacific Ocean, *Nature*, 288, 442-446, 1980.
- McNutt, M. K., and A. V. Judge, The superswell and mantle dynamics beneath the South Pacific, *Science*, 248, 969-975, 1990.
- Michael, P. J., The concentration, behavior and storage of H_2O in the suboceanic upper mantle: Implications for mantle metasomatism, *Geochim. Cosmochim. Acta*, 52, 555-566, 1988.
- Michael, P. J., and E. Bonatti, Periodotite composition from the North Atlantic: Regional and tectonic variations and implications for partial melting, *Earth Planet. Sci. Lett.*, 73, 91-104, 1985.
- Mocquet, A., and B. Romanowicz, Three-dimensional structure of the upper mantle beneath the Atlantic Ocean inferred from long-period Rayleigh waves, 2, Inversion, *J. Geophys. Res.*, 95, 6787-6798, 1990.
- Mocquet, A., B. Romanowicz, and J. P. Montagner, Three-dimensional structure of the upper mantle beneath the Atlantic Ocean inferred from long-period Rayleigh waves, 1, Group and phase velocity distributions, *J. Geophys. Res.*, 94, 7449-7468, 1989.
- Montagner, J. P., and T. Tanimoto, Global anisotropy in the upper mantle inferred from the regionalization of phase velocities, *J. Geophys. Res.*, 95, 4797-4819, 1990.
- Nakanishi, I., and D. L. Anderson, Measurements of mantle wave velocities and inversion for lateral heterogeneity and anisotropy, II, Analysis by the single station method, *Geophys. J. R. Astron. Soc.*, 78, 573-617, 1984.
- Nolet, G., and N. J. Vlaar, The NARS project: Probing the Earth's interior with a large seismic antenna, *Terra Cognita*, 2, 17-25, 1982.
- O'Hara, M. J., Is there an Icelandic mantle plume, *Nature*, 253, 708-710, 1975.
- Oxburgh, E. R., and E. M. Parmentier, Compositional and density stratification in oceanic lithosphere—Causes and consequences, *J. Geol. Soc. London*, 133, 343-355, 1977.
- Parmentier, E. M., and J. E. Oliver, A study of shallow global mantle flow due to the accretion and subduction of lithospheric plates, *Geophys. J. R. Astron. Soc.*, 57, 1-21, 1979.
- Parsons, B., and S. Daly, The relationship between surface topography, gravity anomalies, and temperature structure of convection, *J. Geophys. Res.*, 88, 1129-1144, 1983.
- Parsons, B., and F. M. Richter, A relation between the driving force and geoid anomaly associated with mid-ocean ridges, *Earth Planet. Sci. Lett.*, 51, 445-450, 1980.
- Parsons, B., and J. G. Sclater, An analysis of the variation of ocean floor bathymetry and heat flow with age, *J. Geophys. Res.*, 82, 803-827, 1977.
- Peltier, W. R., Mantle viscosity, in *Mantle Convection*, edited by W. R. Peltier, pp. 389-478, Gordon and Breach, New York, 1989.
- Peterson, J., and C. R. Hutt, Test and calibration of the digital world-wide standardized seismograph, *U.S. Geol. Surv. Open File Rep.*, 82-1087, 170 pp., 1982.
- Peterson, J., H. M. Butler, L. G. Holcomb, and C. R. Hutt, The seismic research observatory, *Bull. Seismol. Soc. Am.*, 66, 2049-2068, 1976.
- Pockalny, R. A., R. S. Detrick, and P. J. Fox, Morphology and tectonics of the Kane transform from Sea Beam bathymetry data, *J. Geophys. Res.*, 93, 3179-3193, 1988.
- Purdy, G. M., and R. S. Detrick, Crustal structure of the Mid-Atlantic Ridge at 23°N from seismic refraction studies, *J. Geophys. Res.*, 91, 3739-3762, 1986.
- Rader, C. M., and B. Gold, Digital filter design techniques in the frequency domain, *Proc. IEEE*, 55, 149-171, 1967.
- Randall, M. J., A revised travel-time table for S, *Geophys. J. R. Astron. Soc.*, 22, 229-234, 1971.
- Revenaugh, J., and B. Parsons, Dynamic topography and gravity anomalies for fluid layers whose viscosity varies exponentially with depth, *Geophys. J. R. Astron. Soc.*, 90, 349-368, 1987.
- Richards, M. A., and B. H. Hager, Geoid anomalies in a dynamic Earth, *J. Geophys. Res.*, 89, 5987-6002, 1984.
- Robinson, E. M., B. Parsons, and S. F. Daly, The effect of a shallow low viscosity zone on the apparent compensation of midplate swells, *Earth Planet. Sci. Lett.*, 82, 335-348, 1987.
- Romanowicz, B., M. Cara, J. F. Fels, and D. Rouland, GEO-SCOPE: A French initiative in long period, three-component, global seismic networks, *Eos Trans. AGU*, 65, 753-754, 1984.
- Romanowicz, B., et al., The GEOSCOPE Program: Present status and perspectives, *Bull. Seismol. Soc. Am.*, 81, 243-264, 1991.
- Sandwell, D. T., and K. R. MacKenzie, Geoid height versus topography for oceanic plateaus and swells, *J. Geophys. Res.*, 94, 7403-7418, 1989.
- Sato, H., and I. S. Sacks, Anelasticity and thermal structure of the oceanic upper mantle: Temperature calibration with heat flow data, *J. Geophys. Res.*, 94, 5705-5715, 1989.
- Sato, H., I. S. Sacks, T. Murase, and C. M. Scarfe, Thermal structure of the low velocity zone derived from laboratory and seismic investigations, *Geophys. Res. Lett.*, 15, 1227-1230, 1988.
- Sato, H., I. S. Sacks, and T. Murase, The use of laboratory velocity data for estimating temperature and partial melt fraction in the low-velocity zone: Comparison with heat flow and electrical conductivity studies, *J. Geophys. Res.*, 94, 5689-5704, 1989.
- Schilling, J.-G., Geochemical and isotopic variation along the Mid-Atlantic Ridge axis from 79°N to 0°N, in *The Geology of North America*, vol. M, *The Western North Atlantic Region*, edited by P. R. Vogt and B. E. Tucholke, pp. 137-156, Geological Society of America, Boulder, Colo., 1986.
- Schilling, J.-G., M. B. Bergeron, and R. Evans, Halogens in the mantle beneath the North Atlantic, *Philos. Trans. R. Soc. London, Ser. A*, 297, 147-178, 1980.
- Schilling, J.-G., M. Zajac, R. Evans, T. Johnston, W. White, J. D. Devine, and R. Kingsley, Petrologic and geochemical variations along the Mid-Atlantic Ridge from 29°N to 73°N, *Am. J. Sci.*, 283, 510-586, 1983.

- Sclater, J. G., B. Parsons, and C. Jaupart, Oceans and continents: Similarities and differences in the mechanism of heat loss, *J. Geophys. Res.*, **86**, 11,535–11,552, 1981.
- Scott, D. R., and D. J. Stevenson, A self-consistent model of melting, magma migration and buoyancy-driven circulation beneath mid-ocean ridges, *J. Geophys. Res.*, **94**, 2973–2988, 1989.
- Searle, R. C., Lithospheric structure of the Azores Plateau from Rayleigh-wave dispersion, *Geophys. J. R. Astron. Soc.*, **44**, 537–546, 1976.
- Sheehan, A. F., Lateral variation in upper mantle temperature and composition beneath mid-ocean ridges inferred from shear-wave propagation, geoid, and bathymetry, Ph.D. thesis, 258 pp., Mass. Inst. of Technol., Cambridge, 1991.
- Sheehan, A. F., and M. K. McNutt, Constraints on thermal and mechanical structure of the oceanic lithosphere at the Bermuda Rise from geoid height and depth anomalies, *Earth Planet. Sci. Lett.*, **93**, 377–391, 1989.
- Sipkin, S. A., and T. H. Jordan, Lateral heterogeneity of the upper mantle determined from the travel times of multiple *ScS*, *J. Geophys. Res.*, **81**, 6307–6320, 1976.
- Sipkin, S. A., and T. H. Jordan, Multiple *ScS* travel times in the western Pacific: Implications for mantle heterogeneity, *J. Geophys. Res.*, **85**, 853–861, 1980.
- Sleep, N. H., Segregation of magma from a mostly crystalline mush, *Geol. Soc. Am. Bull.*, **85**, 1225–1232, 1974.
- Sotin, C., and E. M. Parmentier, Dynamical consequences of compositional and thermal density stratification beneath spreading centers, *Geophys. Res. Lett.*, **16**, 835–838, 1989.
- Spudich, P., and J. Orcutt, A new look at the seismic velocity structure of the oceanic crust, *Rev. Geophys.*, **18**, 627–645, 1980.
- Stacey, F. D., A thermal model of the Earth, *Phys. Earth. Planet. Inter.*, **15**, 341–348, 1977.
- Stark, M., and D. W. Forsyth, The geoid, small-scale convection, and differential travel time anomalies of shear waves in the central Indian Ocean, *J. Geophys. Res.*, **88**, 2273–2288, 1983.
- Stewart, I. C. F., and C. E. Keen, Anomalous upper mantle structure beneath the Cretaceous Fogo seamounts indicated by *P*-wave reflection delays, *Nature*, **274**, 788–791, 1978.
- Tanimoto, T., Long wavelength *S*-wave velocity structure throughout the mantle, *Geophys. J. Int.*, **100**, 327–336, 1990.
- Tanimoto, T., and D. L. Anderson, Mapping convection in the mantle, *Geophys. Res. Lett.*, **11**, 287–290, 1984.
- Tucholke, B. E., Structure of basement and distribution of sediments in the western North Atlantic, in *The Geology of North America*, vol. M, *The Western North Atlantic Region*, edited by P. R. Vogt and B. E. Tucholke, pp. 331–340, Geological Society of America, Boulder, Colo., 1986.
- Uhrhammer, R., *S*-wave travel times for a spherically averaged Earth, *Geophys. J. R. Astron. Soc.*, **55**, 283–309, 1978.
- Uhrhammer, R., Shear-wave velocity structure for a spherically averaged Earth, *Geophys. J. R. Astron. Soc.*, **58**, 749–767, 1979.
- U.S. Naval Oceanographic Office, Digital bathymetric database 5 (DBDB5), Natl. Geophys. Data Cent., Boulder Colo., 1985.
- Watts, A. B., D. P. McKenzie, B. E. Parsons, and M. Roufosse, The relationship between gravity and bathymetry in the Pacific Ocean, *Geophys. J. R. Astron. Soc.*, **83**, 263–298, 1985.
- Wells, P. R. A., Pyroxene thermometry in simple and complex systems, *Contrib. Mineral. Petrol.*, **62**, 129–139, 1977.
- White, R. S., Atlantic ocean crust: Seismic structure of a slow spreading ridge, in *Ophiolites and Oceanic Lithosphere*, edited by I. G. Glass, S. J. Lippard, and A. W. Shelton, *Geol. Soc. Spec. Publ. London*, **13**, 101–111, 1984.
- White, R. S., A hot-spot model for early Tertiary volcanism in the N Atlantic, in *Early Tertiary Volcanism and the Opening of the NE Atlantic*, edited by A. C. Morton and L. M. Parson, *Geol. Soc. Spec. Publ. London*, **39**, 3–13, 1988.
- White, R., and D. McKenzie, Magmatism at rift zones: The generation of volcanic continental margins and flood basalts, *J. Geophys. Res.*, **94**, 7685–7729, 1989.
- Whitmarsh, R. B., A. Ginzburg, and R. C. Searle, The structure and origin of the Azores-Biscay Rise, north-east Atlantic Ocean, *Geophys. J. R. Astron. Soc.*, **70**, 79–107, 1982.
- Wood, D. A., A variably veined suboceanic upper mantle—Genetic significance for mid-ocean ridge basalts from geochemical evidence, *Geology*, **7**, 499–503, 1979.
- Woodhouse, J. H., and A. M. Dziewonski, Mapping the upper mantle: Three-dimensional modeling of Earth structure by inversion of seismic waveforms, *J. Geophys. Res.*, **89**, 5953–5986, 1984.
- Woodward, R. L., and G. Masters, Global upper mantle structure from long-period differential travel times, *J. Geophys. Res.*, **96**, 6351–6378, 1991a.
- Woodward, R. L., and G. Masters, Lower mantle structure from *ScS-S* differential travel times, *Nature*, **352**, 231–233, 1991b.
- Wyllie, P. J., Role of water in magma generation and initiation of diapiric uprise in the mantle, *J. Geophys. Res.*, **76**, 1328–1338, 1971.
- Zehnder, C. M., and J. C. Mutter, Systematics of thickness variations in ocean crust (abstract), *Eos Trans. AGU*, **71**, 1573, 1990.
- Zhang, Y.-S., and T. Tanimoto, Investigation of the *SV*-velocity variation of the upper mantle by using Rayleigh waves (abstract), *Eos Trans. AGU*, **71**, 1449, 1990.
- Zhang, Y.-S., and T. Tanimoto, Global Love wave phase velocity variation and its significance to plate tectonics, *Phys. Earth Planet. Inter.*, **66**, 160–202, 1991.

A. F. Sheehan and S. C. Solomon, Department of Earth, Atmospheric, and Planetary Sciences, Bldg. 54-520, Massachusetts Institute of Technology, Cambridge, MA 02139.

(Received March 6, 1991;
revised July 23, 1991;
accepted June 14, 1991.)